



**NTNU – Trondheim**  
Norwegian University of  
Science and Technology

# Bending of X65 Offshore Steel Pipes

**Erik Digerud**

**Kristoffer Lofthaug**

Master of Science in Mechanical Engineering

Submission date: June 2014

Supervisor: Tore Børvik, KT

Co-supervisor: Martin Kristoffersen, KT  
Magnus Langseth, KT

Norwegian University of Science and Technology  
Department of Structural Engineering







## MASTER'S THESIS 2014

SUBJECT AREA: Computational Mechanics	DATE: 10.06.2014	NUMBER OF PAGES: 16 + 156 + 10
--	---------------------	-----------------------------------

TITTEL:  
**Bending of X65 Offshore Steel Pipes**

BY:  
ERIK DIGERUD  
KRISTOFFER LOFTHAUG



**ABSTRACT:**

This thesis is part of an ongoing research program between SIMLab and Statoil about impact loads on X65 offshore pipelines and it is a continuation of previous work. Offshore pipelines are frequently impacted by accidental loads, e.g. trawl gear or anchors. Such loads may cause severe damage to the pipe and a complex stress-strain history locally in the impacted area.

Fracture have previously been found in pipes dynamically impacted. Quasi-static bending of similar pipes with the same boundary conditions have been conducted as part of this thesis. The pipes were examined by metallurgical investigation afterwards, but no sign of fracture was found.

Finite Element Analysis (FEA) of the experiments has been carried out to investigate if it is possible to determine fracture by using the Cockcroft-Latham fracture criterion. To carry out analysis on a highly refined mesh, it has been investigated if it is possible to utilize a technique known as submodeling. The analyses did not succeed in predicting fracture.

Offshore pipelines are often pressurized and this influences the stress-strain history when impacted. As a continuation of previous work it has been conducted quasi-static bending of pressurized and axially loaded pipes. The internal pressure reduced the amount of denting in the impacted zone and increased the stiffness of the pipe with respect to transverse loading.

FEA of the experiments have been conducted to investigate if it is possible to recreate the application of internal pressure and horizontal axial loading. The force-response and deformation of the pipe was found to be described quite well. Horizontal axial loading had minor importance on the plastic deformation locally in the impacted zone.

RESPONSIBLE TEACHER: Tore Børvik  
SUPERVISORS: Tore Børvik, Magnus Langseth and Martin Kristoffersen  
CARRIED OUT AT: SIMLab, Department of Structural Engineering, NTNU





## MASTEROPPGAVE 2014

FAGOMRÅDE: Beregningsmekanikk	DATO: 10.06.2014	ANTALL SIDER: 16 + 156 + 10
----------------------------------	---------------------	--------------------------------

TITTEL:  
**Bøying av X65 offshore stålrør**

UTFØRT AV:  
ERIK DIGERUD  
KRISTOFFER LOFTHAUG



### SAMMENDRAG:

Denne oppgaven er en del av et pågående forskingsprosjekt mellom SIMLab og Statoil om støtlast på offshore rørledninger og er en fortsettelse av tidligere arbeid. Offshore rørledninger blir ofte truffet av tilfeldige laster som f. eks. trålutstyr eller ankere. Slike laster kan skade røret alvorlig og forårsake en kompleks spennings-tøyningshistorie lokalt i det skadede området.

Brudd har tidligere blitt funnet i rør utsatt for dynamisk støtlast. Kvasistatisk bøying av tilsvarende rør med samme grensebetingelser har blitt utført som en del av denne oppgaven. Det ble utført metallurgisk undersøkelse i etterkant, men det ble ikke funnet tegn til brudd.

Analyse ved bruk av elementmetoden av eksperimentene har blitt gjort for å undersøke om det er mulig å påvise brudd ved bruk av Cockcroft-Latham bruddkriteriet. For å utføre analyse på et høyt forfinet elementnett har det blitt undersøkt om det er mulig å benytte en teknikk kjent som submodellering. Analysene klarte ikke å påvise brudd.

Offshore rørledninger er ofte trykksatt og dette påvirker spennings-tøyningshistorien ved støt. Som en fortsettelse av tidligere arbeid har det blitt utført kvasistatisk bøying av rør utsatt for indre trykk og aksial last. Indre overtrykk reduserte mengden lokal deformasjon i den mest skadede sonen og økte stivheten av røret med hensyn til transversell last.

Simulering ved hjelp av elementmetoden har blitt utført for å undersøke om det er mulig å gjenskape effekten av indre overtrykk og horisontal last. Kraftresponsen og deformasjonen til røret ble beskrevet relativt godt. Horisontal last ser ut til å ha mindre betydning for den plastisk deformasjonen lokalt i det skadede.

FAGLÆRER: Tore Børvik  
VEILEDERE: Tore Børvik, Magnus Langseth og Martin Kristoffersen  
UTFØRT VED: SIMLab, Institutt for konstruksjonsteknikk, NTNU



**Institute of Structural Engineering**

FACULTY OF ENGINEERING SCIENCE AND TECHNOLOGY  
NTNU – Norwegian University of Science and Technology

## **MASTER THESIS 2014**

for

*Erik Digerud and Kristoffer Lofthaug*

### **Bending of X65 offshore steel pipes**

*Bøying av X65 offshore stålrør*

After discussions with the Norwegian offshore industry, a need for increased knowledge regarding behaviour, modelling and design of subsea constructions exposed to impact loading from e.g. trawl gear or falling objects has been identified. Metallurgical investigations have shown that fracture may initiate within the pipe wall where the impacting object struck, making such fractures hard to discover – which in turn may result in severe economic and environmental consequences. During such an impact, internal pressure may influence the course of deformation. In this master thesis, X65 steel pipes will be tested both quasi-statically in three-point bending, and quasi-statically with an internal pressure in a stretch-bending rig. The results will be compared to previously conducted dynamic tests and quasi-static tests without inner pressure. This will be done in conjunction with advanced numerical simulations. Accurate numerical models will be an invaluable aid when predicting the probability of fracture after an impact event. The thesis is part of an ongoing research project at CRI SIMLab.

The thesis shall contain the following activities:

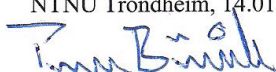
1. Literature review: Previous work on impact against pipes and theory regarding material behavior and fracture in metals.
2. Laboratory tests: Quasi-static three-point bending tests equivalent to previously conducted dynamic tests, and pressurized stretch-bending test equivalent to previously conducted tests on unpressurized pipes shall be carried out with proper instrumentation as this is a central part of the study. These tests will later be used for validation of numerical models.
3. Numerical simulations: Nonlinear finite element analyses of the laboratory tests are another important part of the work. Previously calibrated material models should be used in accordance with the SIMLab Metal Model (SMM). It will in addition be attempted to capture the fracture and cracking that occurred in the previously conducted dynamic tests.
4. Validation and report: The numerical results shall be validated against laboratory tests, and reported in the final thesis.

The thesis work is organised according to current guidelines at NTNU.

*Supervisors:* Tore Børvik, Magnus Langseth and Martin Kristoffersen

**The thesis shall be delivered to the Department of Structural Engineering within 10.06.14.**

NTNU Trondheim, 14.01.2014



Tore Børvik  
Main supervisor/Professor



# Acknowledgements

This master's thesis is a part of an ongoing research program between Centre for Research-based Innovation, Structural Impact Laboratory (CRI SIMlab), NTNU and Statoil ASA on X65 steel pipelines. This thesis has been carried out in the spring 2014, as a conclusion of the master's degree at the Norwegian University of Science and Technology (NTNU).

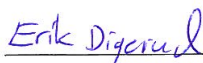
We would like to thank our supervisors Professor Tore Børvik and Ph.D. candidate Martin Kristoffersen for valuable guidance and encouragement through weekly meetings. In addition it must be mentioned that Kristoffersen has been available for questions and discussion almost whenever we needed, which have been highly appreciated. We also wish to thank Magnus Langseth for valuable input regarding the execution of the experiments.

A part of this thesis was doing laboratory tests, and in conjunction with this, we would like to thank Trond Auestad and Tore Wisth for preparing and carrying out the experiments. A great thanks also goes to Egil Fagerholt for providing us with Digital Image Correlation (DIC) analysis of the experiments, and helping us process the results. We would like to thank Ida Westermann for carrying out a metallurgical investigation of the laboratory tests.

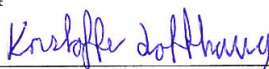
Further we wish to thank David Morin and Professor Torodd Berstad for being most helpful when it came to the numerical work. Additionally we would like to thank Simulia Nordic (Nordic supplier of Abaqus) for giving us valuable input regarding submodeling.

We appreciate that there has been spent this amount of resources on this work during these 20 weeks. We feel privileged to have been given this opportunity to carry out both experimental and numerical work to this extent. This has enabled us to see important aspects of experimental and numerical testing, which has been highly educational.

Trondheim, June 6 2014



\_\_\_\_\_  
Erik Digerud



\_\_\_\_\_  
Kristoffer Lofthaug





# Abstract

This thesis is part of an ongoing research program between SIMLab and Statoil about impact loads on X65 offshore pipelines and it is a continuation of previous work. Offshore pipelines are frequently impacted by accidental loads, e.g. trawl gear or anchors. Such loads may cause severe damage to the pipe and a complex stress-strain history locally in the impacted area.

Fracture have previously been found in pipes dynamically impacted. Quasi-static bending of similar pipes with the same boundary conditions have been conducted as part of this thesis. The pipes were examined by metallurgical investigation afterwards, but no sign of fracture was found.

Finite Element Analysis (FEA) of the experiments has been carried out to investigate if it is possible to determine fracture by using the Cockcroft-Latham fracture criterion. To carry out analyses on a highly refined mesh, it has been investigated if it is possible to utilize a technique known as submodeling. The analyses did not succeed in predicting fracture.

Offshore pipelines are often pressurized and this influences the stress-strain history when impacted. As a continuation of previous work it has been conducted quasi-static bending of pressurized and axially loaded pipes. The internal pressure reduced the amount of denting in the impacted zone and increased the stiffness of the pipe with respect to transverse loading.

FEA of the experiments has been conducted to investigate if it is possible to recreate the application of internal pressure and horizontal loading. The force-response and deformation of the pipe was found to be described quite well. Horizontal loading had minor importance on the plastic deformation locally in the impacted zone.



# Nomenclature

## Symbols

Symbol	Units	Description
$B$	$mm$	Dent width
$b$	$mm$	Buffer width
$C_{ijkl}$	$MPa$	Fourth-order elastic tensor
$[C]$	$kg/s$	Damping matrix
$c_d$	$m/s$	Speed of sound (dilatational wave speed)
$C_\sigma$		Rate sensitivity of the flow stress
$D$		Damage parameter
$\mathbf{D}$	$1/s$	Rate of deformation tensor
$\{\ddot{\mathbf{D}}(t)\}$	$m/s^2$	Acceleration vector
$\{\dot{\mathbf{D}}(t)\}$	$m/s$	Velocity vector
$\{\mathbf{D}(t)\}$	$m$	Displacement vector
$D_i$		Material parameters for the Johnson-Cook fracture criterion
$d$	$mm$	Transverse indenter displacement/Element displacement
$d^*$		Dimensionless transverse indenter displacement
$d_{inner}$	$mm$	Inner pipe diameter
$E$	$MPa$	Youngs' modulus
$F$	$kN$	Transverse indenter force
$F^*$		Dimensionless transverse indenter force
$F_{avg}$	$kN$	Average transverse indenter force
$F_{avg}^{buffer}$	$kN$	Average buffer stiffness
$F_{avg}^{denting}$	$kN$	Average force needed to create a dent
$F_{max}$	$kN$	Maximum transverse pipe load capacity
$\mathbf{F}$		Deformation gradient tensor
$f$	$MPa$	Yield function
$I, II, III$		Invariants of the principal stress tensor
$I_z$	$mm^4$	Second moment of area
$J_2, J_3$		Invariants of the principal deviatoric stress tensor
$k$	$N/m$	Spring stiffness
$[K]$	$N/mm$	Stiffness matrix
$L$	$mm$	Hinge width
$\mathbf{L}$	$1/s$	Velocity gradient tensor
$m_p$	$kNm/m$	Plastic moment capacity per unit length

$[M]$	$kg$	Mass matrix
$\mathbf{n}$		Unit normal vector
$N_{DOF}$		Total number of degrees of freedom
$P_{avg}^{int}$	$bar$	Average internal pressure
$Q_{R_i}, \theta_{R_i}$	$MPa, MPa$	Voce hardening parameters
$Q_{\chi_i}, \theta_{\chi_i}$	$MPa, MPa$	Armstrong-Fredericks hardening parameters
$\mathbf{R}$		Rotational matrix
$\{\mathbf{R}^{ext}(t)\}$	$N$	External force vector
$r$	$mm$	Pipe radius
$T^*$		Homologous temperature
$t$	$mm$	Pipe wall thickness
$\mathbf{V}$		Deformation tensor
$\mathbf{v}$	$m/s$	Velocity vector
$\mathbf{W}$	$1/s$	Spin tensor
$W_{cr}$	$MPa$	Cockcroft-Latham parameter
$w$	$kNm/mm$	Plastic work per unit length
$\Delta$	$mm$	Local dent depth
$\Delta t_{cr}$	$s$	Critical time step
$\boldsymbol{\varepsilon}$		Strain tensor
$\boldsymbol{\varepsilon}'$		Deviatoric strain tensor
$\boldsymbol{\varepsilon}^e$		Elastic strain tensor
$\boldsymbol{\varepsilon}^p$		Plastic strain tensor
$\dot{\boldsymbol{\varepsilon}}^p$	$s^{-1}$	Plastic strain rate tensor
$\boldsymbol{\varepsilon}_{principal}$		Principal strain tensor
$\varepsilon_1, \varepsilon_2, \varepsilon_3$		Principal strains
$\dot{\varepsilon}_0$	$s^{-1}$	Reference strain rate
$\varepsilon_{eq}$		Equivalent strain
$\varepsilon_{eq}^f$		Equivalent strain to failure
$\varepsilon_{qbs}^f$		Absolute fracture strain
$\varepsilon_{rel}^f$		Relative fracture strain
$\varepsilon_{t,rel}$		Relative true strain
$\varepsilon_{eq}^p$		Equivalent plastic strain
$\varepsilon_{eq}^{p,0}$		Reference equivalent plastic strain
$\dot{\varepsilon}_{eq}$	$s^{-1}$	Equivalent plastic strain rate
$\dot{\varepsilon}_{eq}^{p,*}$		Dimensionless relative strain rate
$\kappa$		Dimensionless buffer stiffness constant
$\dot{\lambda}$	$s^{-1}$	Plastic multiplier
$\mu_\sigma$		Lode Parameter
$\rho$	$kg/m^3$	Density
$\boldsymbol{\sigma}$	$MPa$	Cauchy stress tensor
$\boldsymbol{\sigma}_{principal}$	$MPa$	Principal stress tensor
$\boldsymbol{\sigma}'$	$MPa$	Deviatoric stress tensor
$\sigma^*$		Stress triaxiality ratio
$\sigma_1, \sigma_2, \sigma_3$	$MPa$	Principal stresses
$\sigma_x, \sigma_y, \sigma_z$	$MPa$	Normal stresses
$\sigma_Y$	$MPa$	Yield stress

$\sigma_H$	<i>MPa</i>	Hydrostatic stress
$\sigma_{eq}$	<i>MPa</i>	Equivalent stress (in relation to the used yield criteria)
$\sigma_{eq}^h$	<i>MPa</i>	Equivalent Hershey stress
$\sigma_{eq}^m$	<i>MPa</i>	Equivalent von Mises stress
$\sigma_{eq}^t$	<i>MPa</i>	Equivalent Tresca stress
$\sigma_t$	<i>MPa</i>	True stress
$\tilde{\sigma}_{ij}$	<i>MPa</i>	Effective stress between voids
$\tau_{xy}, \tau_{xz}, \tau_{yz}$	<i>MPa</i>	Shear stresses
$\chi$	<i>MPa</i>	Backstress tensor
$\dot{\chi}$	<i>MPa/s</i>	Rate of backstress tensor

## Acronyms

AVG	Average
BCC	Body Centred Cubic
CAE	Complete Abaqus Environment
CPU	Central Processing Unit
DIC	Digital Image Correlation
DOF	Degree Of Freedom
FEA	Finite Element Analysis
NTNU	Norwegian University of Science and Technology
SEM	Scanning Electron Microscopy
SDEV	Standard Deviation
SMM	SIMLab Metal Model
UTG	Ultrasonic Thickness Gauge

# Contents

<b>1</b>	<b>Introduction</b>	<b>1</b>
<b>2</b>	<b>Material Behaviour</b>	<b>5</b>
2.1	Stress . . . . .	6
2.1.1	Cauchy Stress Tensor . . . . .	6
2.1.2	Principal Stresses . . . . .	7
2.1.3	Hydrostatic and Deviatoric Stress . . . . .	7
2.2	Strain . . . . .	9
2.2.1	Finite Strain Theory . . . . .	9
2.2.2	Logarithmic Strain . . . . .	9
2.2.3	Principal Strains . . . . .	11
2.3	Plastic Deformation . . . . .	12
2.3.1	Yield Criterion . . . . .	12
2.3.2	Plastic Flow Rule . . . . .	14
2.4	Scalar Measures of Stress and Strain . . . . .	17
2.4.1	Equivalent Stress . . . . .	17
2.4.2	Equivalent Strain . . . . .	18
2.4.3	Stress Triaxiality Ratio . . . . .	19
2.4.4	Lode Parameter . . . . .	19
2.5	Strain Decomposition . . . . .	20
2.6	Work Hardening . . . . .	21
2.6.1	Isotropic Hardening . . . . .	21
2.6.2	Kinematic Hardening . . . . .	21
2.7	Viscoplasticity . . . . .	23
<b>3</b>	<b>Failure</b>	<b>25</b>
3.1	Theory . . . . .	26
3.1.1	Ductile Fracture . . . . .	26
3.1.2	Brittle Fracture . . . . .	29
3.1.3	Dynamic Mechanisms . . . . .	31
3.2	Previous Findings . . . . .	33
3.2.1	X65 Steel . . . . .	33
3.2.2	Component Tests . . . . .	34
3.2.3	Uniaxial Compression-Tension Tests . . . . .	37
3.3	Fracture Criterion . . . . .	41

3.3.1	Coupled Approach . . . . .	41
3.3.2	Uncoupled Approach . . . . .	42
<b>4</b>	<b>Experimental Work</b>	<b>49</b>
4.1	Quasi-Static Bending of Simply Supported Empty Pipes . . . . .	50
4.1.1	Previous Findings . . . . .	50
4.1.2	Experimental Setup . . . . .	51
4.1.3	Pipe Measurement . . . . .	52
4.1.4	Results . . . . .	54
4.1.5	Metallurgical Investigation . . . . .	61
4.2	Quasi-Static Bending of Pressurized Pipes With Horizontal Axial Loading . . . . .	67
4.2.1	Experimental Setup . . . . .	67
4.2.2	Pipe Measurement . . . . .	70
4.2.3	Previous Findings . . . . .	71
4.2.4	Results . . . . .	73
4.3	Concluding Remarks . . . . .	83
<b>5</b>	<b>Finite Element Analysis</b>	<b>85</b>
5.1	Theory . . . . .	86
5.1.1	Time Integration . . . . .	86
5.1.2	Stability . . . . .	86
5.1.3	Energy Balance . . . . .	87
5.1.4	Locking . . . . .	88
5.1.5	Submodeling . . . . .	89
5.2	Material Model . . . . .	90
5.2.1	SIMLab Metal Model . . . . .	91
5.3	Quasi-Static Bending of Pressurized Pipes With Horizontal Axial Loading . . . . .	93
5.3.1	Numerical Model . . . . .	93
5.3.2	Results . . . . .	95
5.3.3	The Effect of Internal Pressure . . . . .	100
5.4	Quasi-Static Bending of Simply Supported Empty Pipes . . . . .	104
5.4.1	Numerical Model . . . . .	104
5.4.2	Results . . . . .	105
5.5	Dynamic Impact on Simply Supported Empty Pipes (Pipe K) . . . . .	108
5.5.1	1/4 Global Model Vs. 1/2 Global Model in Coherence with Submodelling . . . . .	109
5.5.2	Global Model . . . . .	110
5.5.3	Submodeling . . . . .	121
5.5.4	Refined Submodel Analysis . . . . .	126
5.5.5	Change of Yield Surface . . . . .	132
5.5.6	Global Analysis Using Fully Integrated Elements . . . . .	133
5.5.7	The Effect of Pressure . . . . .	141
5.5.8	Summery and Discussion . . . . .	145
<b>6</b>	<b>Summary and Conclusions</b>	<b>147</b>

<b>Further Work</b>	<b>153</b>
<b>References</b>	<b>155</b>
<b>Appendices</b>	<b>159</b>
A.1 Pipe Measurements . . . . .	159
A.2 Pipe Flange . . . . .	166
A.3 SMM Material card . . . . .	168



# Chapter 1

## Introduction

On November 1st 2007, Statoil discovered that one of their gas pipelines had been dragged approximately 50 *m* out of its initial position by an anchor at the Kvitebjørn oil field. The production was temporarily shut down, but after inspection it was decided safe to reopen the pipeline. Half a year later a leak was discovered in the damaged pipe, and this led to an immediate shut down of the oil field for repairs. This accident highlighted the need for a deeper knowledge on how cracks initiate and develop in such pipelines. It also commenced a project between Statoil and the Structural Impact Laboratory (SIMLab) on impact against offshore steel pipes. The task was to investigate dynamic impacts on offshore pipelines to gain knowledge about the loads and the mechanisms causing an offshore pipeline made of X65 steel to fail.

At this point, five different master's theses have been written as part of this project [1, 2, 3, 4, 5], along with an ongoing Ph.D. project which is to be finished this year. Multiple component tests have previously been carried out on scaled pipes, exposed to different cases of loading and boundary conditions (Figure 1.1), followed by numerical analysis to get a deeper understanding on the strains and stresses which develop locally in the pipe when impacted. As part of this, material tests have been conducted in the attempt to calibrate an accurate material model.

A typical trawl gear accident is characterized by different phases of loading: impact, hooking, pull-over and release [6]. Such an event causes a complex stress-strain history which is not particularly well covered in existing guidelines [7]. To gain knowledge of the stresses and strains that develop during such an event, simplified experiments on simply supported scaled pipes have been conducted in the lab. The kicking machine [8] was used to launch a trolley with a given mass and velocity against a simply supported pipe. After the impact event the pipe was stretched straight in a tension rig. This was considered to be a simplification of the loading sequence of impact and straightening of a full-scale pipeline. Visual fracture was found on all pipes after stretching [1]. Metallurgical investigation of pipes only exposed to impact revealed that internal and external cracks were

# 1. Introduction

---

present already before stretching [3]. Equivalent quasi-static tests will be carried out as part of this thesis to investigate if such fracture is dynamically dependent. I.e. it shall be investigated if internal or external cracks are present also after quasi-static bending. The work will in this way be a continuation of the theses written by Slåttedalen and Ørmen [1] and Aune and Hovdelien [3].

A pipeline will in reality be under the influence of internal pressure and axial loading. These effects are assumed to affect the response of the pipe when it is impacted. Simplified quasi-static experiments have previously been conducted in a three point stretch-bending rig [9]. These experiments are discussed in the thesis by Asheim and Mogstad [4] and the thesis by Jacobsen [5]. Both constant and linearly increasing horizontal loading were applied as the pipe were quasi-statically deformed at midspan by a rigid indenter to account for the effect of axial loading. Horizontal axial loading was found to especially increase the force response in the last phase of deformation when the pipe bends in a global mode of deformation. The amount of local deformation was found to be approximately unaffected by horizontal axial loading. Pipes exposed to both bending and stretching displayed visual surface cracks of varying size after stretching. As part of this thesis quasi-static bending experiments (without stretching) on pipes exposed to both horizontal axial loading and internal pressure will be examined.

	Impact only	Impact and stretching	
Simply supported	<div style="background-color: red; color: white; padding: 5px; text-align: center;">           Pipe: K, L            Aune and Hovdelien            (2012)         </div>	<div style="background-color: blue; color: white; padding: 5px; text-align: center;">           Pipe: M, N            Digerud and Lofthaug            (2014)         </div>	<div style="background-color: red; color: white; padding: 5px; text-align: center;">           Pipe: A, B, C, D            Slåttedalen and Ørmen            (2010)         </div>
Internal Pressure	<div style="background-color: red; color: white; padding: 5px; text-align: center;">           Pipe: G, H, I, J            Fornes and Gabrielsen            (2011)*         </div>	<div style="background-color: blue; color: white; padding: 5px; text-align: center;">           Pipe: 8, 9, 10            Digerud and Lofthaug            (2014)**         </div>	
Axial loading		<div style="background-color: blue; color: white; padding: 5px; text-align: center;">           Pipe: 4, 5, 6            Jakobsen            (2014)***         </div>	<div style="background-color: blue; color: white; padding: 5px; text-align: center;">           Pipe 1, 2, 3            Asheim and Mogstad            (2013)         </div>

Dynamic
  Quasi-static

\* Experiments on open and encapsulated pipes filled with water. I.e. not constant pressure.

\*\* Experiments with both internal pressure and axial loading.

\*\*\* Work conducted fall 2013

**Figure 1.1:** Different experiments on pipes conducted as part of this project.

The results will be compared with pipes exposed to horizontal loading only.

The experimental work is followed by numerical work using Finite Element Analysis (FEA) to investigate if the experimental tests can be predicted numerically and to get a deeper understanding of the local stresses and strains that develop in a pipe when it is deformed. The numerical work will in particular focus on fracture and if it is possible to predict fracture using the Cockcroft-Latham fracture criterion. In previous works it has been noted that a high number of elements is needed in the impacted area to accurately describe the plastic strains that develop. It will be investigated if it is possible to utilize an numerical technique known as submodeling to carry out analyses on a highly refined mesh. Additionally, refined global models will be carried out. In light of the experiments on pressurized pipes, special attention will be made on how pressure influences the stresses and strains that develop when a pipe is deformed.



## Chapter 2

# Material Behaviour

The major goal of this project is to gain a better understanding of the loads causing a pipe to fail after an impact event. An important part of this is to understand the behaviour of the material itself and how this behaviour can be modeled and implemented in numerical models. Such models enables one to carry out numerous "numerical experiments" for different load cases, it also enables one to investigate the strains and stresses which develop in the pipe wall during impact on a much more detailed level. One of the key factors to make such models useful, is to model the material behaviour in an appropriate way through constitutive equations. But before constitutive equations can be developed a consistent mathematical framework of stress and strain must be established. The following presentation will not go through the derivation of each expression since this can be found in a detailed manner in most books written on the topic of continuum mechanics, instead a general summary of the most important aspects will be presented.

The general concept of stress and strain will first be presented, secondly an introduction to plasticity and how this is mathematically treated and finally some commonly used scalar measures of stress and strain will be presented. Tensors, matrices and vectors will be written in bold. Index notation will be used some places where it is practical, in which cases indices  $i$  and  $j$  are according to the axis of a general 3D cartesian coordinate system:  $1 \leq i, j \leq 3$ .

## 2.1 Stress

The internal forces acting in the material during deformation are typically defined through the Cauchy stress tensor, which is a 2nd order tensor describing the stresses acting on a 3-dimensional solid cube (Figure 2.1). Many different subsets of this tensor have been developed to describe different aspects of material behaviour, and therefore the most important ones used throughout this thesis, in addition to the stress tensor itself, will be presented.

### 2.1.1 Cauchy Stress Tensor

The Cauchy stress tensor is a 2nd order tensor with nine stress components that completely define the state of stress at a point inside a material in the deformed configuration. It can be written on matrix form as

$$\boldsymbol{\sigma} = \sigma_{ij} = \begin{bmatrix} \sigma_{11} & \sigma_{12} & \sigma_{13} \\ \sigma_{21} & \sigma_{22} & \sigma_{23} \\ \sigma_{31} & \sigma_{32} & \sigma_{33} \end{bmatrix} = \begin{bmatrix} \sigma_x & \tau_{xy} & \tau_{xz} \\ \tau_{yx} & \sigma_y & \tau_{yz} \\ \tau_{zx} & \tau_{zy} & \sigma_z \end{bmatrix}, \quad (2.1)$$

where  $\sigma_i$  ( $i=x,y,z$ ) denotes normal stresses and  $\tau_{ij}$  ( $i,j=x,y,z$ ) shear stresses. The material point must however be in equilibrium, which means that the tensor is symmetric, having only six independent stress components:  $\sigma_x, \sigma_y, \sigma_z, \tau_{xy} = \tau_{yx}, \tau_{xz} = \tau_{zx}$  and  $\tau_{yz} = \tau_{zy}$ .

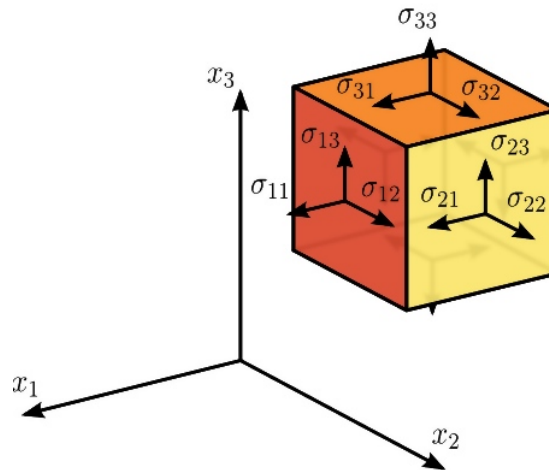


**Figure 2.1:** The stresses acting on a 3-dimensional solid cube according to the Cauchy stress tensor, where  $x_1, x_2$  and  $x_3$  denotes the  $x, y$  and  $z$  axis respectively [10].

### 2.1.2 Principal Stresses

The principal stress theorem states that: *For any state of stress there exists, through a particle, three orthogonal planes free of shear stresses. The planes are called the principal stress planes, the three unit normals  $\mathbf{n}_1$ ,  $\mathbf{n}_2$  and  $\mathbf{n}_3$  to the planes are the principal stress directions, and the normal stresses  $\sigma_1$ ,  $\sigma_2$  and  $\sigma_3$  on the planes are the principal stresses in the particle* [11]. It is thus possible to rotate the cube in Figure 2.1 in such a way that only normal stresses will act on it. The orientation is expressed through the three unit normals,  $\mathbf{n}_i$ , and the principal stresses,  $\sigma_i$  ( $i=1,2,3$ ), can be found by solving the eigenvalue problem

$$(\boldsymbol{\sigma} - \sigma \mathbf{I})\mathbf{n} = 0, \quad (2.2)$$

where  $\boldsymbol{\sigma}$  is the Cauchy stress tensor and  $\mathbf{I}$  the diagonal identity matrix. The non-trivial solution to this equation is found when the determinant,  $\det((\boldsymbol{\sigma} - \sigma \mathbf{I})) = 0$ , which gives the characteristic equation

$$\sigma^3 - I\sigma^2 + II\sigma - III = 0. \quad (2.3)$$

$I, II, III$  are called the principal invariants of the Cauchy stress tensor. The three roots of Equation (2.3) yields the principal stresses  $\sigma_1$ ,  $\sigma_2$  and  $\sigma_3$ , and the corresponding eigenvectors  $\mathbf{n}_1$ ,  $\mathbf{n}_2$  and  $\mathbf{n}_3$  are the principal directions. If the volume element in Figure 2.1 is rotated according to these directions, the stress tensor can be written on matrix form as a diagonal matrix

$$\boldsymbol{\sigma}_{principal} = \begin{bmatrix} \sigma_1 & 0 & 0 \\ 0 & \sigma_2 & 0 \\ 0 & 0 & \sigma_3 \end{bmatrix}. \quad (2.4)$$

This is a very useful transformation because it allows one to deal with three normal stresses instead of six. It is also worth noting that the invariants  $I, II, III$  are coordinate invariants, i.e. they are the same whether they stem from the characteristic equation of  $\boldsymbol{\sigma}$  or  $\boldsymbol{\sigma}_{principal}$  [11].

### 2.1.3 Hydrostatic and Deviatoric Stress

It is common to assume that plastic deformation in most metals occurs without any change of volume. It is therefore useful to decompose the stress tensor into two parts,  $\boldsymbol{\sigma} = \boldsymbol{\sigma}' + \sigma_H \mathbf{I}$ . Here  $\sigma_H$  is the hydrostatic stress causing change of volume (acts as a form of pressure) and  $\boldsymbol{\sigma}'$  is the deviatoric part associated with shear deformation.  $\sigma_H$  is calculated as the average normal stress

$$\sigma_H = \frac{\sigma_x + \sigma_y + \sigma_z}{3} = \frac{\sigma_1 + \sigma_2 + \sigma_3}{3}. \quad (2.5)$$

The deviatoric stress tensor is obtained by subtracting the hydrostatic stress from the Cauchy stress tensor

$$\boldsymbol{\sigma}' = \boldsymbol{\sigma} - \sigma_H \mathbf{I} = \begin{bmatrix} \sigma_x & \tau_{xy} & \tau_{xz} \\ \tau_{yx} & \sigma_y & \tau_{yz} \\ \tau_{zx} & \tau_{zy} & \sigma_z \end{bmatrix} - \begin{bmatrix} \sigma_H & 0 & 0 \\ 0 & \sigma_H & 0 \\ 0 & 0 & \sigma_H \end{bmatrix}. \quad (2.6)$$

## 2. Material Behaviour

---

As with the Cauchy stress tensor the deviatoric stress tensor can be transformed into principal deviatoric stresses by solving the eigenvalue problem,  $\det((\boldsymbol{\sigma}' - \sigma \mathbf{I})) = 0$ . This leads to a characteristic equation of the form

$$(\sigma')^3 - J_2 \sigma' - J_3 = 0. \quad (2.7)$$

Here  $-I\sigma^2$ , the term from Equation (2.3) is missing since  $I = J_1 = \text{tr}(\boldsymbol{\sigma}') = 0$  by definition due to the subtraction of the hydrostatic stress (average normal stress) from the deviatoric stress tensor [11].



## 2.2 Strain

Strain is a description of deformation in terms of relative displacement of particles in a body that exclude rigid body motions [12]. The strain tensor is typically written on matrix form as

$$\boldsymbol{\varepsilon} = \varepsilon_{ij} = \begin{bmatrix} \varepsilon_{11} & \varepsilon_{12} & \varepsilon_{13} \\ \varepsilon_{12} & \varepsilon_{22} & \varepsilon_{23} \\ \varepsilon_{13} & \varepsilon_{23} & \varepsilon_{33} \end{bmatrix}. \quad (2.8)$$

The tensor is symmetric, which leaves us with six unknown variables:  $\varepsilon_{11}$ ,  $\varepsilon_{22}$ ,  $\varepsilon_{33}$ ,  $\varepsilon_{12} = \varepsilon_{21}$ ,  $\varepsilon_{13} = \varepsilon_{31}$  and  $\varepsilon_{23} = \varepsilon_{32}$ . Where the three first are normal strains and the three last are shear strains. A large number of different strain measures exist, measures that will report different values of strain for the same physical deformation when the deformations become large. Some commonly known measures of strain are Green's strain, Almansi strain, nominal strain and logarithmic strain. It is however important to note that each concept needs a corresponding measure of stress which is work conjugative. The work conjugative measure of strain to the Cauchy stress tensor is the logarithmic strain tensor.

### 2.2.1 Finite Strain Theory

Physical deformation is typically described through the deformation gradient tensor,  $\mathbf{F}$ , defined as

$$\mathbf{F} = \frac{\partial \mathbf{x}}{\partial \mathbf{X}}. \quad (2.9)$$

Here  $\mathbf{X}$  is a vector describing the position of a material particle in the undeformed configuration,  $C_0$ , and  $\mathbf{x}$  is a vector describing the position of the same particle in the deformed configuration,  $C_n$  (Figure 2.2). A problem arises when the deformations become large, and the material particle,  $Q$ , is subjected to both stretches and rigid body rotations. Stretches contributes to strain while rigid body rotations do not and the problem is that  $\mathbf{F}$  do not distinguish between stretch and rigid body rotation [13]. How the stretches are separated from the deformation gradient tensor,  $\mathbf{F}$ , is the difference between the previously mentioned strain measures. However the key is the polar decomposition theorem which allows us to decompose  $\mathbf{F}$  into a deformation tensor,  $\mathbf{V}$ , (also known as "left Cauchy-Green deformation tensor") and a rotational matrix,  $\mathbf{R}$ .

$$\mathbf{F} = \mathbf{V} \cdot \mathbf{R}. \quad (2.10)$$

The decomposition can be interpreted as a two-step process: first rotate the particle by  $\mathbf{R}$  and then apply deformations through  $\mathbf{V}$  on the rotated particle. However the particle remains fixed in a physical context, as a part of a larger physical continuum. It is moreover the infinitesimal "virtual cube" in which strains are measured that is rotated.

### 2.2.2 Logarithmic Strain

The default strain output variable in Abaqus/Explicit is logarithmic strain [15]. Logarithmic strain (commonly known as true strain or natural strain) arises from

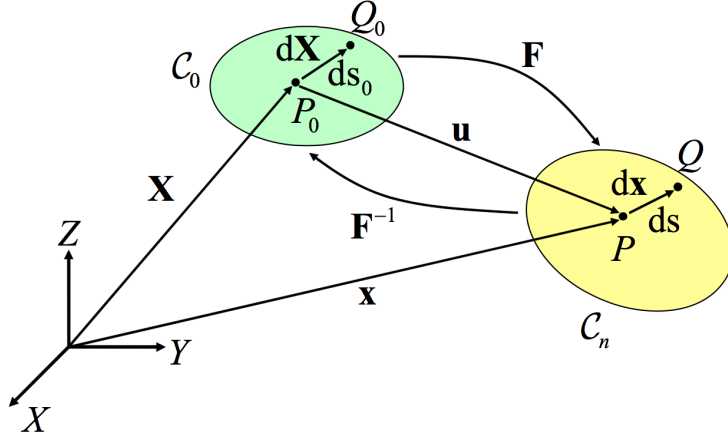


**Figure 2.2:**  $\mathbf{X}$  refers to a material point  $P_0$  in the reference configuration,  $C_0$ , and  $\mathbf{x}$  refers to the position of the same point in the deformed configuration,  $C_n$ .  $d\mathbf{X}$  describes the relative position of a neighbouring point and  $d\mathbf{x}$  the position after deformation for the same neighbouring particle,  $ds_0$  and  $ds$  are the absolute length of  $d\mathbf{X}$  and  $d\mathbf{x}$ , respectively [14].

the time integration of the rate of deformation tensor,  $\mathbf{D}$ . The rate of deformation tensor is defined through the velocity gradient tensor, defined as

$$\mathbf{L} = \frac{\partial \mathbf{v}}{\partial \mathbf{x}}. \quad (2.11)$$

Here  $\mathbf{v}$  is a 1st order tensor describing the velocities around the material particle described by the vector  $\mathbf{x}$  in the deformed configuration,  $C_n$ .  $\mathbf{L}$  is a tensor describing the velocity gradients around the particle. The velocity gradient tensor,  $\mathbf{L}$ , can be decomposed into a symmetric and an antisymmetric tensor.

$$\mathbf{L} = \frac{1}{2}(\mathbf{L} + \mathbf{L}^T) + \frac{1}{2}(\mathbf{L} - \mathbf{L}^T), \quad (2.12)$$

where  $\frac{1}{2}(\mathbf{L} + \mathbf{L}^T)$  is the symmetric part, denoted as the rate of deformation tensor,  $\mathbf{D}$ , and  $\frac{1}{2}(\mathbf{L} - \mathbf{L}^T)$  is the antisymmetric part, denoted as the spin tensor,  $\mathbf{W}$ , such that

$$\mathbf{L} = \mathbf{D} + \mathbf{W}. \quad (2.13)$$

If the directions of strain remain fixed through the deformation, the logarithmic strain can be obtained directly by time integration of the rate of deformation tensor

$$\boldsymbol{\varepsilon}^{n+1} = \int_0^{t^{n+1}} \mathbf{D} dt. \quad (2.14)$$

However this is not possible if the directions of strain change during deformation, but the expression explains the origin of logarithmic strain.

During FEA the deformation is calculated as a series of increments, with corre-

sponding strain increments,  $\Delta\boldsymbol{\epsilon}$ . If the direction of strain is assumed constant during one increment, the strain increment,  $\Delta\boldsymbol{\epsilon}$ , can be related to the incremental deformation tensor,  $\Delta\boldsymbol{V}$ , such that

$$\Delta\boldsymbol{\epsilon} = \ln\Delta\boldsymbol{V}. \quad (2.15)$$

A detailed derivation of this relationship is found in [16].

### 2.2.3 Principal Strains

Analogous to what was done with the stress tensor,  $\boldsymbol{\sigma}$ , the strain tensor,  $\boldsymbol{\epsilon}$ , can be rotated in such a way that only normal strains exist by solving the eigenvalue problem defined by

$$(\boldsymbol{\epsilon} - \varepsilon\mathbf{I})\mathbf{n} = \mathbf{0}. \quad (2.16)$$

This problem yields three solutions for  $\varepsilon$ :  $\varepsilon_1$ ,  $\varepsilon_2$  and  $\varepsilon_3$ . With three corresponding principal directions, expressed as the eigenvectors of Equation (2.16):  $\mathbf{n}_1$ ,  $\mathbf{n}_2$  and  $\mathbf{n}_3$ . The principal directions represents the orientation of the axes in the rotated coordinate system in which the principal strains are expressed. Like  $\boldsymbol{\sigma}_{principal}$ ,  $\boldsymbol{\epsilon}_{principal}$  can be written on matrix form as a diagonal matrix

$$\boldsymbol{\epsilon}_{principal} = \begin{bmatrix} \varepsilon_1 & 0 & 0 \\ 0 & \varepsilon_2 & 0 \\ 0 & 0 & \varepsilon_3 \end{bmatrix}. \quad (2.17)$$

### 2.3 Plastic Deformation

Plasticity is a phenomena describing irreversible deformation of metals. When pipelines are hit by either trawl gear or an anchor, the pipe material will most likely experience plastic deformation, and thus is plasticity an important part when it comes to describing the behaviour of the X65 steel pipe. A summery of how plasticity is modeled will now be presented to gain an understanding of the assumptions needed to be able to develop constitutive equations applicable to the numerical model. The following theory is mainly based on the compendium written by O.S. Hopperstad and T. Børvik related to the course Materials Mechanics at NTNU [17].

#### 2.3.1 Yield Criterion

The yield criterion expresses when the material deforms elastically and when it deforms plastically. This is expressed through the yield function,  $f(\boldsymbol{\sigma})$ , which is a continuous function of the stress tensor,  $\boldsymbol{\sigma}$ . Where

$$f(\boldsymbol{\sigma}) \leq 0 \quad (2.18)$$

applies when the material is assumed rate-independent.  $f(\boldsymbol{\sigma}) = 0$  means that the material deforms plastically (yield limit) and  $f(\boldsymbol{\sigma}) < 0$  means that the material deforms elastically (Figure 2.3).

The yield surface determines the states of stress causing plastic deformation and therefore it is often denoted as the yield criterion, its shape may however vary. Two criteria (or shapes) often used are the Von Mises and Tresca criteria. Both criteria are isotropic, meaning that the yield function is independent of the direction of loading. They are also pressure-independent. This implies that yielding is independent of the hydrostatic stress,  $\sigma_H$ . This gives physical meaning since plastic deformation in metals to a large extent takes place by plastic slip, which is a shear-driven deformation mode hence not causing any change of volume.

#### von Mises Criterion

The von Mises criterion states that plastic deformation occurs when a scalar measure of stress, named von Mises equivalent stress,  $\sigma_{eq}^m$  (explained in Section 2.4.1), is equal to the yield stress,  $\sigma_Y$ . Its three dimensional shape is illustrated in Figure 2.6. If plane stress is assumed it takes the two dimensional elliptical form seen in Figure 2.4. The yield function can be written in terms of the principal stresses as

$$f(\sigma_1, \sigma_2, \sigma_3) = \left( \frac{1}{2}((\sigma_1 - \sigma_2)^2 + (\sigma_2 - \sigma_3)^2 + (\sigma_3 - \sigma_1)^2) \right)^{\frac{1}{2}} - \sigma_Y = 0. \quad (2.19)$$

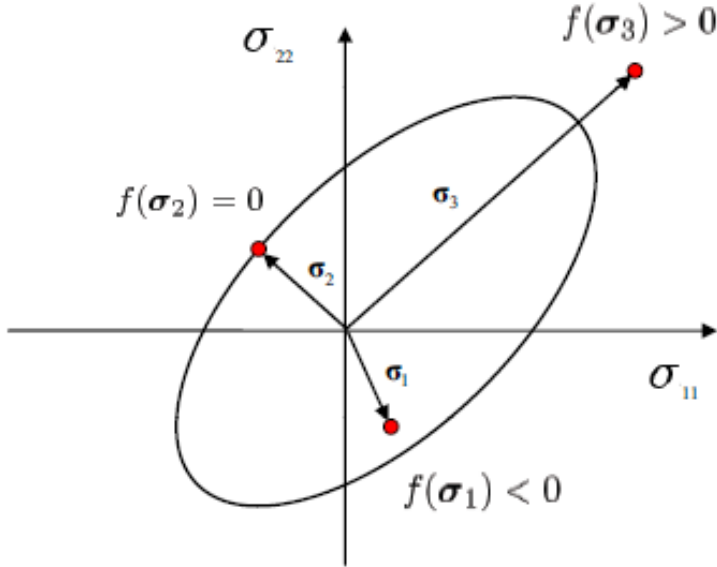


**Figure 2.3:** Elastic domain, yield surface and inadmissible region [17]

### Tresca Criterion

The Tresca criterion assume yielding to occur when the maximum shear stress,  $\tau_{max}$ , reaches a critical value

$$\tau_{max} = \frac{1}{2}(\sigma_{max} - \sigma_{min}), \quad (2.20)$$

where  $\sigma_{max/min}$  is the maximum and minimum principal stresses. In case of plane stress does the Tresca yield surface takes the shape of a hexagon (Figure 2.4). The yield function can be written in terms of the principal stresses as

$$f(\sigma) = \frac{1}{2}(|\sigma_1 - \sigma_2| + |\sigma_2 - \sigma_3| + |\sigma_3 - \sigma_1|) - \sigma_Y = 0. \quad (2.21)$$

### High-exponent Yield Criterion

The high-exponent yield criterion (or Hershey criterion) can be expressed in terms of the principal stresses as

$$f(\sigma_1, \sigma_2, \sigma_3) = \left( \frac{1}{2}(|\sigma_1 - \sigma_2|^m + |\sigma_2 - \sigma_3|^m + |\sigma_3 - \sigma_1|^m) \right)^{\frac{1}{m}} - \sigma_Y = 0, \quad (2.22)$$

where  $m$  is a constant that determines the curvature of the yield surface:  $m = 2$  equals the von Mises criterion and  $m \rightarrow \infty$  equals the Tresca criterion. I.e. the surface will vary between the Tresca and the von Mises surface when changing

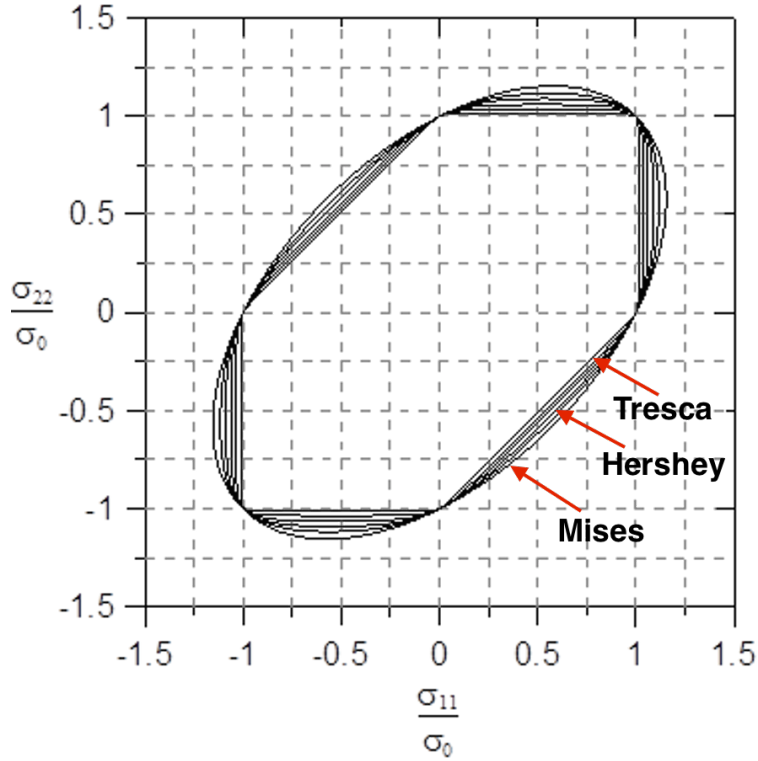


**Figure 2.4:** Geometric representation of the high-exponent yield criterion for plane stress conditions and different  $m$ -values [17].

the parameter  $m$  (Figure 2.4).

### 2.3.2 Plastic Flow Rule

The plastic flow rule determines the evolution of the plastic strain tensor,  $\varepsilon_{ij}^p$ . It defines the plastic strain rate tensor,  $\dot{\varepsilon}_{ij}^p$ , and can in the most general case be written as

$$\dot{\varepsilon}_{ij}^p = \dot{\lambda} h_{ij}, \quad (2.23)$$

where  $h_{ij}$  is the flow function and  $\dot{\lambda}$  is the plastic multiplier (non-negative scalar).  $h_{ij}$  can be defined by the yield function,  $f(\boldsymbol{\sigma})$ , such that

$$h_{ij} = \frac{\partial f}{\partial \sigma_{ij}}. \quad (2.24)$$

By doing this the associated flow rule is obtained. It is important to note that the associated flow rule implies that the shape of the yield surface determines both

the stress state where yielding initiates and the direction of the plastic flow. This implies that the plastic strain increment,  $d\epsilon_{ij}^p = \dot{\epsilon}_{ij}^p dt$ , is parallel to the normal vector of the yield surface,  $\mathbf{n}$ , at the stress state,  $\boldsymbol{\sigma}$  (Figure 2.5). The flow rule can now be written as

$$\dot{\epsilon}_{ij}^p = \dot{\lambda} \frac{\partial f}{\partial \sigma_{ij}} = \dot{\lambda} \mathbf{n}, \quad (2.25)$$

where the plastic multiplier,  $\dot{\lambda}$ , can be identified as the equivalent plastic strain rate,  $\dot{\epsilon}_{eq}^p$  (Section 2.5). This is the most common way to define the plastic flow rule when it comes to describing the behaviour of metals, and it ensures that plastic dissipation is non-negative

$$\mathfrak{D}_p = \sigma_{ij} \dot{\epsilon}_{ij}^p \geq 0, \quad (2.26)$$

where  $\mathfrak{D}_p$  is the energy dissipated through plastic deformation as heat. I.e. plastic deformation can not occur without external supply of energy.

If the yield surface has corners i.e. singular points, the normal vector to the yield surface is not unique, then at such a point  $\dot{\epsilon}^p$  must lie in the cone formed by the normal vectors meeting there [18] (Figure 2.5). It is also possible to see from Figure 2.5 that if the yield surface is straight, then all the positions on the straight line have the same normal vector, meaning that different stress states correspond to the same  $\dot{\epsilon}^p$ .

Equation (2.22) can be slightly rewritten, by using that  $\sigma_1 \geq \sigma_2 \geq \sigma_3$ . By doing

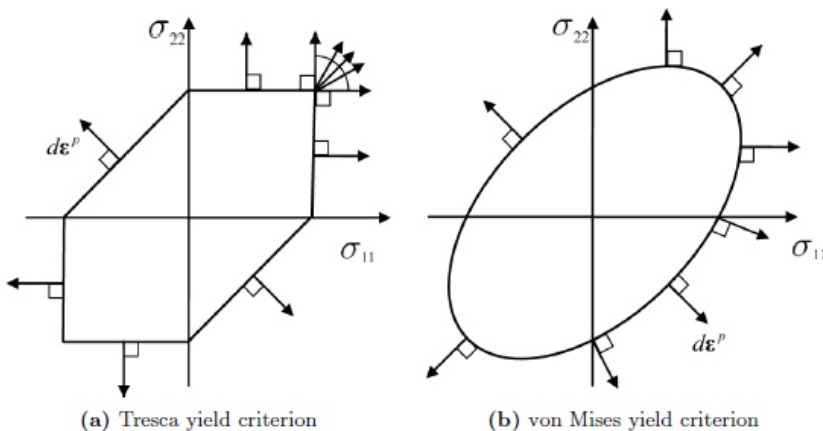


**Figure 2.5:** Geometric representation of the associated flow rule for Tresca and von Mises yield surfaces in case of plane stress. The associated flow rule implies that the incremental plastic strain vector is normal to the yield surface [17]. Where  $d\epsilon^p = \dot{\epsilon}^p dt$ .

## 2. Material Behaviour

---

this the absolute-signs can be ignored, and the yield criterion can be written as

$$f(\sigma_1, \sigma_2, \sigma_3) = \left( \frac{1}{2}((\sigma_1 - \sigma_2)^m + (\sigma_2 - \sigma_3)^m + (\sigma_1 - \sigma_3)^m) \right)^{\frac{1}{m}} - \sigma_Y = 0. \quad (2.27)$$

By use of this expression the principal plastic strain rate,  $\dot{\epsilon}_1^p$ , when defined in terms of the associated flow rule and the high-exponent yield criterion can be expressed as

$$\dot{\epsilon}_1^p = \frac{\dot{\lambda}}{2^{\frac{2}{m}}} \frac{(\sigma_1 - \sigma_2)^{m-1} + (\sigma_1 - \sigma_3)^{m-1}}{(\sigma_{eq}^h)^{m-1}}, \quad (2.28)$$

where  $\sigma_{eq}^h$  is the equivalent Hershey stress defined in Section 2.4.1. Similar expressions can be obtained for both  $\dot{\epsilon}_2^p$  and  $\dot{\epsilon}_3^p$ .



## 2.4 Scalar Measures of Stress and Strain

Practical scalar measures of stress and strain have been developed for simplification. Equivalent stress,  $\sigma_{eq}$ , and strain,  $\varepsilon_{eq}$ , will be presented along with the stress triaxiality ratio,  $\sigma^*$ , and the Lode parameter,  $\mu_\sigma$ . Equivalent stress and strain is related to the yield criterion, while the stress triaxiality ratio and the Lode parameter are practical measures when discussing failure (Chapter 3).

### 2.4.1 Equivalent Stress

One of the most commonly used measures of stress is the von Mises equivalent stress,  $\sigma_{eq}^m$ , which is a scalar measure of stress used to predict yielding. It was first formulated by James Clerk Maxwell in 1865, but it is generally attributed to Richard Edler von Mises (1913) [19]. It is related to the von Mises yield criterion (Section 2.3.1), which assume plastic yielding to only depend on the second principal invariant,  $J_2$ , of the deviatoric stress tensor.

The von Mises equivalent stress can be visualized if the state of stress in terms of principal stresses is plotted in a coordinate system of principal stresses (Haigh-Westergaard space). The von Mises equivalent stress can be found in the deviatoric plane illustrated in Figure 2.6. Any state of stress can be projected onto this plane, and the equivalent stress is the radial distance between origo and this

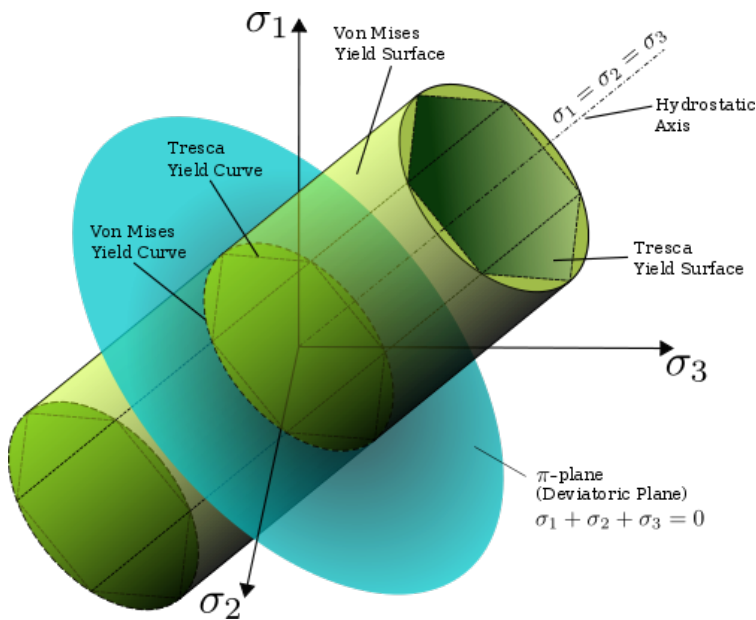


**Figure 2.6:** The von Mises yield surface; a cylinder parallel with the hydrostatic axis. The Tresca yield surface is also included for comparison. The blue surface illustrates any state of deviatoric stress only ( $\sigma_H = 0$ ) [19].

## 2. Material Behaviour

---

projected point. This relation is mathematically given as

$$\sigma_{eq}^m = \sqrt{\frac{(\sigma_1 - \sigma_2)^2 + (\sigma_2 - \sigma_3)^2 + (\sigma_1 - \sigma_3)^2}{2}}, \quad (2.29)$$

$\sigma_{eq}^m$  can also be calculated directly from the six variables of the Cauchy stress tensor.

It is important to note that the concept of equivalent stress is strongly related to the yield criterion used in the constitutive equations. Equation (2.29) can be interpreted as the equation of a circle expressed in the  $\pi$  - *plane* (Figure 2.6), and the circle expresses the yield surface related to the von Mises yield criterion. Yielding is defined to occur when  $\sigma_{eq}$  is equal to  $\sigma_Y$  (yield stress from uniaxial tension tests), according to the flow function (Section 2.3). Thus when the yield criterion is changed to for example the Tresca criterion, which has a more narrow yield surface, the definition of  $\sigma_{eq}$  must also be changed such that  $\sigma_{eq} = \sigma_Y$  is satisfied. This allows for definition of the equivalent Tresca stress

$$\sigma_{eq}^t = \frac{1}{2}(|\sigma_1 - \sigma_2| + |\sigma_2 - \sigma_3| + |\sigma_3 - \sigma_1|), \quad (2.30)$$

which can be interpreted as the equation of the Tresca yield surface also illustrated in Figure 2.6. In the same way also the equivalent Hershey stress,  $\sigma_{eq}^h$ , according to the Hershey yield criterion, can be defined as

$$\sigma_{eq}^h = \left( \frac{1}{2}(|\sigma_1 - \sigma_2|^m + |\sigma_2 - \sigma_3|^m + |\sigma_3 - \sigma_1|^m) \right)^{\frac{1}{m}}. \quad (2.31)$$

The definition of these equivalent measures of stress makes it possible to express the yield function only in terms of the equivalent stress,  $\sigma_{eq}$ , and yield stress,  $\sigma_Y$  as

$$f(\boldsymbol{\sigma}) = \sigma_{eq}(\boldsymbol{\sigma}) - \sigma_Y. \quad (2.32)$$

Here does  $\sigma_{eq}(\boldsymbol{\sigma})$  mean that the equivalent stress,  $\sigma_{eq}$ , is a function of the Cauchy stress tensor,  $\boldsymbol{\sigma}$ .

### 2.4.2 Equivalent Strain

The work conjugate scalar strain measure to von Mises equivalent stress,  $\sigma_{eq}^m$ , is the equivalent von Mises strain which can be defined as [20]

$$\varepsilon_{eq}^m = \sqrt{\frac{2}{3}\boldsymbol{\varepsilon}' : \boldsymbol{\varepsilon}'} = \sqrt{\frac{2}{3}\varepsilon'_{ij}\varepsilon'_{ij}}, \quad (2.33)$$

where  $\boldsymbol{\varepsilon}'$  is the deviatoric strain tensor. The equivalent von Mises strain,  $\varepsilon_{eq}^m$  can be decomposed in the same way as the strain tensor,  $\boldsymbol{\varepsilon}$  (Section 2.5)

$$\varepsilon_{eq}^m = \varepsilon_{eq}^e + \varepsilon_{eq}^p. \quad (2.34)$$

$\varepsilon_{eq}^p$  can be found as the sum of the equivalent plastic strain increments (Equation 2.40). It is however important to point out that  $\varepsilon_{eq}^e$  becomes much smaller than

$\varepsilon_{eq}^p$  in case of large plastic deformations. In such cases is  $\varepsilon_{eq} \approx \varepsilon_{eq}^p$ .

When the yield criterion is changed, e.g. from the von Mises criterion to the Hershey criterion, the equivalent stress measure is changed. In order to maintain work conjugacy ( $\boldsymbol{\sigma} : \boldsymbol{\varepsilon} = \sigma_{eq} \varepsilon_{eq}$ ) the equivalent strain is also changed. However when using the associated flow rule this adoption is done automatically since the equivalent plastic strain increment is calculated directly from the gradient vector of the flow function.

### 2.4.3 Stress Triaxiality Ratio

Even though equivalent stress is a very practical measure predicting plastic deformation, it is insufficient as a single measure when it comes to predicting fracture. This is because fracture depend on the hydrostatic stress, whereas plastic deformation does not. It is therefore useful to introduce the stress triaxiality ratio,  $\sigma^*$ , which indicates the amount of hydrostatic stress relative to the equivalent stress

$$\sigma^* = \frac{\sigma_H}{\sigma_{eq}}. \quad (2.35)$$

### 2.4.4 Lode Parameter

Recent experimental and numerical studies show that it might be insufficient to characterize the stress state only in terms of the stress triaxiality when it comes to describing fracture [21]. This is especially true when the second principal stress,  $\sigma_2$ , is of major importance [22]. In such cases the Lode parameter can give a more complete description of the stress state. The Lode parameter is defined as

$$\mu_\sigma = \frac{2\sigma_2 - \sigma_1 - \sigma_3}{\sigma_1 - \sigma_3}, \quad (2.36)$$

where  $\sigma_1$ ,  $\sigma_2$  and  $\sigma_3$  are the principal stresses.  $\mu_\sigma$  will vary between -1 and 1, where:

- $\mu_\sigma = -1$  characterize an axisymmetric state of stress.
- $\mu_\sigma = 1$  is when the second principal stress is equal to the major principal stress ( $\sigma_1 = \sigma_2 > \sigma_3$ ).
- $\mu_\sigma = 0$  is when the second principal stress is equal to the hydrostatic stress,  $\sigma_H$ .

## 2.5 Strain Decomposition

For metals the total strain,  $\varepsilon_{ij}$ , can be decomposed into an elastic reversible part,  $\varepsilon_{ij}^e$ , and a plastic irreversible part  $\varepsilon_{ij}^p$

$$\varepsilon_{ij} = \varepsilon_{ij}^e + \varepsilon_{ij}^p. \quad (2.37)$$

$\varepsilon_{ij}^p$  is path dependent, and its evolution is defined through the associated flow rule  $\dot{\varepsilon}_{ij}^p = \dot{\lambda} \frac{\partial f}{\partial \sigma_{ij}}$ , where  $f$  is the flow function defining the yield criterion (Section 2.3.2).

If von Mises plasticity is assumed (material isotropy and isovolumetric plastic deformation), the plastic strain rate,  $\dot{\varepsilon}_{ij}^p$ , is proportional to  $\frac{\partial f}{\partial \sigma_{ij}}$  and the plastic multiplier,  $\dot{\lambda}$ , is identified as the equivalent plastic strain rate,  $\dot{\varepsilon}_{eq}^p$ . If the plastic strain rate tensor,  $\dot{\varepsilon}_{ij}^p$ , is multiplied with a time increment,  $dt$ , the incremental plastic strain tensor ( $dt\dot{\varepsilon}_{ij}^p = d\varepsilon_{ij}^p$ ) can be written as

$$d\varepsilon_{ij}^p = d\varepsilon_{eq}^p \frac{\partial f}{\partial \sigma_{ij}}. \quad (2.38)$$

Here  $d\varepsilon_{eq}^p$  is the equivalent plastic strain increment, corresponding to a given load increment.  $d\varepsilon_{eq}^p$  is found through an iterative process where equilibrium between external loading and material response of the structure is searched. The total plastic strain is then found as the sum of the plastic increments corresponding to the incremental load steps

$$\varepsilon_{ij}^p = \sum_n d\varepsilon_{ij}^{p,n}, \quad (2.39)$$

where  $n$  denotes the total number of time increments in the simulation. The total equivalent plastic strain is given in the same way as

$$\varepsilon_{eq}^p = \sum_n d\varepsilon_{eq,n}^p. \quad (2.40)$$

## 2.6 Work Hardening

### 2.6.1 Isotropic Hardening

Isotropic hardening is defined as the increase in strength of the material due to plastic deformation, i.e. the yield stress,  $\sigma_Y$ , increases. Plastic deformation usually occurs by the movement of dislocations in the atomic lattice in most metals. The movement of such dislocations is restricted by grain boundaries and other dislocations. Plastic deformation is also associated with the formation of new dislocations which inhibits the movement of the already existing dislocations [23]. This effect is perhaps better known as strain hardening, and causes the yield surface to increase in size. The size of the yield surface is determined by the yield stress,  $\sigma_Y$ , and the evolution of  $\sigma_Y$  during plastic deformation is described through the hardening law.

Slåttedalen and Ørmen [1] used isotropic hardening in the constitutive equations. Isotropic hardening means the yield strength is equally increased in all directions (in stress-space) when plastic deformation occurs in one direction, i.e. if plastic deformation occurs in compression such that the yield strength is increased, the yield strength in tension will equivalently increase at the same time. Isotropic hardening can be modeled using the Voce-hardening law, where the yield strength is written as a function of the equivalent plastic strain,  $\varepsilon_{eq}^p$ .

$$\sigma_Y(\varepsilon_{eq}^p) = \sigma_0 + \sum_{i=1}^N Q_{R_i} (1 - \exp(-\frac{\theta_{R_i}}{Q_{R_i}} \varepsilon_{eq}^p)), \quad (2.41)$$

where  $\sigma_0$  is the initial yield stress before hardening. For further details about how the strain hardening effect is modeled it is referred to one of the previous thesis, for example [5].

### 2.6.2 Kinematic Hardening

In contrast to the enlargement of the yield surface during plastic deformation caused by isotropic hardening the yield surface may also translate in stress space, and this effect is known as kinematic hardening. Kinematic hardening is caused by the variation of grain orientation in the microstructure of a polycrystalline metal like X65 steel. The microscopic grains will due the different orientations deform plastically with different ease when exposed to macroscopic loading. Thus will plastic deformation begin in the most favorably oriented grains meaning that the amount of plastic strain after deformation will vary from grain to grain.

Due to this effect residual stresses between the different grains will be present after unloading, such that some grains will start to yield earlier when the load is reversed and the yield stress will by that be reduced. This effect is also known as the Bauschinger effect [24]. Fornes and Gabrielsen [2] and Aune and Hovdelien [3] investigated this effect and included it in the constitutive equations with use of the non-linear relation proposed by Armstrong-Fredericks. The yield function is

## 2. Material Behaviour

---

firstly modified such that a backstress tensor,  $\boldsymbol{\chi}$ , representing the residual stresses in the material after plastic deformation, is included

$$f(\boldsymbol{\sigma}, \boldsymbol{\chi}) = \sigma_{eq}(\boldsymbol{\sigma} - \boldsymbol{\chi}) - \sigma_Y, \quad (2.42)$$

where  $\sigma_{eq}(\boldsymbol{\sigma} - \boldsymbol{\chi})$  express that the backstress need to be subtracted from the Cauchy stress tensor before calculating the equivalent stress. The evolution of  $\boldsymbol{\chi}$  is then calculated using the Armstrong-Fredericks equation which can be expressed as

$$\dot{\boldsymbol{\chi}} = \sum_{i=1}^N \theta_{\chi_i} \left( \frac{\boldsymbol{\sigma} - \boldsymbol{\chi}_i}{\sigma_{eq}(\boldsymbol{\sigma} - \boldsymbol{\chi}_i)} - \frac{\boldsymbol{\chi}_i}{Q_{\chi_i}} \right) \dot{\epsilon}_{eq}^p. \quad (2.43)$$

For further details about the mathematics needed to describe this effect it is referred to one of the previous thesis, for example [4].

It is important to note that a combination of isotropic and kinematic hardening is fully possible.

## 2.7 Viscoplasticity

The evolution of the yield stress for steels when exposed to plastic straining is usually rate-dependent. This was also shown to be the case for the X65 steel, when uniaxial tension tests were performed at elevated strain rates using the Split-Hopkinson bar [1]. The tests displayed an increase in stress for a given amount of strain at elevated strain rates. The theory describing rate-dependent plastic behaviour of solids is called viscoplasticity. The viscoplastic behaviour of metals is related to the movement of dislocations in the grains of the material associated with plastic deformation, with superposed effects of inter-crystalline gliding [25].

When viscoplasticity is included in the constitutive equations the flow function,  $f(\boldsymbol{\sigma})$ , is allowed to take positive values, contrary to what was defined in the case of rate-independent behaviour (Equation (2.18)). Plastic deformation is instead defined to occur when  $f(\boldsymbol{\sigma}) > 0$  and the elastic domain is now defined as  $f(\boldsymbol{\sigma}) \leq 0$ . I.e. the stress state,  $\boldsymbol{\sigma}$ , is allowed to move outside the yield surface. The plastic strain rate will in some way depend on the value of  $f(\boldsymbol{\sigma})$ . Thus when  $\boldsymbol{\sigma}$  take on a values outside the yield surface the material will start to plastically deform as a function of time. As the material plastically deforms the yield surface will increase in size in case of isotropic hardening, such that the surface eventually reaches  $\boldsymbol{\sigma}$  and plastic deformation stops. This process is known as creep, and the above explanation assume  $\boldsymbol{\sigma}$  to be constant with time after application.

The dimensionless relative strain rate can be defined as

$$\dot{\varepsilon}_{eq}^{p,*} = \frac{\dot{\varepsilon}_{eq}^p}{\dot{\varepsilon}_{eq}^{p,0}} = \max \left( \left( \frac{\sigma_{eq}}{\sigma_Y} \right)^{C_\sigma} - 1, 0 \right). \quad (2.44)$$

Here  $\dot{\varepsilon}_{eq}^p$  is the plastic strain rate,  $\dot{\varepsilon}_{eq}^{p,0}$  is the reference plastic strain rate and  $C_\sigma$  define the strain-rate dependency of the material. By using this definition the flow function can be written as

$$f(\boldsymbol{\sigma}) = \sigma_{eq} - \sigma_Y \left( 1 + \dot{\varepsilon}_{eq}^{p,*} \right)^{C_\sigma}. \quad (2.45)$$





## Chapter 3

# Failure

A material model is not complete until one is able to predict when the material fails (i.e. fractures). Fracture in a metal is typically characterized by growth or multiplication of macroscopic cracks [22]. The origin of these cracks lies in the microscopic defects in the material and all materials contains defects of various types and scales [23]. From the atomic scale with point defects in the atomic lattice to larger scale with second phase particles or inclusions. How these cracks nucleate and grow depend on many different factors (e.g. type of material, temperature, stress triaxiality etc.). The challenge is to relate the nucleation and growth of these cracks, which eventually may lead to global fracture, to the global loading of the structure.

### 3.1 Theory

Fracture in metals is typically characterized as either ductile or brittle. Classification is based on the ability of the metal to experience plastic deformation and energy absorption before fracture. The two modes are relative terms, meaning that a particular metal may fail in a ductile manner in one situation or in a brittle in another, dependent on the stress state, stress history, temperature and strain rate [23].

#### 3.1.1 Ductile Fracture

Ductile fracture is the result of nucleation, growth and coalescence of microscopic voids that initiate at inclusions and second-phase particles [26], the typical process of how such microscopic voids grow and coalesce into a macroscopic fracture is shown in Figure 3.1.

##### Void Nucleation

Voids form around a second-phase particle or inclusion when sufficient stress is applied to break the interfacial bonds between the particle and the matrix [22]. How these voids nucleate depend on the state of stress (Figure 3.2) and in case of multi-axial compressive loads voids may actually not open at all, in spite a large magnitude of plastic deformation (void locking Figure 3.2). How easy these voids nucleate depend on multiple factors:

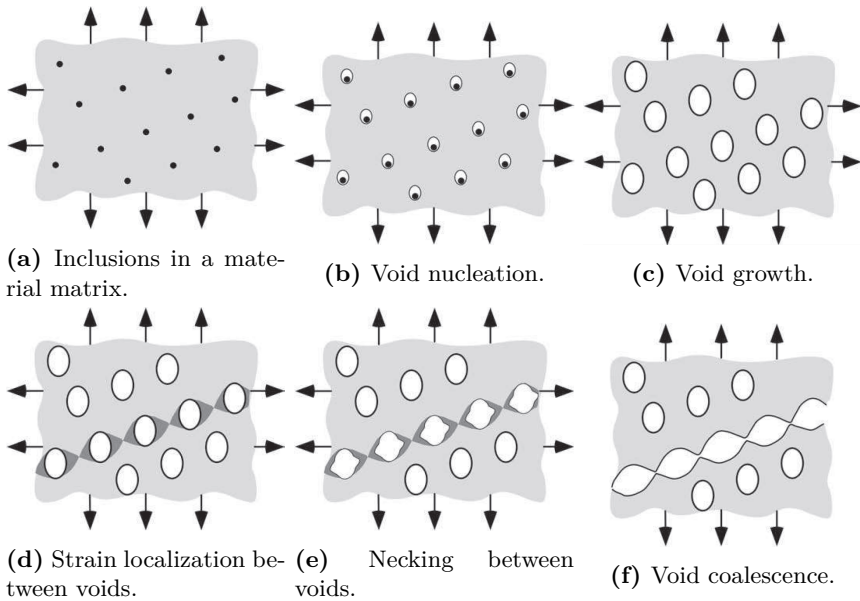


**Figure 3.1:** Void nucleation, growth and coalescence in case of ductile fracture [26].

- Particle size; voids nucleate first on the largest particles [22].
- Stress triaxiality; nucleation increases with hydrostatic stress and how the voids nucleate will depend on the stress state [26] [27].
- Bonding between the second-phase particles and the matrix; voids will more easily nucleate if the interfacial bonding is weak [22].

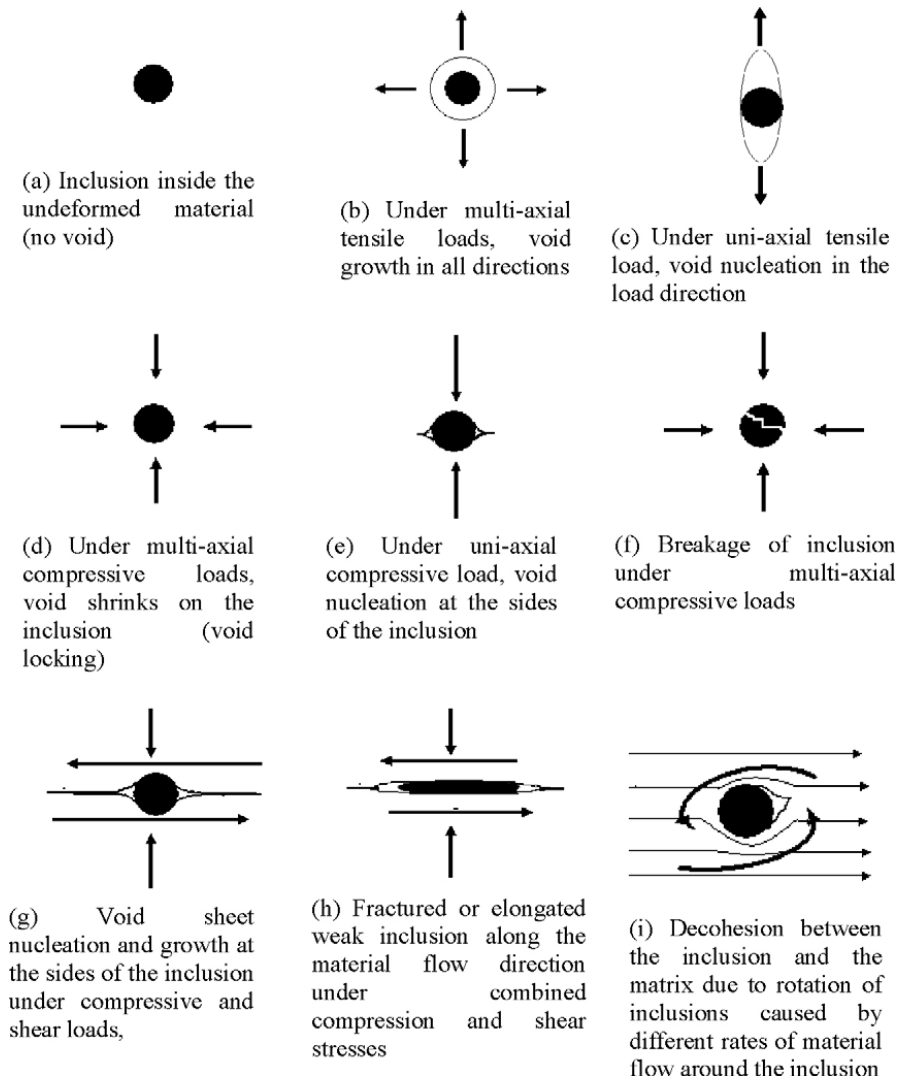


**Figure 3.2:** Illustrations of void nucleation mechanisms around a inclusion under different stress states [27].

### Void Growth

The most important macroscopic observation about ductile fracture is that the fracture strain decreases exponentially with increasing stress triaxiality. This effect is directly related to a significant increase of the void growth rate with an increasing stress triaxiality ratio [22]. The opposite effect is shown in case of negative stress triaxiality, i.e. compressive hydrostatic stress. It is assumed that voids stop to grow when the stress triaxiality get sufficiently low, i.e. the compressive hydrostatic stress is so high that it is impossible for voids to grow (illustrated in Figure 3.2 as void locking). Bao and Wierzbicki [28] proposed a cut-off value of  $-1/3$  on the stress triaxiality ratio, below which fracture never occurs based on their experiments on 2024-T351 aluminum and 1045 steel.

The fracture strain versus stress triaxiality plot from their experiment on 2024-T351 aluminum is illustrated in Figure 3.3. Bao and Wierzbicki [28] also found a change of slope when the average stress triaxiality ratio was around 0.4, however this effect may also be caused by their specific experimental setup and thus not be a universal phenomena describing all cases of loading and metals.

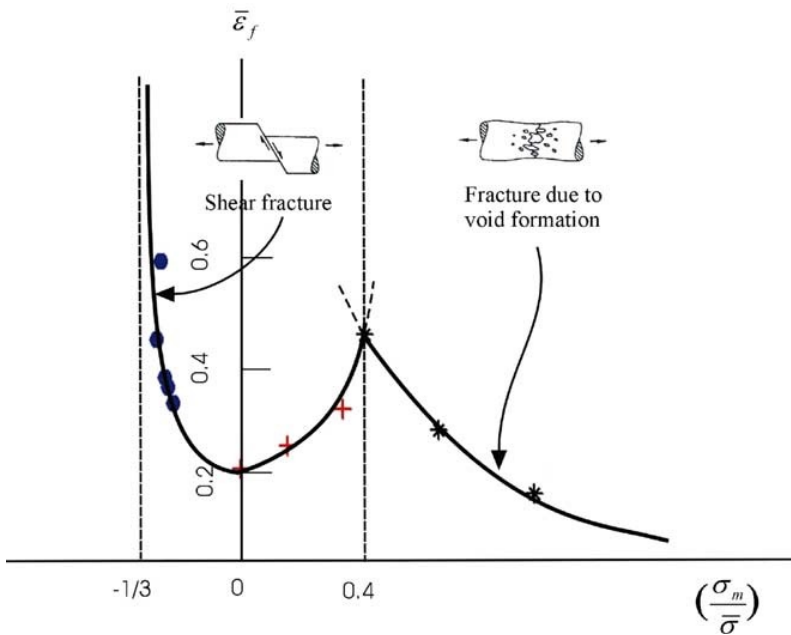


**Figure 3.3:** The equivalent strain to fracture plotted against the average stress triaxiality ratio during the tests. This plot is for an 2024-T351 aluminum alloy, but a similar curve was found for 1045 steel also with a cut-off value at  $-1/3$  [28].

### Void Coalescence

As the voids continues to grow coalesce will eventually happen (Figure 3.1). As long as the voids remain small it can be assumed that they grow independently in a stable manner, i.e. an increase in stress is needed for further growth [23]. When the voids reach a certain size the neighbouring voids will interact and cause strain localization between the voids, the stress concentration around the void increases, the process becomes unstable, resulting in void coalescence and the creation of a macroscopic crack. These cracks may then grow, or open up, in different ways dependent the stress state, as illustrated in Figure 3.4.

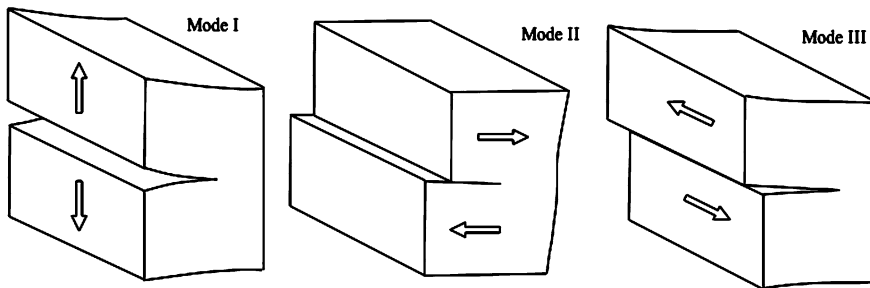


**Figure 3.4:** Different modes of crack opening. Mode I, opening or tensile mode; mode II, sliding mode; and mode III, tearing mode [22].

### 3.1.2 Brittle Fracture

Brittle fracture take place without any appreciable deformation and by rapid crack propagation in an unstable manner [23]. Fracture surfaces of materials that failed in a brittle manner will typically be relatively flat and the fracture is characterized as either cleavage (through the interior of grains) or intergranular (along grain boundaries)(Figure 3.5).

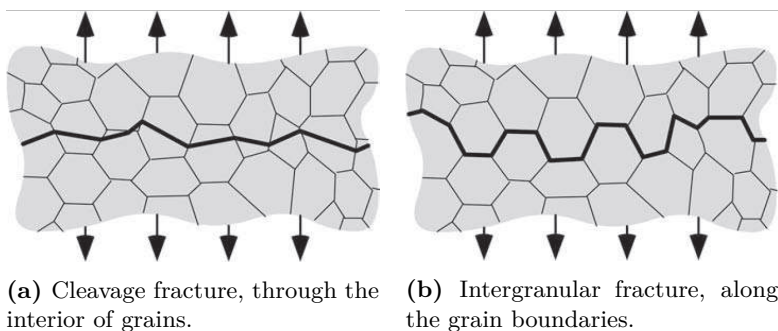


**Figure 3.5:** Different brittle fracture modes [26].

#### Intergranular Fracture

Intergranular fracture occurs when the grain boundaries are the preferred fracture path in the material [26]. Fracture occurs by breakage of interatomic bonds and the breakage path chosen will be the path that requires the least energy. An indication of the energy required to break such interatomic bonds between two fracture planes, created by either cleavage or intergranular fracture, can be found by comparing the surface energies [22]. This theoretical approach lead to the conclusion that intergranular fracture is the preferred fracture path in iron. However, the observation from experiments is that brittle fracture usually occurs by cleavage in most metals [26], because segregation of impurities like carbon (important component in steel) in iron tend to suppress intergranular fracture [22].

#### Cleavage

Crack propagation by cleavage corresponds to the successive and repeated breaking of atomic bonds along specific crystallographic planes across each grain [23]. The orientation of the cleavage planes varies from grain to grain since each grain will have a random orientation, this leads to a somewhat grainy surface. An example of such a surface is shown in Figure 3.11.

A theoretical value of the stress required to fracture a surface by cleavage can quite easily be calculated if the bonding energy between the atoms located across

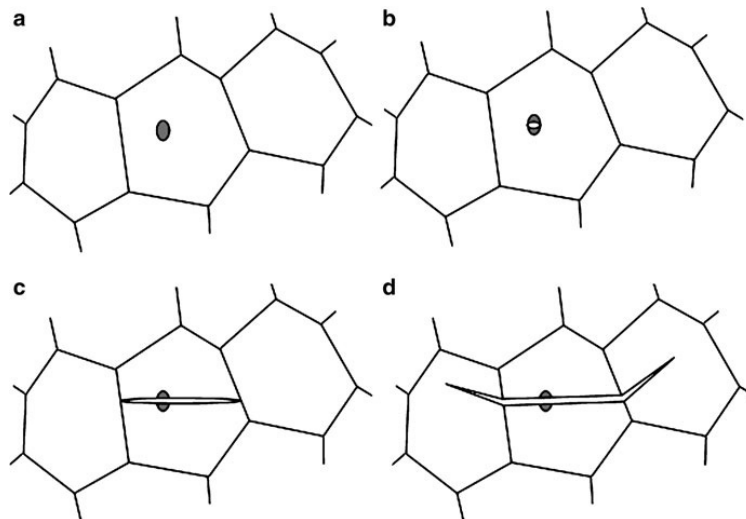


**Figure 3.6:** Schematic representation showing how cleavage initiates when a brittle second phase particle cracks and creates a microcrack. It also shows how the propagating direction changes when the crack propagates into the neighbouring grains [22].

the cleavage plane is known. The experimental global cleavage stress is however much less, but the theoretical values may be reached on a local microscopic level due to stress concentrations. Such stress concentrations are typically found in steels to be caused by brittle second phase particles which are trapped in the matrix [22]. Figure 3.6 illustrates how this happens. Dislocations and twins may also cause such microscopic stress concentrations, but this is a less common effect in steels [26].

### 3.1.3 Dynamic Mechanisms

#### Adiabatic Shear Localization

In case of very high deformation rates, so-called adiabatic shear bands may develop: zones of intense shear strain called shear bands (Figure 3.7). These bands develop due to rapid local heating, resulting from dissipated heat due to intense plastic shear deformation. This thermal heating causes the material to soften. If the thermal softening increases faster than the hardening due to plastic deformation the plastic deformation will become unstable. The adjective "adiabatic" is used to emphasize that the heat generated in the shear bands is significantly greater than the heat lost [29].

Adiabatic shear bands is closely related to cracking, but it is not, generally speaking, a crack since it does not directly imply separation of two surfaces. It can be looked upon as a highly localized mode of deformation which eventually may lead to global failure of the structure. However the final fracture may develop along these shear bands, shown in Figure 3.7.

The energy needed to create failure for a given load case by adiabatic shear banding may be less than failure by other "regular" modes. But the occurrence of adiabatic shear banding is dependent on very high deformation rates (e.g. pen-

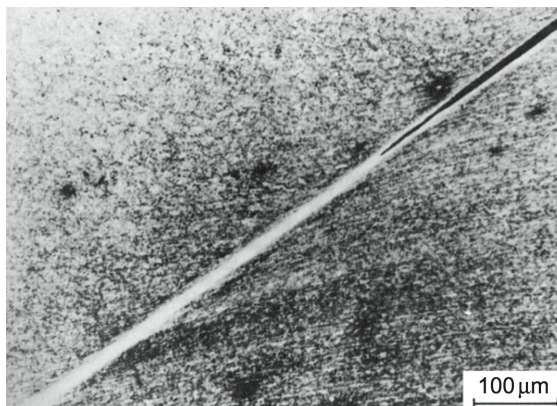


**Figure 3.7:** Adiabatic shear band and an associated crack in a martensitic steel deformed in a dynamic compression test [30].

### 3. Failure

---

etration of bullets). The heat generated in the shear bands must not have the time to dissipate to the surrounding material such that the thermal softening outweighs the strain hardening effect.

#### Spall Fracture

Spall fracture is a shock-induced dynamic fracture mode caused by wave propagation through the material after dynamic impact. It can be defined as fracture that occurs simultaneously over an area, not by growth of a single macrocrack, but by the nucleation and growth of many cracks, or voids at essentially the same time. This may be caused by tensile waves produced when compression waves are reflected from a boundary. The fracture initiates at the interior of the solid and can cause flakes of the material to be broken off [31]. Spall fracture is an evolutionary process, Figure 3.8 illustrates how such a crack may evolve and finally cause a flake of material to be broken off when loading is increased.

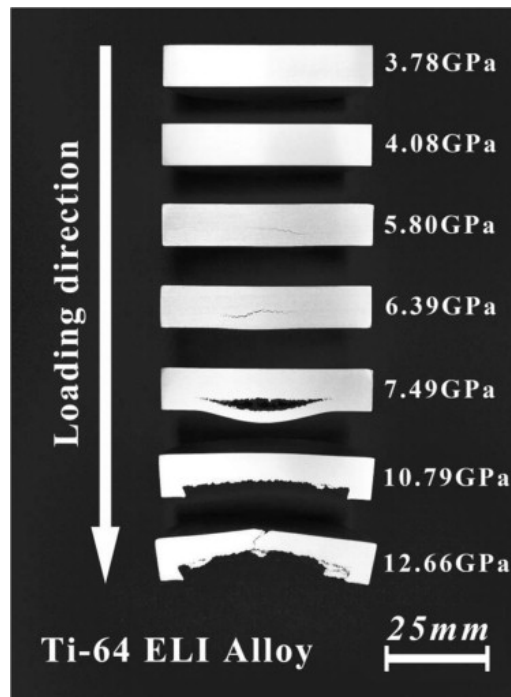


**Figure 3.8:** Illustration of spall fracture and how it develops for increasing shock pressures on a plate of a Ti-6Al-4V alloy [32].



## 3.2 Previous Findings

Many experiments and metallurgical investigations have been conducted over the years as part of this ongoing project on X65 steel pipes. Tests on both the pipe itself and uniaxial material tests of different kinds have been carried out, with subsequent metallurgical investigation of some of the tests. The previous findings most relevant to this thesis with regard to fracture will now be presented.

### 3.2.1 X65 Steel

The X65 steel is one of the most used steel grades in the offshore piping industry due to its strength and low cost. The X65 steel has a rather low carbon content of 0.09 wt%C [33], making it a rather ductile material. It has a ferritic micro structure made of pearlite and ferrite grains [34] (Figure 3.9). Ferrite is a Body Centred Cubic (BCC) structured iron and pearlite is made of alternating layers of ferrite and a iron carbide termed cementite ( $Fe_3C$ ). Ferrite is rather soft and ductile, while pearlite has properties intermediate between the soft ferrite and the hard, brittle cementite [23]. In addition to carbon, the main quantities found where: 0.25%Si, 1.13%Mn, 0.04%Cr, 0.09%Mo, 0.09%Cu and 0.06%V [7].

The pipes discussed in this thesis have been produced by the Argentinian supplier Tenaris according to guidelines given in DNV-OS-F101 [35]. The pipes are made seamless utilizing a production technique known as the Mannesmann process.

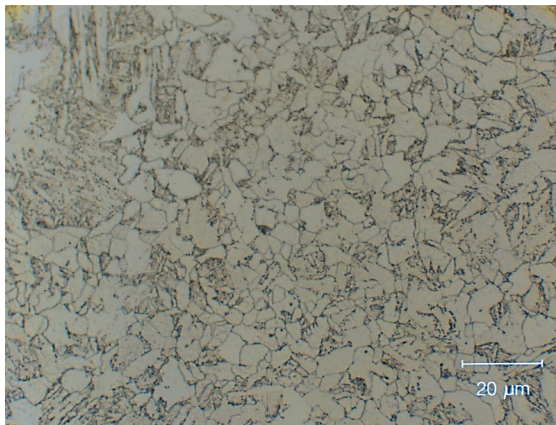


**Figure 3.9:** Microstructure found in the pipe wall [36].

#### 3.2.2 Component Tests

For details about the experimental setup it is referred to [1]

##### Dynamic Impact and Subsequent Quasi-Static Stretching (Pipe A, B, C and D)

A fracture observed in pipes exposed to a high impact velocity ( $> 5\text{m/s}$ ,  $1472\text{kg}$ ) and the entire load sequence (impact and stretching) is given in Figure 3.10. The pictures illustrate a fracture that developed during subsequent quasi-static stretching (pipe B), after impact. A visible through-the-thickness crack developed almost immediately during stretching [1, 37]. A more detailed investigation of the fracture surface with use of Scanning Electro Microscopy (SEM) revealed both a brittle and a ductile fracture surfaces. A brittle fracture surface (cleavage) was found in zone 1, while a ductile was found in zone 2. A transition between a ductile and a brittle fracture surface was found in zone 3 as a ductile "ridge". The difference between the fracture surface in zone 1 and 2 is shown in Figure 3.11.

The two images clearly visualize the difference between the two fracture modes. While the cleavage surface is relatively plane due to transgranular fracture, the ductile fracture surface has a much more dimpled appearance due the creation of microvoids prior to coalescence and global fracture. Small particles were also found at the bottom of the dimples which indicate that voids probably nucleated around these particles [37].

This observation of ductile and brittle behaviour in the same fracture indicate that a local transition from ductile to brittle behaviour has taken place. Ductile to brittle transition is typically caused by a shift in temperature [26]. However this can probably not explain the above mentioned observation since temperature

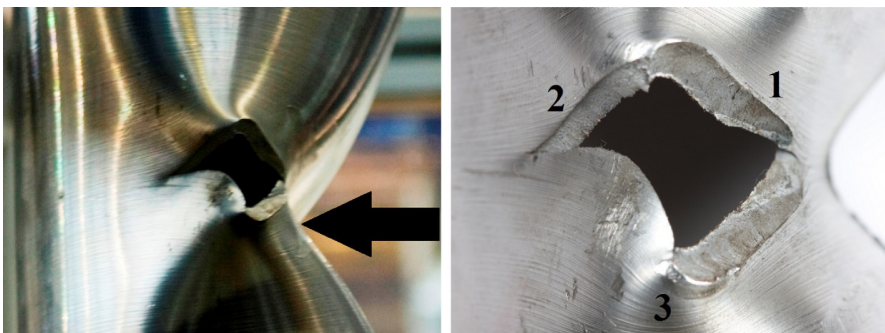


**Figure 3.10:** Fracture observed in pipe B exposed to both dynamic impact and stretching. This pipe was impacted with a trolley velocity of  $5.13\text{ m/s}$ , with mass equal to  $1472\text{ kg}$ . The fracture is characterized by different zones which exhibits different characteristics. The arrow indicates the direction of impact. [37].

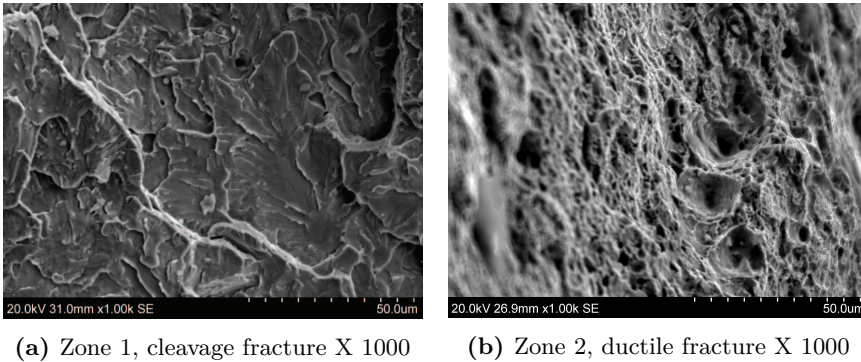


**Figure 3.11:** Comparison of the fracture surfaces of zone 1 and 2 [37].

is assumed approximately constant. A more likely explanation can be that the brittle behaviour in zone 1 is caused by a higher degree of plastic deformation compared to zone 2 and 3, when the pipe was bended during impact. Zone 1 is positioned on the "inside" of the dent FEA [1, 3] indicated that the largest amount of plastic deformation occur in this zone during impact, in a compressive state of stress (negative stress triaxiality). Less plastic deformation is predicted to occur in zone 2. I.e. a large amount of plastic deformation during impact in a compressive state might restrict plastic deformation during stretching in zone 1 (in a tensile state), such that the material fail in a brittle mode, according to Anderson [26], which states that brittle fracture occur when plastic deformation is restricted.

An observation worth mentioning is that the fracture in zone 1 seems to have developed as mode I, opening, while the fracture in zone 2 seems to have developed through mode III, tearing, with reference to Figure 3.4.

It is important to note that this pipe (pipe B), was exposed to a very high degree of deformation during impact. The diameter at midspan was reduced from 122.80 mm to 22.5 mm, i.e. almost dented flat. Pipes impacted at a lower velocity, did also show visible fracture after stretching. However to a much less extent. The pipe A experiment (3.24m/s, 1472kg) resulted in a diameter reduction at midspan from 122.56 mm to 60 mm during impact, and visible surface cracks was observed to developed during stretching (Figure 3.12).

### Impact Only (Pipe K and L)

Slåttedalen and Ørmen [1] discovered visible cracks that developed during stretching after all cases of loading (impact velocity varying between 2.7 to 5.1 m/s). It was therefore of interest to investigate if cracks developed already after impact. Aune and Hovdelien [3] carried out new tests with the same boundary conditions and impact velocities as Slåttedalen and Ørmen, but without subsequent stretch-

### 3. Failure

---



**Figure 3.12:** Surface fracture observed on pipe A, exposed to both dynamic impact and stretching. This pipe was impacted with a trolley velocity of 3.24 m/s, with mass equal to 1472kg [37].

ing.

What they found was indeed very interesting. Both internal<sup>1</sup> and external<sup>2</sup> 75% through-the-thickness cracks was found in the compressive zone in case of 5.2 m/s impact velocity (pipe K), illustrated in Figure 3.13. This impact velocity caused a large amount of global deformation. The diameter at midspan was reduced from 122.46 mm to approximately<sup>3</sup> 27 mm, i.e. almost dented flat. However, their test with 3.26 m/s impact velocity (diameter reduction from 122.47 mm to 73.40 mm) revealed microscopic internal cracks ranging between 20-300  $\mu\text{m}$  (Figure 3.14). Smaller surface cracks were also found. It should be noted that such cracks are very hard to detect by non-destructive inspection. The integrity of the pipe is severely reduced due to potential local stress concentrations caused by the cracks.

It is hard to believe that these cracks open during compression (Figure 3.2), the spring back phase is therefore assumed to be responsible for crack opening. The spring back phase is caused by stored elastic forces which builds as the pipe is bended and causes the pipe and trolley to spring back. This spring back change the state of stress from compression to tension inside the dent, such that cracks may open. This is a very interesting discovery because it indicates that fracture might be dynamically dependent, such that quasi-static testing is not sufficient. In addition, the discovery of internal cracks, indicates that visual inspection of the pipe surface after impact is not necessarily sufficient.

---

<sup>1</sup>No connection to the surface

<sup>2</sup>Connection to the surface

<sup>3</sup>Difficult to measure the diameter exactly



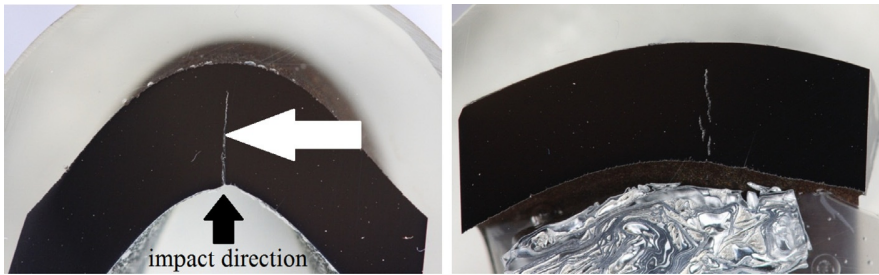


**Figure 3.13:** External and internal cracks found in the 5.2  $m/s$  impact experiment after impact only (pipe K) [37].

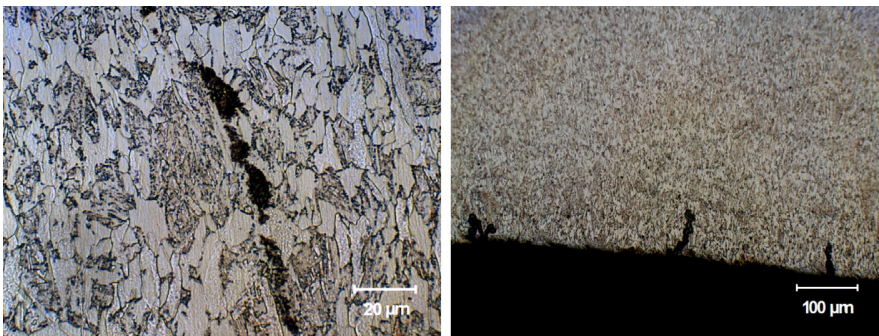


**Figure 3.14:** Examples of internal and external surface cracks found in the 3.26  $m/s$  impact experiment after impact only (pipe L) [37].

### 3.2.3 Uniaxial Compression-Tension Tests

#### Smooth Specimens

Uniaxial tension tests were conducted by Slåttedalen and Ørmen [1] on smooth axisymmetric specimens (Figure 3.19). The fracture surface was investigated two years later as part of the thesis written by Aune and Hovdelien [3] and revealed a typical ductile surface; "cup-and-cone" with a clearly dimpled surface.

#### Notched Specimens

Aune and Hovdelien [3] carried out a more detailed investigation two years later. They followed up the work done by Fornes and Gabrielsen [2] the former year by doing uniaxial compression-tension test with pre-compressive strain up to 40% with subsequent tension until failure on notched specimens 3.20. SEM investigation of the fracture surface revealed a clearly dimpled surface on all specimens, indicating ductile fracture. A relative plot of the true stress-strain curve is given in Figure 3.16. Here only the part with a positive true stress is plotted, and each curve has been translated along the strain-axis such that the plot begin in origo. The strain is calculated as  $\varepsilon_{t,rel} = \ln(A_r/A)$ , where  $A_r$  is taken as the cross-sectional area after pre-compression (zero loading). Both the absolute fracture

### 3. Failure

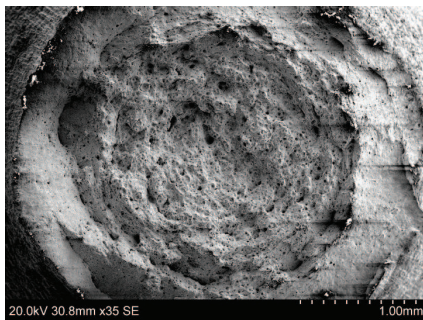
---

strain,  $\varepsilon_{abs}^f = \ln(A_0/A_f)$ , and relative fracture strain,  $\varepsilon_{rel}^f = \ln(A_r/A_f)$ , where  $A_0$  is taken as the initial cross sectional area before compression, displayed a drop in fracture strain in case of pre-compression [37].

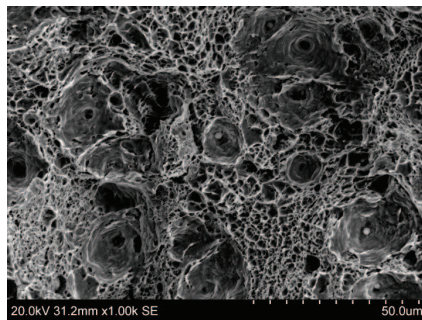
Closer investigation with use of SEM revealed what seemed to be a crushed particle at the bottom in many of the dimples observed on fracture surface (Figure 3.15 and 3.2). Investigation of the undeformed material revealed a matrix which consisted of iron, manganese and carbon. Two types of particles trapped within the matrix were found, denoted as particle 1 and 2. Particle 1 was spherical in shape and its diameter varied between 2-25  $\mu m$ , it consisted mainly of calcium aluminate, it was in-homogeneously distributed and seemed to be poorly bonded to the matrix. The poorly bonding to the matrix is believed to cause stress concentrations such that voids may nucleate around these particles (Subsection 3.1.1), and it is believed that it was these particles that were seen at the bottom in many of the dimples. Particle 2 was angular in shape, much less numerous and their typical size was about 5  $\mu m$ . Titanium was the main component of these particles and the particle seemed to be well bonded to the matrix [37].

Based on these tests it is reasonable to assume that the fracture strain depends on both the stress history and the stress state (influenced by the specimen geometry).

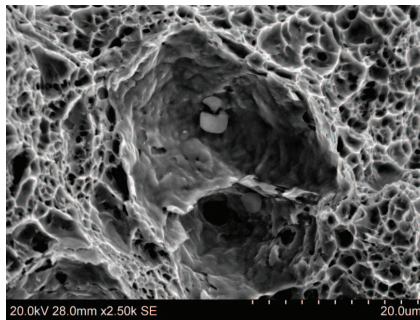
Compression-tension tests from 40% to 100% pre-compressive strain were carried out by [37]. However, with a different geometry (Figure 3.21) to avoid buckling. A similar relative true stress-strain plot as was given in Figure 3.16 is given in Figure 3.17, where the curves are translated along the strain-axis to ease comparison of the fracture strain after pre-compression. Figure 3.17 shows the same trend as Figure 3.16. The relative fracture strain reduced with an increasing amount of pre-compression.



(a) Magnification X 35



(b) Magnification X 1000



(c) Magnification X 2500

**Figure 3.15:** Fracture surface on a uniaxial compression-tension test pre-compressed up to 10% compressive strain, pictured at different magnifications [3].

### 3. Failure

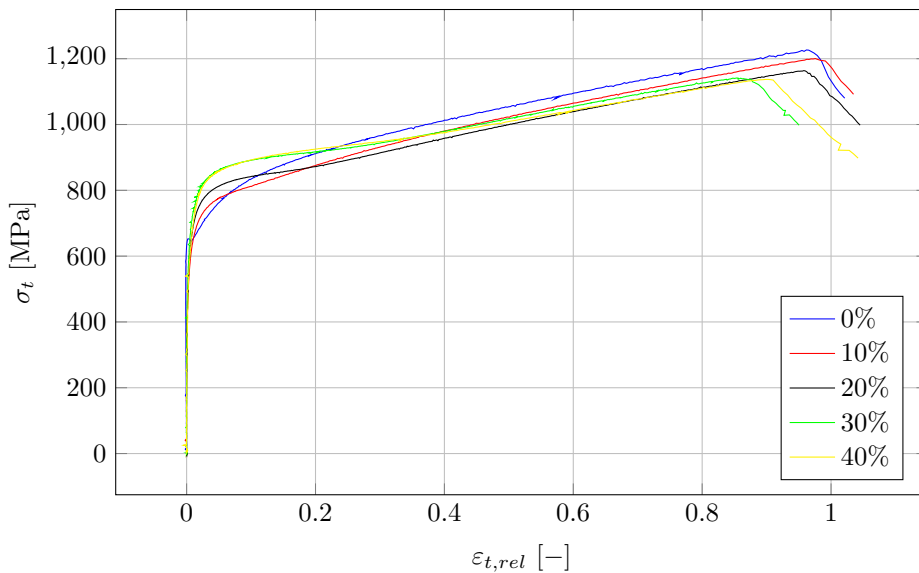


**Figure 3.16:** True stress-strain after different amounts of pre-compressive strain on notched specimens (Figure 3.20).

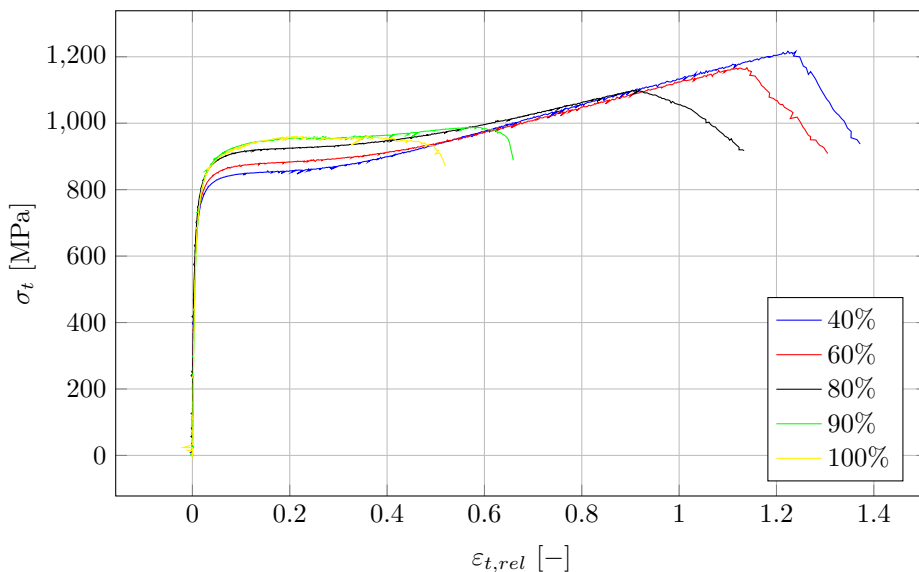


**Figure 3.17:** True stress-strain after different amounts of pre-compressive strain on notched specimens (Figure 3.21). The two specimens exposed to 90 and 100% failed in a shear mode instead of cup-and-cone.



### 3.3 Fracture Criterion

A fracture criterion can be used to predict when the pipe material fails when carrying out FEA. Fracture is a very complex process, depending on many factors. It is therefore difficult to determine a general precise criterion applicable to all types of fracture. It is thus of great help to capture strain localization. Strain may initially be distributed quite homogeneously over a certain area of the component. When straining start to localize, the strain rate may exponentially increase in the respective area when the component is further deformed (e.g. necking when performing tensile tests). Meaning that the fracture criterion itself not necessarily needs be very accurate as long as the numerical model is able to capture strain localization.

Localization is potentially caused by stress concentrations which can occur on different scales. It can be caused by geometrical forms such as sharp edges, or on a smaller scale by for example lathing grooves or corrosion at the surface of the component. Stress concentrations may also be present on a much smaller scale by inclusions or second phase particles trapped within the matrix of the material. I.e. that the ability of the numerical model to capture fracture will depend on the geometric "resolution".

#### 3.3.1 Coupled Approach

Ductile fracture in metals is not a sudden process, but instead a process of nucleation, growth and coalescence of microscopic voids. Such voids will influence the integrity of the metal and make it softer. In the coupled approach the evolution of such voids is modeled and coupled with the constitutive equation. This is usually done by introducing a damage variable,  $\omega$ , which model the reduction of the effective stress area when voids develop [17].  $\omega$  is zero for an undamaged material and unity for a fully damaged material. The stress-strain relation can be written as

$$\sigma_{ij} = (1 - \omega)C_{ijkl}\epsilon_{kl}. \quad (3.1)$$

$\sigma_{ij}$  is the Cauchy stress tensor,  $\epsilon_{kl}$  the strain tensor and  $C_{ijkl}$  the 4th order tensor of elastic coefficients. Here  $1 \leq i, j, k, l \leq 3$  are taken according to the axes of a general 3D cartesian coordinate system. The effective stress,  $\tilde{\sigma}_{ij}$ , between the voids in the matrix is expressed as

$$\tilde{\sigma}_{ij} = \frac{\sigma_{ij}}{1 - \omega}. \quad (3.2)$$

I.e. the effective stress between voids is larger than the globally measured stress,  $\sigma_{ij}$ , when  $\omega > 0$ .  $\tilde{\sigma}_{ij}$  is then included in the yield criterion. The increase of the damage variable can be interpreted as a reduction in the load carrying capacity of the material due to void growth. The challenge is to model how  $\omega$  develops during loading since it will depend on both the stress state and stress history. It can be noted that softening due to void growth and hardening due to plastic deformation are two counteracting effects.

#### 3.3.2 Uncoupled Approach

An uncoupled approach does not alter the constitutive equation, meaning that softening is not taken into account. Two examples of such criteria are given below.

##### Johnson-Cook Fracture Criterion

$$\varepsilon_{eq}^f = (D_1 + D_2 e^{-D_3 \sigma^*})(1 + D_4 \ln \dot{\varepsilon}_{eq}^*)(1 + D_5 T^*). \quad (3.3)$$

$\sigma^*$  is the stress triaxiality ratio,  $\dot{\varepsilon}_{eq}^*$  is the dimensionless strain rate defined as  $\frac{\dot{\varepsilon}_{eq}}{\dot{\varepsilon}_{eq}^0}$ , where  $\dot{\varepsilon}_{eq}^0$  is the strain rate during the tensile test and  $\dot{\varepsilon}_{eq}$  the equivalent strain rate in the numerical model.  $T^*$  is the homologous temperature defined as  $\frac{T - T_r}{T_m - T_r}$ , where  $T_r$  is the room temperature,  $T_m$  the melting temperature and  $T$  the temperature in the numerical model.

This is an empirical criterion, where the material parameters  $D_1, D_2, D_3, D_4$  and  $D_5$  are calibrated based on experimental results for different strain rates, stress triaxiality ratios and temperatures. A more simplified version can be found when neglecting the temperature and strain rate dependency:

$$\varepsilon_{eq}^f = (D_1 + D_2 e^{-D_3 \sigma^*}). \quad (3.4)$$

It is now evident that the fracture strain is modeled as a monotonically decreasing function of the stress triaxiality ratio. The model is for example not able to capture any increase of  $\varepsilon_{eq}^f$  at intermediate stress triaxialities, as proposed by [28] (Figure 3.3), nor any effect of the Lode parameter,  $\mu_\sigma$ .

##### Cockcroft-Latham Fracture Criterion

The Cockcroft-Latham criterion is based on the assumption that it is the major principal stress,  $\sigma_1$ , that is the major cause for void growth and it is written as

$$W_{cr} = \int_0^{\varepsilon_{eq}^f} \max(\sigma_1, 0) d\varepsilon_{eq}^p. \quad (3.5)$$

The Cockcroft-Latham parameter,  $W_{cr}$ , is the only material variable and fracture is predicted to occur when the integral of  $\max(\sigma_1, 0)$ , integrated over the equivalent plastic strain,  $\varepsilon_{eq}^p$ , reach this critical value.

The fracture strain when using the Cockcroft-Latham criterion is plotted against stress triaxiality in Figure 3.18 for different values of the Lode parameter,  $\mu_\sigma$ . The locus will change when calibrated against X65 steel, but the behaviour should be approximately the same. Note how the criterion also yield a cut-off for negative stress triaxialities, below this fracture would never occur. The locus also misses the increase in fracture strain for intermediate stress triaxialities (Figure 3.3), but it should be noted that this behaviour is not yet well documented.

The Cockcroft-Latham criterion is able to capture many different effects implicitly. The constitutive equation influence the evolution of the major principal

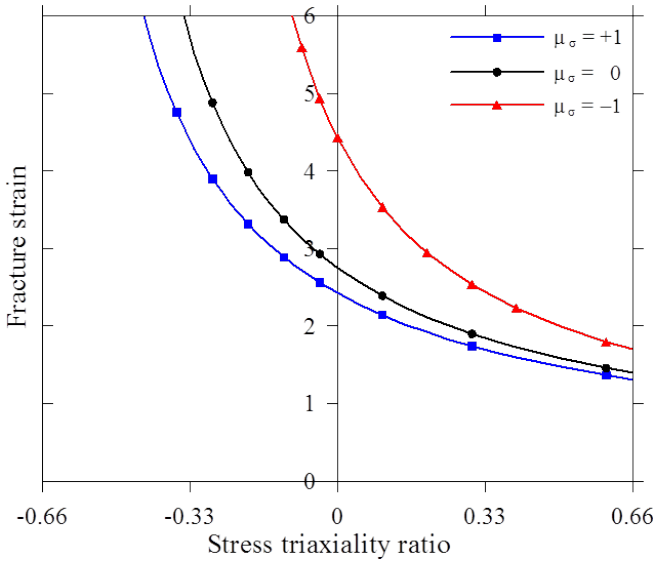


**Figure 3.18:** The fracture locus when using the Cockcroft-Latham criterion on an axisymmetric test specimen made of Weldox 700E steel ( $W_{cr} = 1850MPa$ ) [38].

stress,  $\sigma_1$ , and thus also the fracture strain. The constitutive equation used in this thesis accounts for strain hardening, combined hardening, strain rate and change of yield surface (Hershey surface). A discussion of the how these effects influence the equivalent fracture strain,  $\varepsilon_f$ , is given below.

**Hershey Yield Surface.** By changing the yield surface according to the Hershey-surface (Figure 2.4), the material will undergo plastic deformation earlier compared to the von Mises yield surface in case of shear stresses. This implies that the integral in Equation 3.5 will increase faster for some states of stress compared to when using the von Mises yield surface. The fracture strain will thereby be reduced.

**Isotropic Hardening.** Enlarges the yield surface such that higher stress levels can be reached in case of plastic deformation. This means that higher stress levels will be reached for the same amount of plastic strain compared to ideal plasticity (no enlargement of the yield surface). Thus, the Cockcroft-Latham integral will increase faster and the fracture strain will thereby be reduced. This effect is physically recognized: when a material hardens, for example in case of pre-compressive loading, it will become more brittle and less capable to undergo plastic deformation during subsequent tension. This effect was observed in the material tests carried out on X65 steel. The fracture strain after pre-compression decreased with increasing pre-compression [37].

### 3. Failure

---

**Kinematic Hardening.** Translates the yield surface in case of plastic deformation. When loading is reversed, yielding will occur at a lower state of stress. I.e. in case of compression-tension, the stress in tension, after compression, will be lower for the same amount of strain compared to ideal plasticity. The Cockcroft-Latham integral will only account for the positive values of the major principal stress, meaning that only the phase of tension will contribute to the integral. The fracture strain will thereby be increased (integral will increase slower), compared to a model with ideal plasticity. This effect is not physically recognized and the opposite effect is experienced in the lab. Pre-compression is observed to reduce the fracture strain in subsequent tension (Figure 3.16 and 3.17).

**Viscoplasticity** If the x65 pipe steel is strained at high strain rates, higher stress levels will be reached for the same amount of strain compared to quasi-static straining. This implies that the Cockcroft-Latham integral will increase faster such that the fracture strain will be reduced. Slåttedalen and Ørmen [1] found the fracture strain to decrease slightly with increasing strain rate in their experiments.

#### The Material Parameter, $W_{cr}$

The material parameter  $W_{cr}$  is based on a smooth uniaxial tension tests by determining the area of the true stress - true plastic strain curve until failure. This is simply equal the Cockcroft-Latham integral Equation (3.5), since the true stress,  $\sigma_t = F/A$ , is equal to the average major principal stress over the cross-section. Slåttedalen and Ørmen [1] found  $W_{cr}$  to be equal to  $1595 \text{ MPa}$  after quasi-static testing of smooth specimens with the geometry given in Figure 3.19.

Bao and Wierzbicki pointed out in their article [39] that the Cockcroft-Latham criterion, along with many other similar criteria, did not provide consistent results when tested numerically on different cases of loading on specimens made of 2024-T351 aluminum. Uniaxial material tests have been conducted on different uniaxial notched specimens exposed to different amounts of pre-compression by Kristoffersen et. al. [37] and Aune and Hovdelien [3] on X65 steel.

Figure 3.20 and 3.21 illustrate how the positive true stress - true plastic strain integral,  $W_p$ , reduces if the specimen is exposed to pre-compression. A reduction from  $987$  to  $895 \text{ MPa}$  is noted on the specimen with a  $6.4 \text{ mm}$  notch diameter

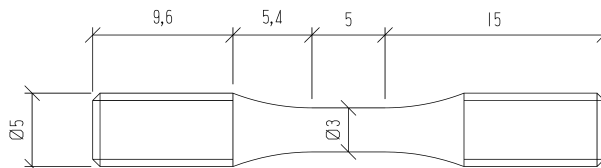


**Figure 3.19:** Smooth specimen used for determining  $W_{cr}$  [1].

when the amount of pre-compressive strain is increased from 0 to 40 %. The specimen with 4.0 mm notch diameter was exposed to pre-compressive strain up to 100 %, and  $W_p$  was reduced from 1212 to 172 MPa. The results for 90% and 100% pre-compression is however not that relevant since both specimens failed in a shear mode instead of cup-and-cone [37]. However, it does shed some light on how drastically  $W_p$  can be reduced if the failure mode is changed.

It is interesting to compare  $W_p$  in case of 0 % pre-compressive strain between the smooth specimen illustrated in Figure 3.19 and the notched specimen in Figure 3.20. The smooth specimen has an initial triaxiality of 0.33, while the notched specimen has an initial maximum triaxiality in the centre equal to 0.70 <sup>4</sup>.  $W_p$  is noted to reduce from 1595 to 987 MPa. The same trend is observed when comparison is made between the two specimens exposed to 40 % pre-compressive strain. The specimen in Figure 3.21 with an initial triaxiality of 0.58 yielded  $W_p$  equal to 1212 MPa, while the specimen in Figure 3.20 with an initial triaxiality of 0.70 yielded 895 MPa. Two trends are thus observed to occur. The true stress - true plastic strain integral,  $W_p$ , which the material parameter  $W_{cr}$  is based on, is observed to reduce with both increasing stress triaxiality and pre-compressive strain.

This observation is probably the best explanation to why the criterion fails when applied to numerical models exposed to varying stress-strain histories.

---

<sup>4</sup>Calculated according the formula proposed by Bridgman[40]:  $\sigma_{max}^* = \frac{1}{3} + \ln(1 + \frac{a}{2R})$ . Here a is the radius at midspan of the specimen and R the radius of the notch.

### 3. Failure

---

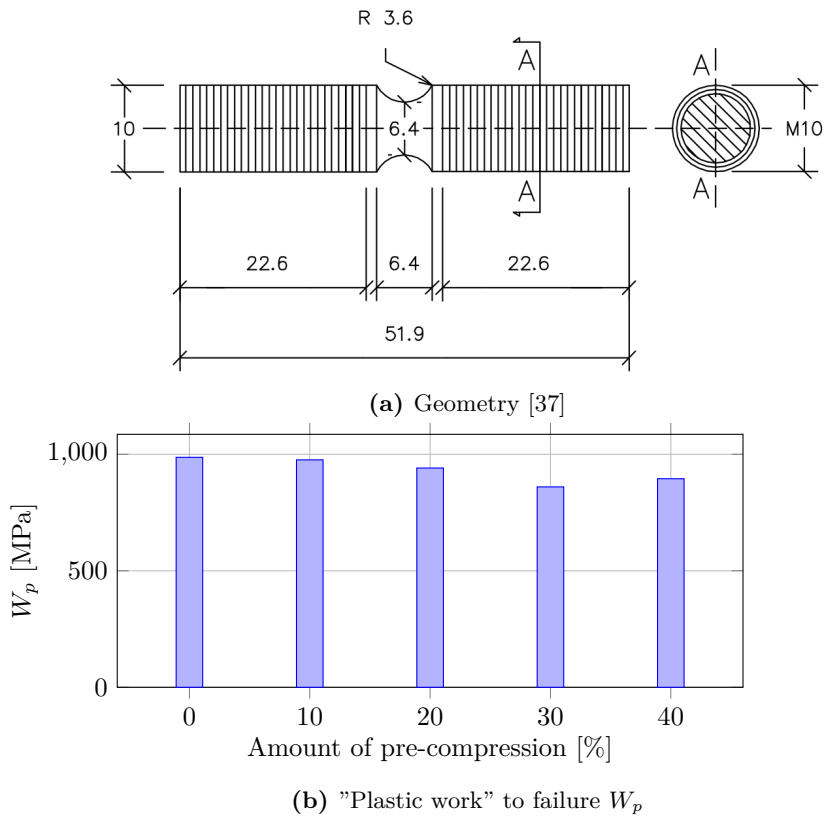


**Figure 3.20:** Compression-tension tests exposed to pre-compressive strain up to 40% [37]

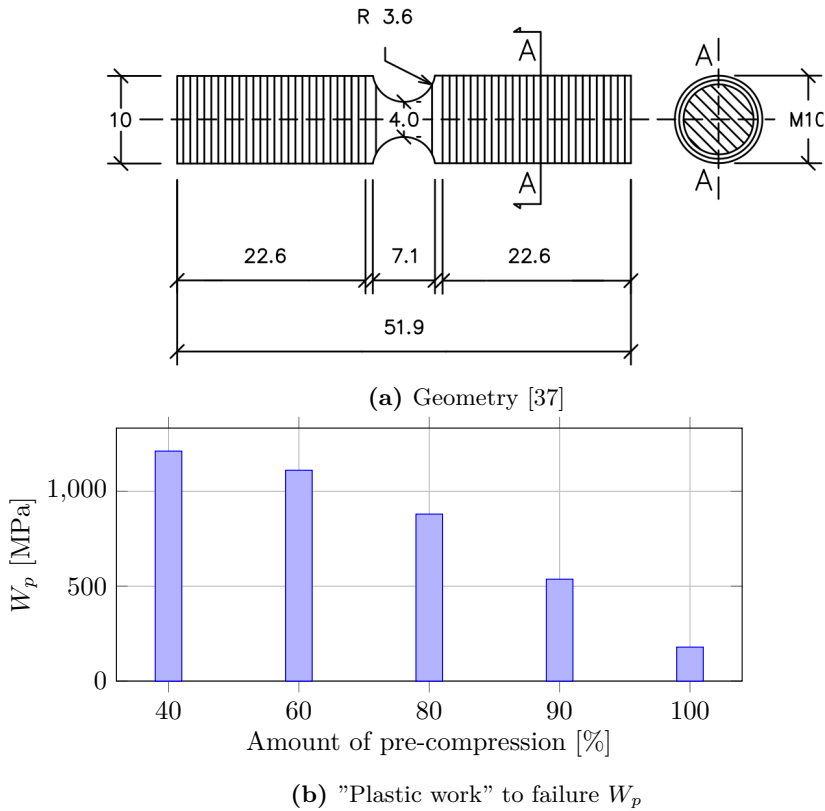


**Figure 3.21:** Compression-tension tests exposed to pre-compressive strain from 40 to 100% [37]





## Chapter 4

# Experimental Work

Two sets of tests have been conducted as part of this thesis. Quasi-static bending of empty pipes and quasi-static bending of simply supported empty pipes with horizontal axial loading and internal pressure in a three point stretch-bending rig. Quasi-static bending of empty pipes were conducted as a comparison to the dynamic tests discussed by Aune and Hovdelien [3]. I.e. pipes with the same dimensions, restricted by the same boundary conditions were loaded to approximately the same indenter deformation as the dynamic impact tests. This was done to investigate the importance of dynamic loading with regard to crack formation. Quasi-static bending of empty pipes with axial loading and internal pressure were conducted as a comparison to the tests discussed by Jakobsen [5] (same boundary conditions only without internal pressure). This was done to investigate how internal pressure affects the global force response of the pipe and the deformation locally in the vicinity of the dent.

### 4.1 Quasi-Static Bending of Simply Supported Empty Pipes

Two quasi-static tests similar to the dynamic experiments, pipe K and L, were conducted. Metallurgical investigation of the pipes after dynamic impact (pipe K and L) revealed both internal and external cracks of different scales (Section 3.2.2). It is of great interest to investigate if the formation of such cracks are dependent on dynamic loading or not. Quasi-static testing is a much simpler form of testing compared to the dynamic tests conducted in the kicking machine [8] situated at SIMLab, NTNU. Thus it is of practical interest to determine if quasi-static testing is sufficient or not.

#### 4.1.1 Previous Findings

Slåttedalen and Ørmen [1] was the first to discuss experimental testing on simply supported empty X65 steel pipes. Four pipes were tested: A, B, C and D. All pipes were first subjected to dynamic impact in the kicking machine and then quasi-statically stretched in a 1200 *kN* Instron test machine to simulate the whole load cycle of trawl gear impact. Pipe A and B were exposed to impact velocities equal to 3.24 *m/s* and 5.12 *m/s*, respectively. Experiment C (3.06 *m/s*) was done as a verification of experiment A, and pipe D was impacted with a slightly lower velocity (2.72 *m/s*). All of the pipes displayed fracture of different scale visible to the naked eye after stretching.

Aune and Hovdelien [3] repeated the experiments two years later, by conducting two new experiments without the stretching step to investigate if cracks developed already after impact (pipe K and L). Pipe K was subjected to an impact velocity equal to 5.18 *m/s* and pipe L was impacted at 3.26 *m/s*. Metallurgical investigation afterwards revealed external and internal cracks through 75% of the wall thickness of pipe K. Smaller external and internal cracks of approximately 20-300  $\mu\text{m}$  was found in pipe L (Section 3.2.2). A brief summery of experiment A, B, D, K and L is presented in Table 4.1.

**Table 4.1:** Summary of relevant dynamic tests.

Pipe	A	B	D	K	L
Load cycle <sup>a</sup>	IS	IS	IS	I	I
Impact velocity [ $m/s$ ]	3.24	5.13	2.71	5.18	3.26
Trolley mass [ $kg$ ]	1472	1472	1472	1472	1472
Kinetic energy <sup>b</sup> [ $kJ$ ]	7.71	19.36	5.44	19.75	7.82
Inner deformation <sup>c</sup> [ $mm$ ]	170	333	105	403	133
<b>6 (N-S)</b> <sup>c</sup> [ $mm$ ]	60	22.5	85.7	27.02	73.40

<sup>a</sup>IS - Impact and Stretching, I - Impact only.

<sup>b</sup>Kinetic energy of the trolley at impact.

<sup>c</sup>According to the measurement scheme in Figure 4.6.

### 4.1.2 Experimental Setup

Two pipes, termed M and N, were to be bended quasi-statically with boundary conditions equivalent to the dynamic experiments. I.e. simply supported, support width equal to  $1000\text{ mm}$ , an indenter with nose tip radius equal to  $10\text{ mm}$  which moved vertically and loaded the pipe at midspan (Figure 4.1 and 4.2). The experiment was carried out in an Instron 1332,  $250\text{ kN}$ , test machine with an indenter velocity equal to  $10\text{ mm}/\text{min}$ . To compare crack development between quasi-static and dynamic loading it was needed to apply a certain indenter deformation which resulted in approximately the same permanent inner deformation as pipe K and L (Table 4.1). However, this parameter is only measurable after testing, hence the indenter displacement was estimated based on previous work. This was not straightforward and measurement afterwards revealed that the estimates were a bit wrong (discussed later in Section 4.1.4). The supports were positioned at the edge of the unlathed area at both ends (Figure 4.2).

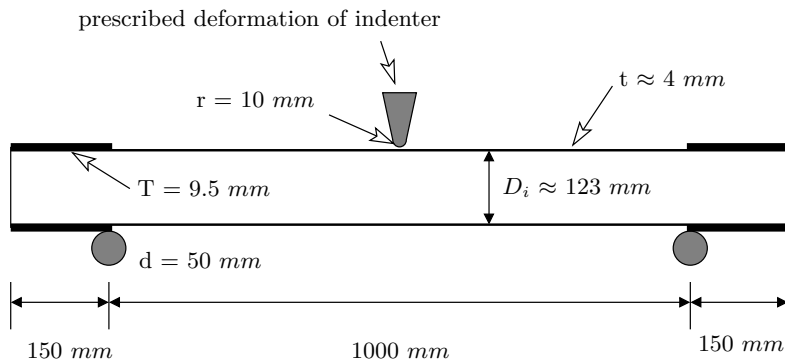


**Figure 4.1:** Simply supported pipe, zero horizontal loading and a support width equal to  $1000\text{ mm}$ .

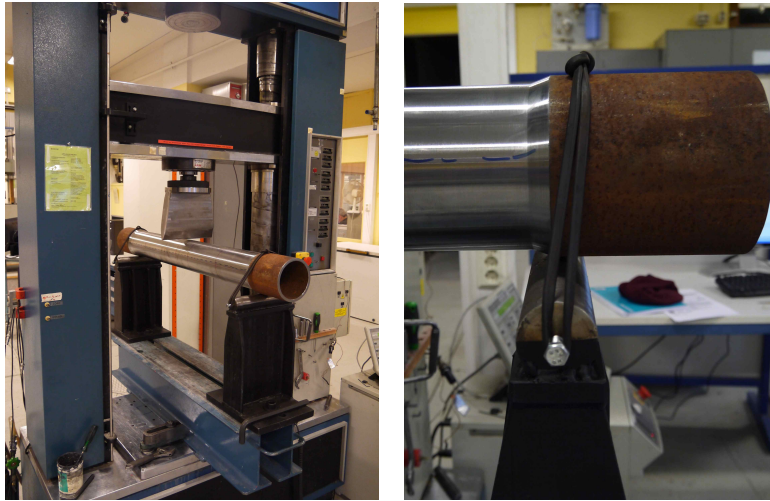


**Figure 4.2:** Setup for component test M and N.

### Digital Image Correlation (DIC)

Both experiments were set up for measurements with DIC. DIC is an algorithm that tracks the translation of a specific point on the surface of a specimen in a series of images. By doing this, translations and strains on the surface of the pipe can be obtained in a three dimensional representation. The surface of both pipes were painted in a chess pattern to get a distinct pattern, which made it easier for the software to correlate each picture such that translations could be obtained. Two cameras were set up to get a 3D representation of the surface and to continuously take pictures during deformation. However it was not easy to position the cameras such that decent pictures could be taken of the whole surface, because the configuration of the test machine obstructed direct positioning of the cameras in front of the pipe. Since the pipe underwent a rather large displacement during deformation it was needed to place the cameras quite far from the the pipe (Figure 4.3).

### 4.1.3 Pipe Measurement

A high sensitivity of the resulting force to the wall thickness has been pointed out in the previous theses. The wall thickness was therefore measured at 40 different locations (Appendix A.1), a summary is presented in Table 4.2 along with the dimensions of pipe A, K and L which is included for comparison with regard to the following discussion.

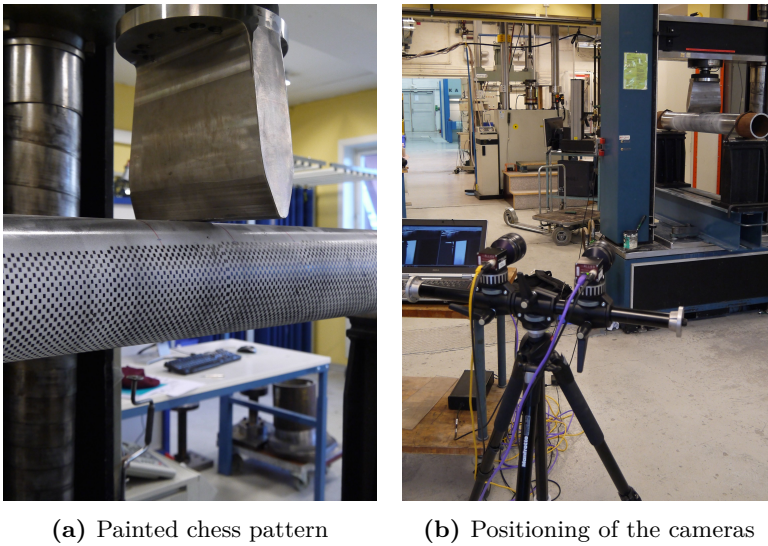


**Figure 4.3:** Setup for component test M and N.

**Table 4.2:** Pipe dimensions prior to testing, according to Figure 4.4.

Pipe	A	K	L	M	N
<b>Wall thickness</b>					
<b>AVG</b> [mm]	3.89	4.12	4.17	3.74	3.90
<b>SDEV(REL)</b> <sup>a</sup>	9.23%	6.30%	8.45%	6.68%	6.67%
<b>Inner diameter</b>					
<b>AVG</b> [mm]	122.56	122.46	122.47	122.62	122.33
<b>SDEV(REL)</b> <sup>a</sup>	0.15%	0.21%	0.17%	0.31%	0.16%
<b>Length</b>					
<b>Inner length</b> [mm]	975	975	975	975	975

<sup>a</sup>SDEV divided by AVG

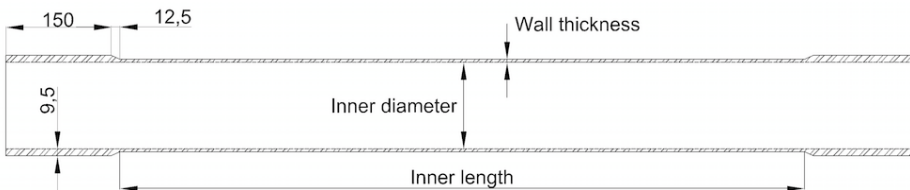


**Figure 4.4:** Measured dimensions.

## 4. Experimental Work

---

### 4.1.4 Results

Four parameters may be pointed out that distinguish between quasi-static and dynamic experiments:

- Impact energy. Different trolley velocities will result in different impact energies.
- Rate of deformation. Different indenter velocities will result in different deformation rates.
- Wall thickness. The wall thickness will affect the pipe stiffness. It might also affect the state of stress and thus the likelihood for fracture .
- Impact off safety buffers. The indenter trolley hits a set of safety buffers at the end of deformation during the dynamic experiment in case of impact velocities approximately larger than  $5\text{ m/s}$ .

**Deformation.** Close up pictures of the dented zone of pipe M and N are given in Figure 4.5. Both pipes were measured according to the procedure followed in the previous theses (Figure 4.6) and results are presented in Table 4.3. The applied indenter displacement resulted in an inner displacement which was  $23\text{ mm}$  less for pipe M (compared to pipe K) and  $28\text{ mm}$  larger for pipe N (compared to pipe L). N-S diameter at midspan (point 6) gives an indication of the dent depth. Even though pipe M was  $23\text{ mm}$  off on inner deformation (compared to K), it was only  $1.0\text{ mm}$  off when it comes to the N-S diameter at point 6. Pipe N was  $28\text{ mm}$  off on inner deformation (compared to L) and was on the other hand  $9.5\text{ mm}$  off on the N-S diameter at point 6. This mismatch of ratios (N-S diameter at point 6 to inner deformation) probably can be explained by an approximately constant dent depth in last phase of deformation. Such that an inner deformation of  $403\text{ mm}$  (pipe K) almost yields the same N-S diameter at midspan as  $380\text{ mm}$  (pipe M), while it does not yield the same when comparing  $133\text{ mm}$  (pipe L) and  $161\text{ mm}$  (pipe N). This mismatch may also be influenced by wall thickness differences between the pipes.

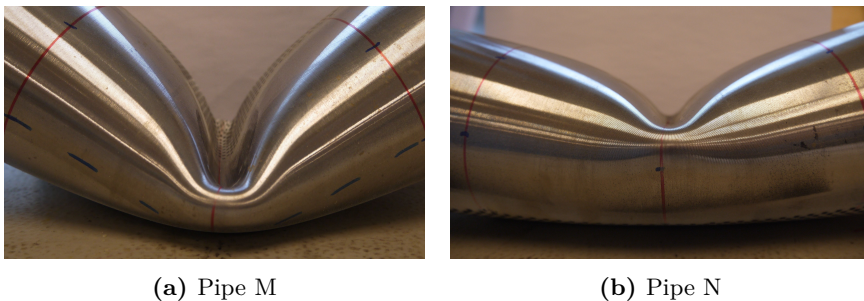


**Figure 4.5:** Comparison of denting between pipe M and N.

**Table 4.3:** Pipe deformation after quasi-static impact.

Pipe	M		N	
Inner deformation [mm]	380		161	
Distance north-north [mm]	1042		1249	
Outer diameter at [mm]	N-S	E-W	N-S	E-W
1	130.83	130.83	131.12	130.90
2	129.65	132.08	130.85	131.41
3	126.83	134.62	128.88	133.16
4	120.13	141.81	123.94	137.31
5	97.32	156.20	113.00	147.69
6 <sup>a</sup>	26.05	201.53	63.91	178.09

<sup>a</sup>Inaccurate measurement in the N-S direction.

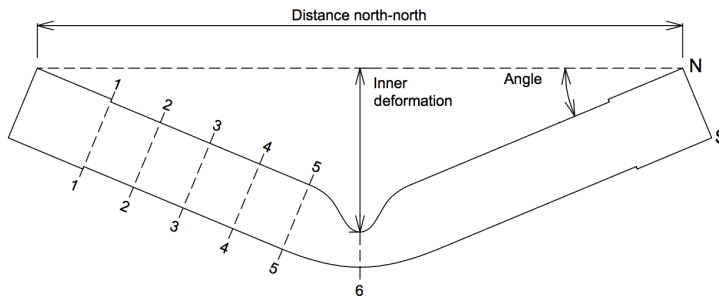


**Figure 4.6:** Points for measurement after deformation [1].

**Table 4.4:** Comparison of relevant measures after deformation.

Pipe	A	K	L	M	N
Inner deformation [mm]	170	403	133	380	161
6 (N-S)[mm]	60	27.02	73.40	26.06	63.91
Ratio <sup>a</sup>	0.35	0.067	0.55	0.07	0.40

<sup>a</sup>Ratio of N-S diameter at point 6 to inner deformation.

### Force-Displacement

**Dimensional Results.** The force-displacement curve is an important parameter when it comes to verification of the numerical model and qualification of the different phases of deformation. It might also tell something about the dynamic forces present in terms of inertial forces when comparing results between dynamic and quasi-static testing. Unfortunately no data was recorded during the dynamic pipe L experiment ( $3.26\text{ m/s}$ ) due to an error in the load cell. The force-displacement curve from the pipe A experiment ( $3.24\text{ m/s}$ ) have therefore been included. The result should basically be the same. A force-displacement comparison between dynamic and quasi-static testing can be seen in Figure 4.7. The dynamic tests have some oscillations due to the indenter impact. It is seen that the oscillations are largest in experiment K, which also had the largest impact velocity. It is seen that all curves have the same curvature which typically can be characterized by three distinct phases [41, 42, 43]:

- Denting. The pipeline dents locally at the top surface where the indenter hits the pipe. The force increases steeply.
- Denting and bending. The denting mode of deformation reduces the bending capacity of the pipe and this leads to a combination of both denting and bending. The maximum transverse pipe load capacity,  $F_{max}$ , occurs during this phase.
- Structural collapse. Occurs after the maximum capacity is reached and is recognized by global bending, as the primary mode of deformation.

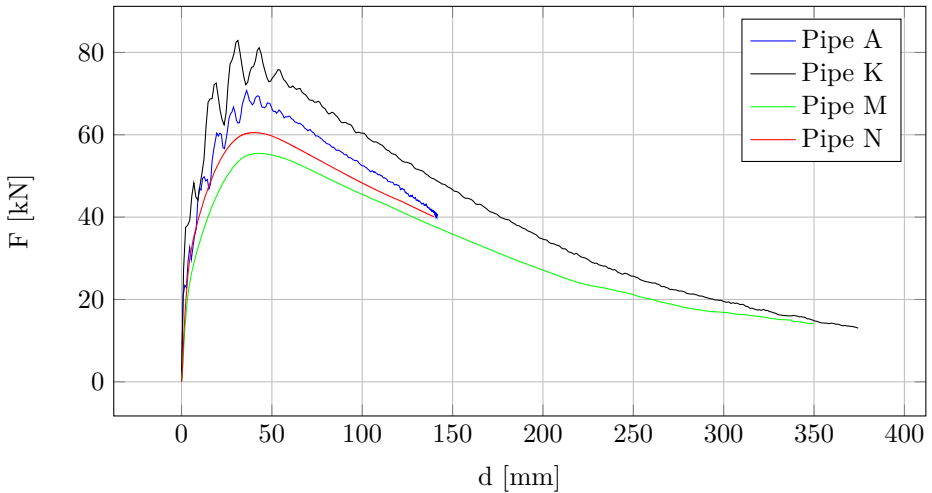


**Figure 4.7:** Force-displacement plot for quasi-static tests (M and N) and dynamic tests (A and K).



**Dimensionless Results.** The average measured thickness of the four pipes varies from 3.74 mm (pipe M) to 4.12 mm (pipe K) and it is pointed out in the previous theses how this parameter largely influences the stiffness. It was therefore questioned if it was possible to make the plot dimensionless in such a way that the variation in wall thickness was accounted for. This implies that the displacement needed to be scaled with a parameter with dimension  $mm$  and force with a parameter with dimension  $kN$ . These parameters can be chosen quite freely, and many options exist. A measure of the quality of the scaling is to compare the two plots of pipe M and N since these pipes were tested with the same boundary conditions: same midspan between supports and same indenter velocity. Thus it is only the thickness and inner diameter which varies between the two pipes, and "good" scaling should make the two plots almost identical.

To make the comparison between dynamic and quasi-static testing easier, the oscillations in the dynamic experiments were first smoothed out using the *csaps*-function in MATLAB. The *csaps*-function is an embedded function in MATLAB which constructs a cubic smoothing spline that more or less follows the presumed underlying trend in noisy data [44]. A user-defined smoothing parameter determines how closely the spline follows the given data.

The transverse indenter displacement (x-axis),  $d$ , was made dimensionless by using the measured inner diameter of each pipe,  $d_{inner}$ . The inner diameter only varied from 122.33 mm (pipe N) to 122.62 mm (pipe M), and therefore only exerts a minor influence

$$d^* = \frac{d}{d_{inner}}. \quad (4.1)$$

Here  $d^*$  is the dimensionless transverse indenter displacement. The dimensional analysis of the pipe impact problem performed by Slåttedalen and Ørmen [1], carrying out the Buckingham  $\pi$  theorem, suggest that the impact force can be scaled as

$$\Pi_{15} = \frac{F}{t^2 \sigma_Y}, \quad (4.2)$$

where  $t$  is the wall thickness and  $\sigma_Y$  is the yield stress. However it is important to point out that this is only a mathematical concept, giving the relation between the different fundamental variables (length, mass, force etc.) in the experiment.

**Bending Stiffness.** It was at first decided to try to scale the force with the indenter force required to reach yield stress in the most exposed point in the cross section due to bending. In case of a simply supported beam with a point load,  $F$ , at midspan, the moment at midspan can be calculated as

$$M_{midspan} = \frac{FL}{4}, \quad (4.3)$$

where  $L$  is the distance between the supports. If the pipe is align according to a cartesian coordinate system, where the x-axis is taken as the axis along the longitudinal direction of the pipe and with the y-axis parallel to the direction of

## 4. Experimental Work

loading. The normal stress in the cross section,  $\sigma_y$ , due to the bending moment,  $M$ , can be calculated as a linear function of  $y$  (not valid in case of plasticity)

$$\sigma_y = \frac{M}{I_z} y. \quad (4.4)$$

Here  $I_z$  is the second moment of area of the cross section with respect to axis of bending, and  $y$  is the distance from the neutral axis. By combining these two expressions and setting  $y = r_o$  and  $\sigma_y = \sigma_Y$ , where  $r_o$  is the outer radius and  $\sigma_Y$  the yield stress, the force required to reach yield the yield limit,  $F_{yield}$ , can be expressed as

$$F_{yield} = \frac{\pi(r_o^4 - r_i^4)\sigma_Y}{Lr_o}, \quad (4.5)$$

where  $r_i$  is the inner radius and  $L$  is the support width, equal to 1000 mm. The dimensionless transverse indenter force is then calculated as

$$F^* = \frac{F}{F_{yield}}. \quad (4.6)$$

The result using  $F_{yield}$  as the scaling parameter is given in Figure 4.8. Compared with the dimensional plot (Figure 4.7), it is seen that bending-stiffness scaling only has a minor effect. Still there is deviation between pipe M and N, which are the two plots assumed to be almost identical if proper scaling is applied.

Based on the work in [41, 42, 43], as described by [1], it is the denting phase which causes the largest increase in loading. It is also pointed out that bending occurs after the formation of a local surface dent, where bending is caused by the reduced second moment of area,  $I_z$  of the cross section, due to denting.

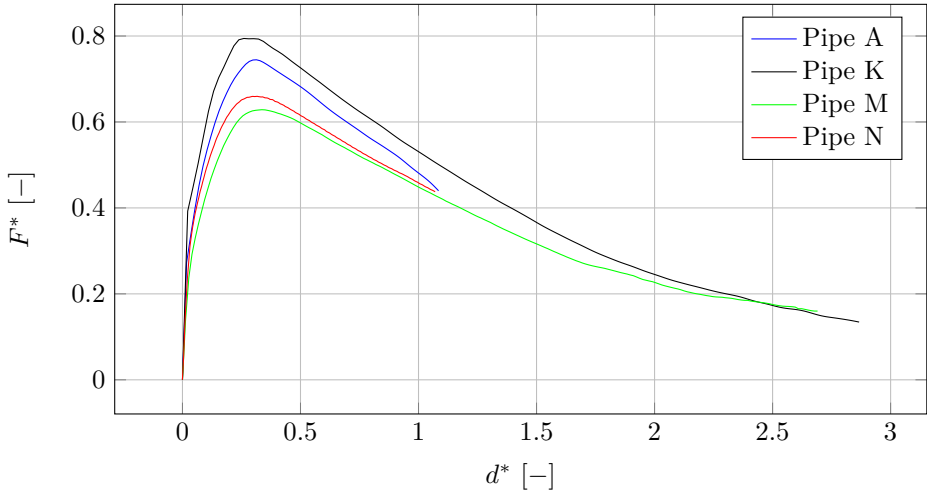


**Figure 4.8:** Dimensionless force-displacement plot for quasi-static tests (M and N) and dynamic tests (A and K) scaled with the bending stiffness.

This might explain why the proposed scaling does not work. It only account for the initial bending stiffness of the pipe, while bending in reality occurs after the denting phase. It was therefore of interest to try another scaling parameter which accounted for the increased denting stiffness due to increased wall thickness.

**Denting Stiffness.** Sørreide [45] proposed a way to calculate the work needed to create a pipe dent, by modeling it as a geometrical configuration of a plastic hinge. If ideal plasticity is assumed, the required moment to bend the pipe wall cross-section is constant, given that deformation across the entire cross section occurs plastically. The so-called plastic moment is thus only dependent on the geometry (wall thickness) and the yield stress. The plastic moment capacity of the pipe wall per unit length can be calculated as

$$m_p = \frac{\sigma_Y t^2}{4}, \quad (4.7)$$

where  $t$  is the wall thickness and  $\sigma_Y$  the yield stress. The work per unit length can correspondingly be calculated as

$$w = m_p \Gamma, \quad (4.8)$$

where  $\Gamma$  is the bended angle of the cross-section. If the dent is geometrically modeled according to Figure 4.9, the total work can be calculated by first decomposing it into two regions such that the total work is given as

$$W = W_r + W_t, \quad (4.9)$$

where  $W_r$  is the work needed to move the rectangle at midspan ( $B \times h$ ) and  $W_t$  is the work needed to move the two triangles (Figure 4.9).  $W_r$  can be found as

$$W_r = \frac{\sigma_y B t^2}{2} \left( \frac{\pi}{2} - \arcsin\left(1 - \frac{\Delta}{r}\right) \right), \quad (4.10)$$

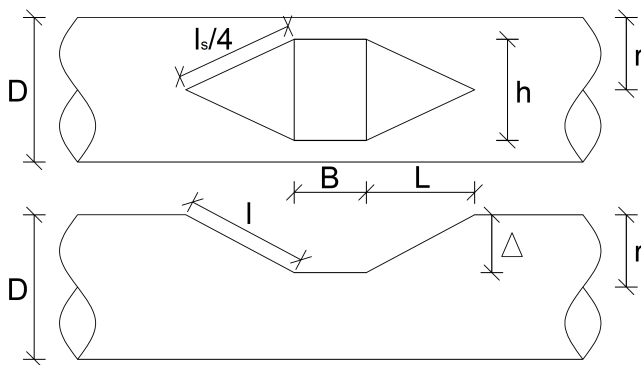


**Figure 4.9:** Geometrical model of the local dent [45].

#### 4. Experimental Work

---

where  $\Delta$  is the dent depth. The work needed to move the two triangles,  $W_t$ , can be found as

$$W_t = \sigma_Y t^2 \Delta \sqrt{2 \frac{r}{\Delta} + \left(\frac{L}{\Delta}\right)^2} \left[ \frac{1}{2} \arctan \left( \frac{\sqrt{\left(1 + 2\frac{r\Delta}{L^2}\right) \left(\frac{\Delta}{r} \left(2 - \frac{\Delta}{r}\right)\right)}}{\left(1 + 2\frac{r\Delta}{L^2} - \left(\frac{\Delta}{L}\right)^2\right) \left(1 - \frac{\Delta}{r}\right)} \right) + \arctan \left( \left(\frac{\Delta}{L}\right)^2 \frac{\sqrt{2\frac{r}{\Delta} - 1}}{\sqrt{1 + 2\frac{r\Delta}{L^2}}} \right) \right]. \quad (4.11)$$

Here  $r$  is taken as the average of the inner and outer radius of the pipe. By choosing a specific dent configuration, defined through  $B$ ,  $L$  and  $\Delta$ . And given the specific wall thickness,  $t$ , radius,  $r$ , and yield stress,  $\sigma_Y$ , the plastic work needed to move such a dent to the specified configuration can be calculated. The average force,  $F_{avg}^{denting}$ , needed to do this work can then be calculated as

$$F_{avg}^{denting} = \frac{W}{\Delta}. \quad (4.12)$$

$F_{avg}^{denting}$  is then used to scale the measured indenter force,  $F$

$$F^* = \frac{F}{F_{avg}^{denting}}. \quad (4.13)$$

$B$  was chosen as the indenter width (twice its radius) equal to 20 mm,  $\Delta$  and  $L$  were set equal to 10 mm and 100 mm. However this choice is not critical for the result as long as  $\frac{\Delta}{L} < 0.15$ . When  $r$  was set as the average of  $r_o$  and  $r_i$ , and  $\sigma_Y$  as 472 MPa the result plotted in Figure 4.10 was obtained.

This choice of scaling seems to give good results. The curves of pipe M and N are almost identical as wanted.

Figure 4.10 clearly illustrates the difference between doing quasi-static and dynamic testing, it is seen that the force initially is higher in the dynamic experiments compared to the quasi-static. This increase is probably caused by viscoplastic and inertial effects.

Dynamic tensile tests on X65 steel, discussed by [1], at elevated strain rates (240-830 1/s) displayed a clear viscoplastic behaviour. The yield stress increased with approximately 19% when the strain rate was increased from quasi-static ( $10^{-3} s^{-1}$ ) to ( $830 s^{-1}$ ). However the local strain rates in the pipe during deformation will vary from being presumably large locally in the dent to being smaller away from the dent, which makes it hard to quantify the influence of this effect.

When the indenter hits the pipe the pipe wall will be accelerated and this will contribute to the recorded transverse force ( $F = ma$ ). This additional "inertial stiffness" vanish when the pipe wall/mass acceleration equals zero. However a

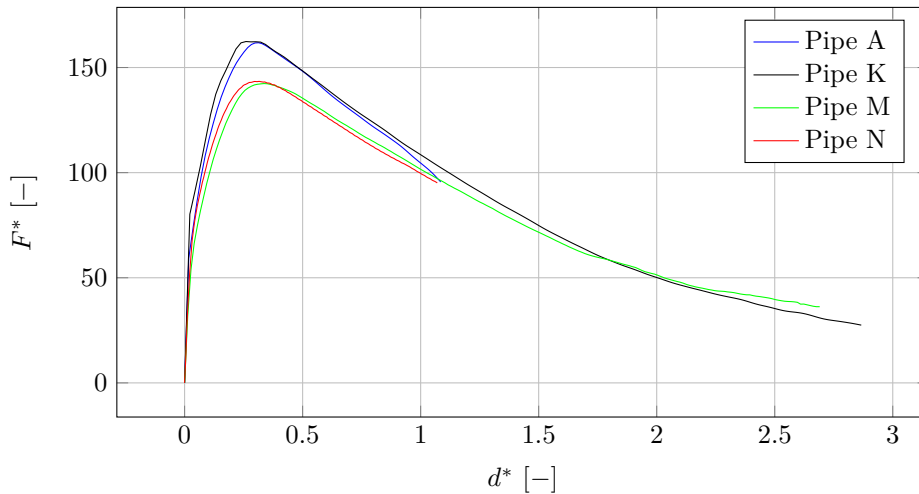


**Figure 4.10:** Dimensionless force-displacement plot for quasi-static tests (M and N) and dynamic tests (A and K) scaled with the denting stiffness.

clear mark of when the "inertial stiffness" vanish does not exist since two modes of deformation are present (denting and bending). I.e. the amount of wall/mass acceleration will vary along the pipe when impacted. Initially only the mass in the vicinity of the dent will be accelerated (denting phase), followed by the bending phase where moreover the "whole" pipe is accelerated. The phase of acceleration will be followed by a phase of deceleration as the deformation is stopped, as the kinetic energy of the trolley and the pipe itself is transferred to either elastic stored energy or dissipated as heat through plastic deformation. This deceleration of the pipe wall/mass will lead to a negative force contribution ( $F = ma$ ) compared to quasi-static testing. This effect might explain why the dynamic plots initially displays a higher force, then approach the quasi-static and finally at the end goes below the quasi-static (only visible on the pipe K vs pipe M plot).

### 4.1.5 Metallurgical Investigation

The main purpose of the experiments was to investigate if any cracks developed after quasi-static loading to determine if the formation of such cracks is dependent on dynamic loading. Pieces of the deformed pipes were cut out and examined using optical microscopy. A comparison of the cross sections of pipe M and N is presented in Figure 4.11.

#### Pipe M

That a difference existed was determined already after visual inspection: no fractures were visible on the surface of the most heavily deformed pipe M, contrary to what was found on the surface of the dynamically impacted pipe K (Figure 4.12). The surface of pipe M also seem more rough (clearly visible lathing

#### 4. Experimental Work

---

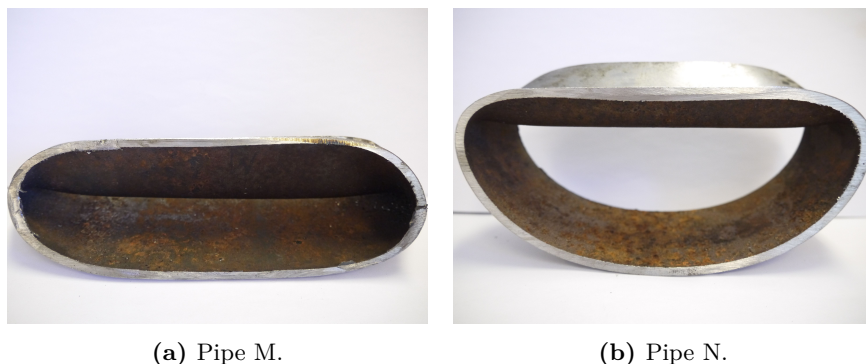


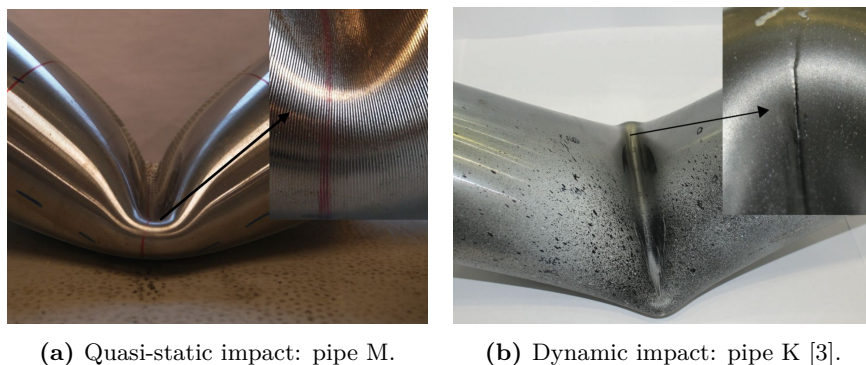
**Figure 4.11:** Comparison of the cross sections after quasi-static loading.

grooves) compared to the surface of pipe K, which seems more polished. An effect which should have favored crack formation on pipe M due to possible stress concentrations caused by the lathing grooves.

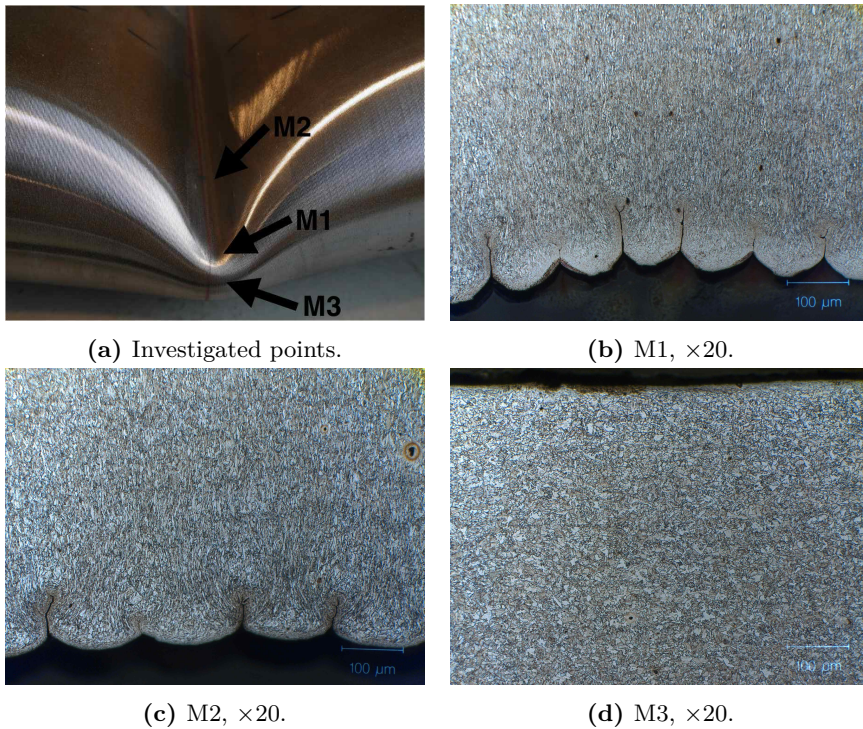
Pieces of the most dented zone were cut out to do a closer investigation of the wall cross-section to see if any smaller cracks had developed. The only cracks found were some small surface cracks related to the lathing grooves (Figure 4.13). No internal cracks were found (Figure 4.14).

Figure 4.13 illustrates the difference on the outside surface of the respective points M1, M2 and M3. Cracks have developed at the bottom in the lathing grooves, this is most likely due to a local geometric stress concentration caused by the grooves. The largest cracks are found at point M1, while no cracks are found at point M3, where the lathing grooves also are seen to be completely stretched out, indicating that M1 is the most critical region.

The cracks are believed to develop in the spring back phase when the indenter is



**Figure 4.12:** Comparison of the surfaces in the dent after quasi-static and dynamic impact with the approximately same inner deformation.



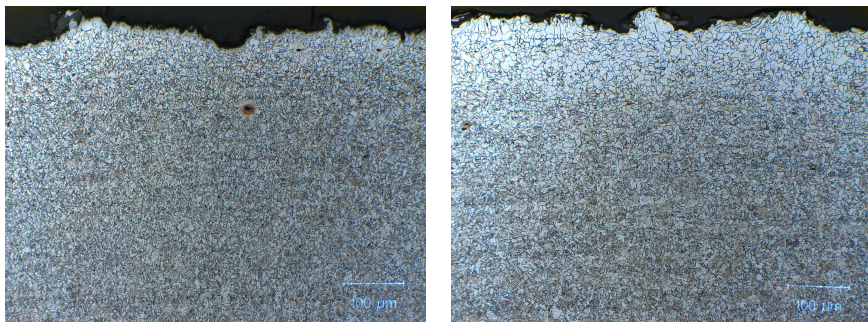
**Figure 4.13:** Microscopy pictures of the outside surface at points M1, M2 and M3.

removed, where the dent to a small degree is stretched due to the stored elastic forces in the pipe. This changes the state of stress from compression to tension at point M1 and M2, such that cracks can develop in a tensile mode. Point M3 is on the other hand exposed to tension during impact, illustrated by the stretched out lathing grooves.

The small black dots seen in Figure 4.13 are the calcium aluminate particles previously described (Section 3.2.3), impurities believed to cause internal stress concentrations which cause the internal cracks found in the dynamic tests [3]. It is important to point out that the lathing grooves are a specific feature of this experiment, and this is not found on real pipelines produced by the Mannesmann process [4]. The experimental pipes are lathed down to obtain the right thickness to diameter ratio for the experiment (experimental pipe dimension is not the same as the real pipe dimension). However similar stress concentrations might be found on the surface of real pipelines due to corrosion.

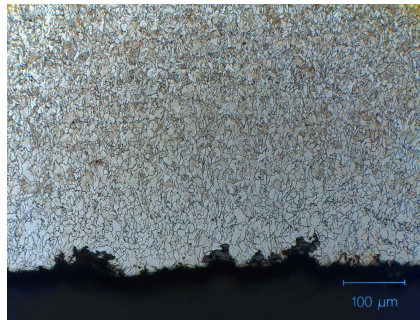
Figure 4.14 illustrates the inside of the wall at the same points M1, M2 and M3, where no cracks of any kind were found.





(a) M1,  $\times 20$ .

(b) M2,  $\times 20$ .



(c) M3,  $\times 20$ .

**Figure 4.14:** Microscopy pictures of the inside surface at points M1, M2 and M3.



### Pipe N

Figure 4.15 illustrates microscopy pictures from the outside surface of the less deformed pipe N after impact. No cracks were found.

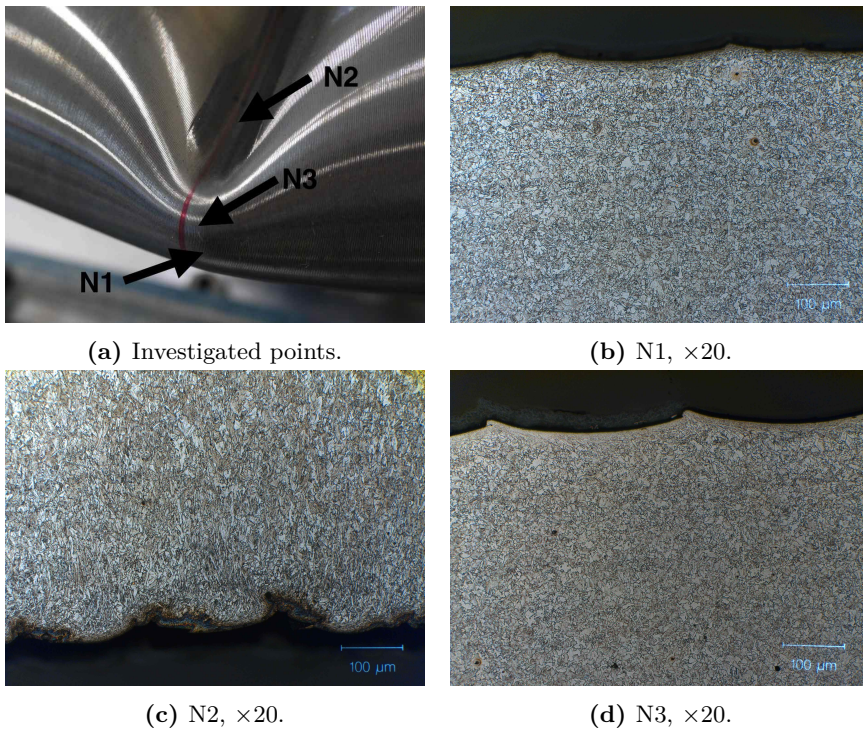


**Figure 4.15:** Microscopy pictures of the outside surface at points N1, N2 and N3.

### 4.2 Quasi-Static Bending of Pressurized Pipes With Horizontal Axial Loading

Three quasi-static tests similar to the tests discussed by Jakobsen [5], but with internal pressure equal to 100 *bar* were conducted as part of this thesis. The tested scenarios are as follows<sup>1</sup>:

**Pipe 8** Internal pressure equal to 100 *bar* and indenter displacement equal to 200 *mm*

**Pipe 9** Internal pressure equal to 100 *bar*, constant horizontal axial loading equal to 50 *kN* and indenter displacement equal to 200 *mm*.

**Pipe 10** Internal pressure equal to 100 *bar*, linearly increasing horizontal axial loading from 0 to 50 *kN* and indenter displacement equal to 200 *mm*.

The horizontal loading is intended to simulate the axial forces which build up as the pipeline is dragged out of its initial position. The amount of 50 *kN* is based on numerical calculations on a 100 *m* long, simply supported beam, which is displaced at midspan. The axial forces will influence how the pipe deforms in the vicinity of the dent, and thus also the probability for fracture. It will also influence the stiffness of the pipe with regard to transverse loading.

As with axial forces, internal pressure will also change the mode of deformation, according to the preliminary numerical study conducted by Asheim and Mogstad [4] and the findings reported by Jonas and Birch [46]. [46] reported that internal pressure decreases the amount of local denting and increase the stiffness of the pipe with regard to transverse loading. This finding is in accordance with the preliminary study conducted [4].

#### 4.2.1 Experimental Setup

Due to application of horizontal axial loading the tests have been carried out in the three point stretch-bending rig situated at SIMLab, NTNU (Figure 4.16). The rig consists of three actuators: two horizontal and one vertical. The vertical actuator is mounted on the floor and it is used to drive the indenter, while the horizontal is connected to a steel frame through a cantilevered structure. All actuators have a load capacity of 330 *kN*. Displacements are independently measured for all three actuators [9].

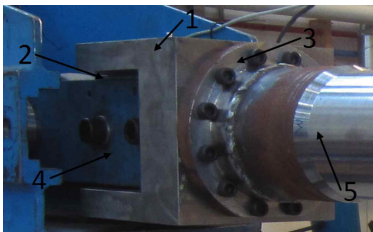
The pipes were mounted to the horizontal actuators through a hinged connection leaving the pipes free to rotate in the plane, i.e. simply supported (Figure 4.17 and 4.18). The pipes were cut 50 *mm* shorter than the pipes used for dynamic tests to fit the rig. Flanges with machined out bolt holes were welded onto the

---

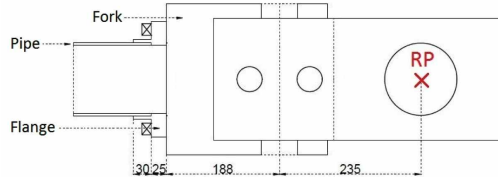
<sup>1</sup>An additional pipe test, termed pipe 7, was executed to test the experimental setup.



**Figure 4.16:** The stretch-bending rig [4].



(a) Flange (1), block bearing - not visible (2), flange (3), grip (4) and pipe (5) [5].



(b) Sketch of distance between pipe weld and rotation point when mounted in the stretch bending rig [4].

**Figure 4.17:** The connecting link between the pipe and the stretch-bending rig.

pipes at the ends such that the pipes could be fastened to the connecting link (Figure 4.17). The flanges resulted in an additional length of 20 mm on each side in accordance with the machine drawing presented in Appendix A.2. Adding the length of the connecting link, 423 mm (188+235 mm), the total length between each rotation point is 2136 mm, which is 1136 mm longer than the previously discussed tests. The same indenter was used as in the previous experiments, i.e. nose tip radius equal to 10 mm. The indenter velocity was set to 25 mm/min and the indenter displacement to 200 mm, equal to pipe experiments 4, 5 and 6.

The unloading is performed as a two step process: first the indenter is removed while the horizontal actuators are fixed, secondly when the indenter is completely removed, the actuators are released such that the pipe can unload completely.

The pipes were pressurized with water, which is incompressible and thus very

## 4. Experimental Work

---

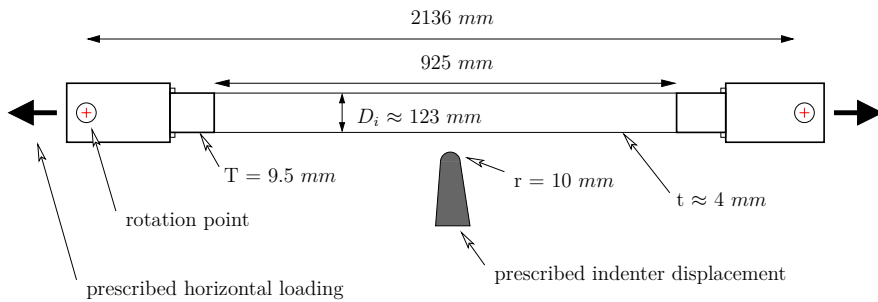


**Figure 4.18:** Sketch of the fundamental setup for quasi-static experiments with varying horizontal loading.

suitable with regard to safety. The pressurizing system mainly consists of a compressor (Figure 4.19), which delivers a pressure of 100 *bar* and a bleeding valve (Figure 4.20), bleeding water as soon as the pressure goes above 100 *bar* during deformation. The compressor was set to deliver water as soon as the pressure went below 100 *bar* as a safety in case the valve bled to much water. A pressure gauge was mounted on the water flow line between the compressor and the pipe such that the pressure could be measured continuously during the experiment (Figure 4.20).



**Figure 4.19:** Hydratron compressor, max capacity of 738 *bar*.

### Digital Image Correlation

It was decided to try to utilize DIC-measurement in the same way which previously has been done in the quasi-static tests in the stretch-bending rig [4, 5]. The surface of the pipe was painted in a dot pattern to get a distinct pattern which could be traced afterwards to obtain translations and strains on the sur-

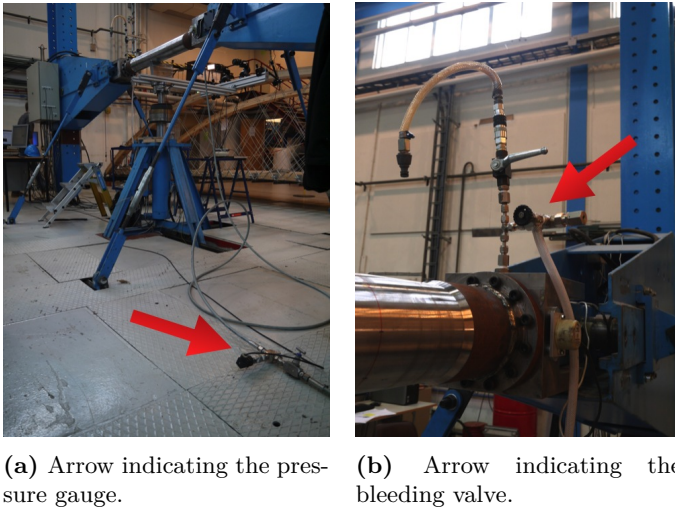


**Figure 4.20:** Key components of the pressurizing system.

face. The cameras were fastened on an aluminum frame that was connected to the vertical actuator such that the cameras could follow the indenter during deformation. Additionally, two headlights were set up on the frame to lighten up the surface and hopefully avoid light sensitivity problems when correlating the pictures (Figure 4.21).

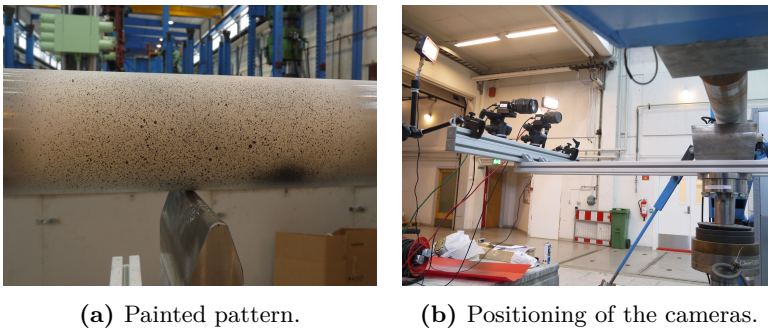


**Figure 4.21:** Setup for pipe experiment 8, 9 and 10.

### 4.2.2 Pipe Measurement

All pipes were measured according to the same scheme as pipe M and N, i.e. the wall thickness was measured at 40 different locations using a PosiTector UTG (Ultrasonic Thickness Gauge), and the inner diameter was measured in four directions on each side using a micrometer. A summary of the data is presented in Table 4.6. For more details it is referred to Appendix A.1.

## 4. Experimental Work

---

**Table 4.5:** Pipe dimensions prior to testing, according to Figure 4.4.

Pipe	8	9	10
<b>Wall thickness</b>			
AVG [ <i>mm</i> ]	4.08	3.95	4.13
SDEV(REL) <sup>a</sup>	5.88%	5.32%	4.35%
<b>Inner diameter</b>			
AVG [ <i>mm</i> ]	122.72	122.48	122.36
SDEV(REL)	0.20%	0.16%	0.23%
<b>Length</b>			
Inner length [ <i>mm</i> ]	925	925	925

<sup>a</sup>SDEV divided on AVG

### 4.2.3 Previous Findings

Asheim and Mogstad [4] discussed pipes exposed to both bending and subsequent stretching (pipe 1, 2 and 3), while Jakobsen [5] omit the stretch step (pipes 4, 5 and 6). Both look at three experiments with zero-, constant- and linearly increasing horizontal loading, similar to what will be discussed in this thesis. However a varying indenter displacement were applied in the pipe experiments 1, 2 and 3 (198.6-282.6 *mm*). It is therefore most relevant to compare results with pipes 4, 5 and 6 (discussed in [5]).

None of the previous quasi-static experiments displayed any signs of fracture by visual inspection after quasi-static bending. However surface cracks were visible on all pipes after subsequent stretching. Metallurgical investigation of the bended-stretched pipes (pipe 1,2 and 3) revealed surface cracks that initiated in the lathing grooves of varying size (120-480  $\mu m$ ) after stretching [4]. The pipes were not subjected to the same indenter displacement, and it is thus not straight forward to point out how horizontal loading affect the probability for fracture.

Metallurgical investigation of pipes 4, 5 and 6 (only bending) were not conducted, and the pipes were not measured after deformation. These pipes have now been measured and the results are given in Table 4.7. The measurements indicate a slight increase in N-S diameter at midspan (i.e. reduction in local denting) in case of horizontal loading. However, the difference is only 5.5 *mm*, and due to difficulties with regard to diameter measurement at midspan this difference is almost negligible. Especially when differences in wall thickness (Table 4.6) also are taken into account.

Figure 4.22 illustrate close up pictures of the respective dents of pipe 4, 5 and 6 (in addition to pipe 8, 9 and 10). When comparing the dents from zero- and constant horizontal loading it can be seen, by close inspection, that the application of horizontal loading to a slight degree reduces local denting in terms of the curvature on the pipe wall, away from the dent. The largest strains are however

**Table 4.6:** Pipe dimensions according to Figure 4.4 [5].

Pipe	4	5	6
<b>Wall thickness</b>			
AVG [mm]	4.20	4.16	4.06
SDEV(REL) <sup>a</sup>	4.56%	6.09%	5.55%
<b>Inner diameter</b>			
AVG [mm]	- <sup>b</sup>	122.41	122.20
SDEV(REL)	- <sup>b</sup>	0.10%	0.19%
<b>Length</b>			
Total length [mm]	1250	1250	1250
Inner length [mm]	925	925	925

<sup>a</sup>SDEV divided on AVG<sup>b</sup>Not measured**Table 4.7:** Pipe deformation after quasi-static impact. Measurements are according to Figure 4.6.

Pipe	4		5		6	
Inner def [mm]	120		120		122	
Distance N-N [mm]	1200		1197		1198	
Outer dia at [mm]	N-S	E-W	N-S	E-W	N-S	E-W
1 <sup>a</sup>						
2	131.00	130.98	130.88	130.90	130.84	130.74
3	130.12	131.82	130.14	131.87	130.23	131.63
4	127.64	134.19	127.87	134.29	127.59	134.07
5	119.50	140.54	118.74	140.92	119.28	140.13
6	83.70 <sup>b</sup>	164.34	89.13 <sup>b</sup>	164.60	86.55 <sup>b</sup>	164.41

<sup>a</sup>In the unlathed area due to shorter inner length. This measurement point was therefore omitted.<sup>b</sup>Inaccurate measurements in the N-S direction.

not present in this region, but instead located in the middle of the dent along the symmetry line at midspan. Based on these observations, it can be assumed that the application of horizontal loading only has a minor influence on the dent geometry and thus also on the likelihood for fracture. However it should also be taken into consideration that horizontal loading possibly change the state of stress (additional stress component along the longitudinal axis of the pipe), and this might accelerate void growth (Section 3.1.1), such that the fracture strain is reduced.

The force - displacement curve for zero-, constant- and linearly increasing loading is illustrated in Figure 4.25 along with the results of the new experiments with



## 4. Experimental Work

---

internal pressure. Horizontal loading is seen to particularly affect the last stage of deformation, where bending is the primary deformation mode.

### 4.2.4 Results

Unfortunately the experiment with constant horizontal loading (pipe 9) did not go exactly as planned. After 200 *mm* of indenter displacement, the indenter was removed while the horizontal actuators were fixed. Due to elastic forces which have built up in the pipe during deformation the pipe will be in a compressive state after the removal of the indenter. The pipe then exerts a force on the horizontal load cell when the horizontal actuators are fixed with regard to displacement: -40 *kN* in the pipe 8 experiment and -57.5 *kN* in the pipe 10 experiment. Due to some unknown error with the load control of the horizontal actuators, an additional horizontal force was added by the actuators such that the compressive load at maximum reached -106 *kN* at the end of the pipe 9 experiment. This load caused the pipe to be plastically bent, which caused a more narrow dent (Figure 4.22). A fracture also developed at the surface in the middle of dent along the symmetry line due to this additional loading. Thus the final results with regard to dent geometry, inner deformation etc. cannot be used for direct comparison with the other results. It is important to note that the sequence of horizontal loading during indenter deformation did go as planned, such that the force - displacement data before unloading still is valid.

Table 4.8 present a brief summary of the execution of the experiments. It is seen that the horizontal actuators gave an average resistance equal to 0.64 *kN* for pipe 8, which is the force needed to stretch out the actuators. The horizontal loading on pipe 9 was planned to be equal 50 *kN*, but was instead on average equal to 53.24 *kN*. However the same error occurred during the experiments without internal pressure (pipe 5) [5], where a constant horizontal load equal to 53 *kN* was applied. The experiment with linearly increasing loading was planned to be executed with a horizontal loading increasing from 0 to 50 *kN*. However, test

**Table 4.8:** Summary of relevant test results for pipe experiment 8, 9 and 10.

Pipe	8	9	10
<b>Horizontal loading</b>			
AVG [kN]	C <sup>a</sup> 0.64	C 53.24	Li <sup>b</sup> -1.85-52.94
SDEV [kN]	0.38	0.11	-
<b>Internal Pressure</b>			
AVG [bar]	103.56	102.99	102.86
SDEV [bar]	0.48	0.64	0.99

<sup>a</sup>C refers to constant

<sup>b</sup>Li refers to linearly increasing



**Table 4.9:** Pipe deformation after quasi-static impact. Measurements are according to Figure 4.6.

Pipe	8		9 <sup>a</sup>		10	
Inner def. [mm]	117		159		113	
Distance N-N [mm]	1200		1168		1200	
Outer dia. at [mm]	N-S	E-W	N-S	E-W	N-S	E-W
1 <sup>b</sup>						
2	131.00	130.92	130.96	130.84	131.21	131.41
3	130.93	131.01	130.82	130.93	131.03	131.28
4	130.70	131.47	130.34	131.49	130.12	131.66
5	127.90	134.29	126.44	134.48	127.52	134.27
6	98.13 <sup>c</sup>	151.90	90.30 <sup>c</sup>	163.93	96.69 <sup>c</sup>	151.76

<sup>a</sup>Not directly comparable due to compressive horizontal loading applied after indenter removal.

<sup>b</sup>Measurement point positioned in the unlathed area due to shorter inner length. The point was therefore omitted for measurement.

<sup>c</sup>Inaccurate measurement in the N-S direction.

data display that it was increased from -1.85 to 52.94 *kN*. The comparable pipe 6 experiment (linearly increasing loading without internal pressure) was exposed to a linearly increasing loading from 0 to 53.1 *kN*.

It was seen that the application of internal pressure worked quite well. A slightly higher pressure than 100 *bar* was observed, but the pressure was relatively constant during deformation. The pressure was also seen to be fairly similar for all experiments.

Overall the application of horizontal loading and internal pressure are deemed satisfactory such that comparison between experiments should be fully possible (except pipe 9 with regard to final geometry).

### Dent Geometry

The measurements according to Figure 4.6 are presented in Table 4.9. No big differences are observed when comparing pipe 8 and 10 (zero and linearly increasing horizontal loading). A 1.0 *mm* difference is observed on the N-S diameter at midspan (point 6), but this difference should not be taken as significant due the variation in wall thickness and accuracy the of measurements (as mentioned in Section 4.2.3).

It is perhaps more interesting to compare this results with the experiments without internal pressure. An overview of N-S and E-W diameter at midspan and inner deformation of pipe 4, 5, 6, 8, 9 and 10 is presented in Table 4.10. It is seen that the application of internal pressure increases the N-S diameter at midspan, i.e. the amount of local denting is reduced. Correspondingly the E-W diameter

## 4. Experimental Work

---

**Table 4.10:** Comparison of relevant measures after deformation.

Pipe	4	5	6	8	9 <sup>a</sup>	10
Inner def. [mm]	120	120	122	117	159	113
<b>6 (N-S)</b> [mm]	83.70	89.13	86.55	98.13	90.30	96.69
<b>6 (E-W)</b> [mm]	164.34	164.69	164.41	151.90	163.93	151.76

<sup>a</sup>Not directly comparable due to compressive horizontal loading applied after indenter removal.

is less increased (initially 122 mm) in case of internal pressure. It is perhaps also interesting to observe that the final inner deformation seems to be less in case of internal pressure (especially pipe 10), despite that all pipes were exposed to the same global deformation. This might indicate that internal pressure leads to a larger amount of spring back after deformation.

Close-up pictures of the respective dents of pipe 4, 5, 6, 8, 9 and 10 are given in Figure 4.22. The above mentioned observation (internal pressure reduce denting) is also seen in these pictures. It can be seen, by close investigation, that internal pressure seems to result in a more localized dent. The length L (Figure 4.9) seems to be reduced compared to the experiments without pressure. However, as previously mentioned, the largest strains are present in the middle of the dent, along the symmetry line, meaning that this localization not necessarily leads to higher strains in the critical region.

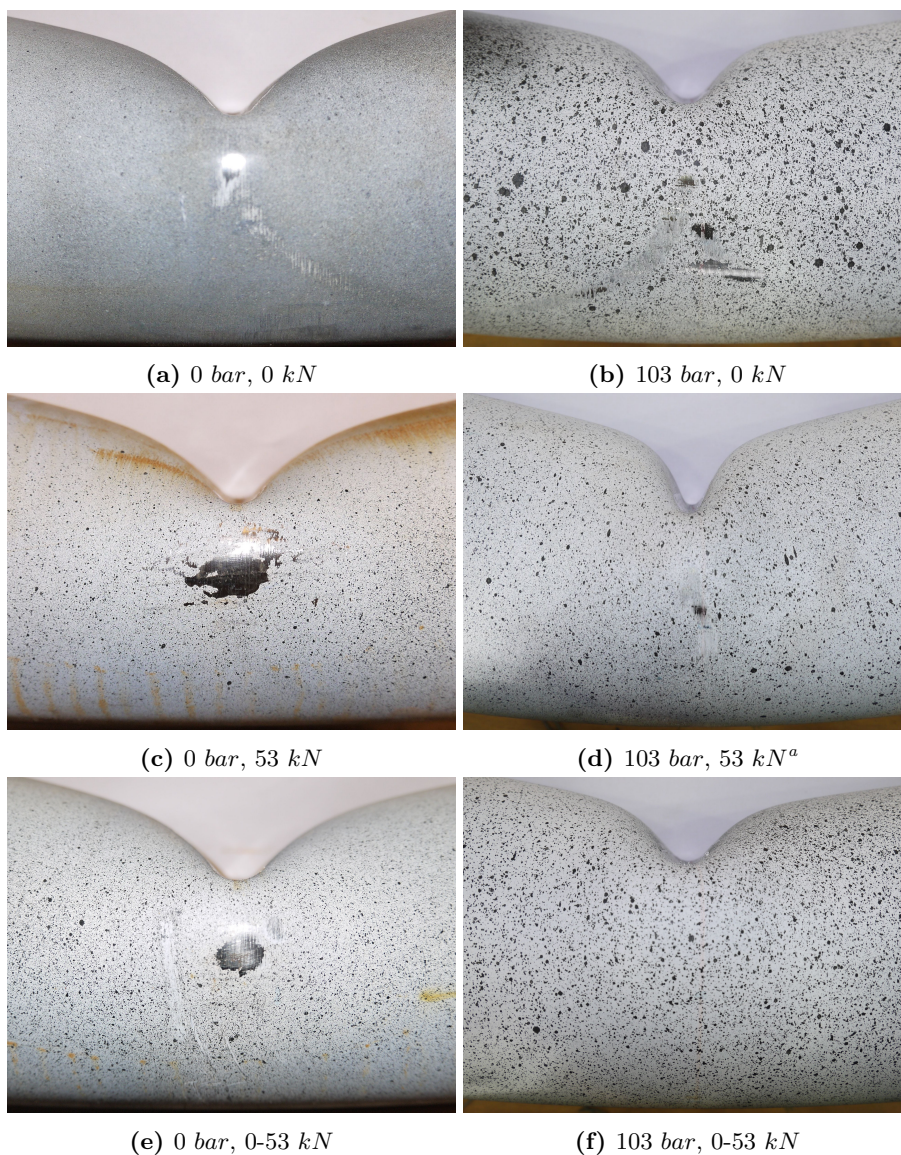


**Figure 4.22:** Comparison of local denting for different cases of loading after complete unloading.

<sup>a</sup>Not directly comparable due to compressive horizontal loading applied after indenter removal.

### DIC Results

When carrying out the analysis, the surface of the pipe is divided into a mesh of rectangular elements, in which the in plane strains are calculated. Then by assuming constant volume during plastic deformation, the out of plane strain component is calculated. From this the von Mises equivalent strain, plotted in Figure 4.23 and 4.24, is calculated (Section 2.4.2).

A comparison of the magnitude of equivalent strain between loading with and without internal pressure for different magnitude of indenter displacements are given in Figure 4.23 and 4.24. Figure 4.23 gives a comparison between cases with constant horizontal loading (pipe 5 and 9), and Figure 4.24 gives a comparison with linearly increasing loading. Unfortunately no DIC results are available for the pipe 4 experiment, due to incorrect positioning of the cameras. Thus comparison in case of zero axial loading is not available.

The process of correlation between pictures is highly sensitive to variations in light. As can be seen, a lot of noise is present in many of the pictures. Such noise also lead to element distortion and miscalculation of the respective strains. Distorted elements have thus been deleted during the analysis. A shaded area is also present on the left hand side in two of the series (pipe 5 and 6), making it impossible to calculate the strain field in these areas.

Figure 4.22 illustrates how internal pressure seem to localize denting and change the geometry of the dent. It was thus expected to see some changes with regard to the strain field when comparing DIC results. But to point out any such effects by evaluating either Figure 4.23 or 4.24, is from our point of view, unfortunately not possible. However, this does not imply the absence of any such effects. It might as well be the quality of the DIC analysis that is insufficient.

## 4.2. Quasi-Static Bending of Pressurized Pipes With Horizontal Axial Loading

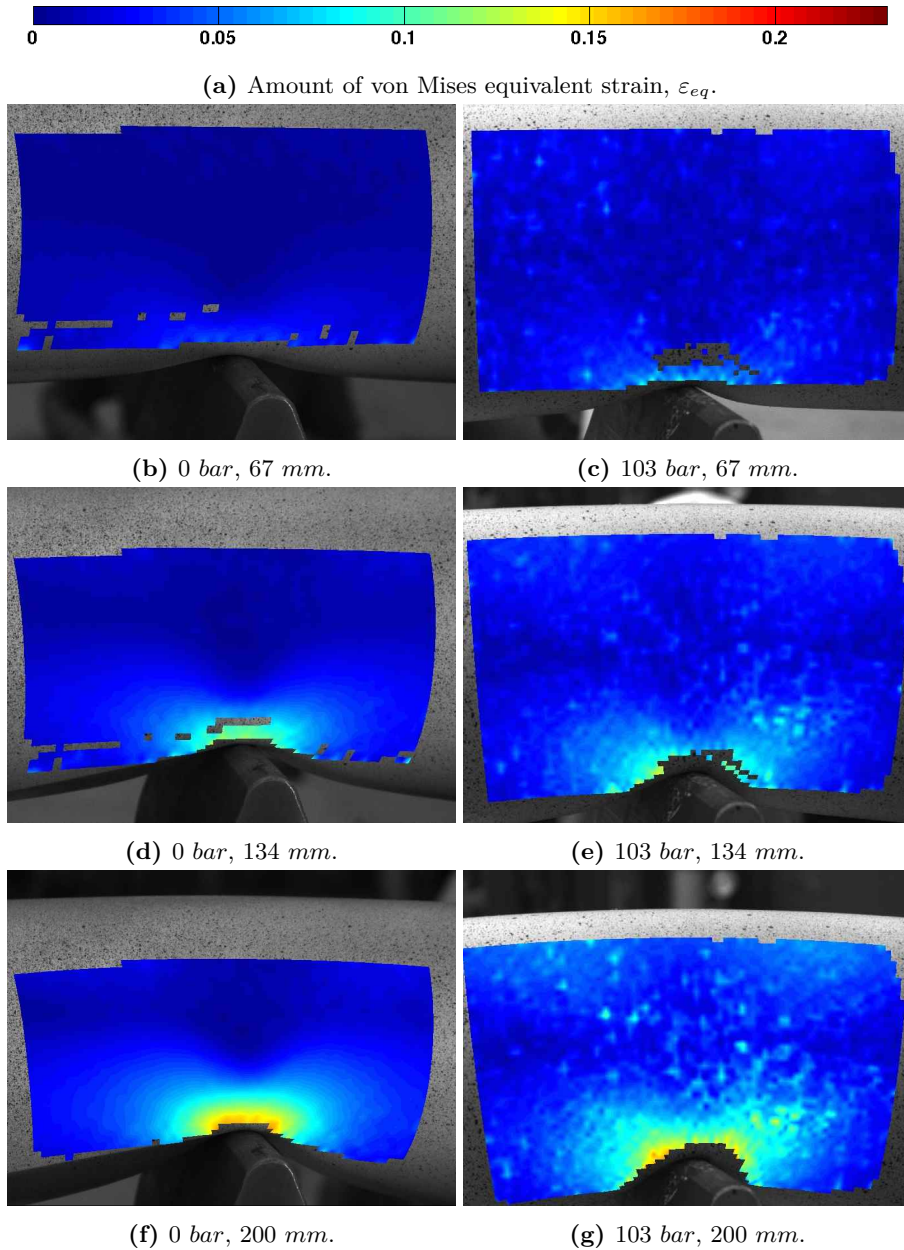


**Figure 4.23:** Comparison of the equivalent strain on the surface for different amounts of indenter displacement with a constant horizontal loading (53 kN). Pipe 5 and 9 on the left and right hand side, respectively. Note the different scale/zoom between the two series.



#### 4. Experimental Work

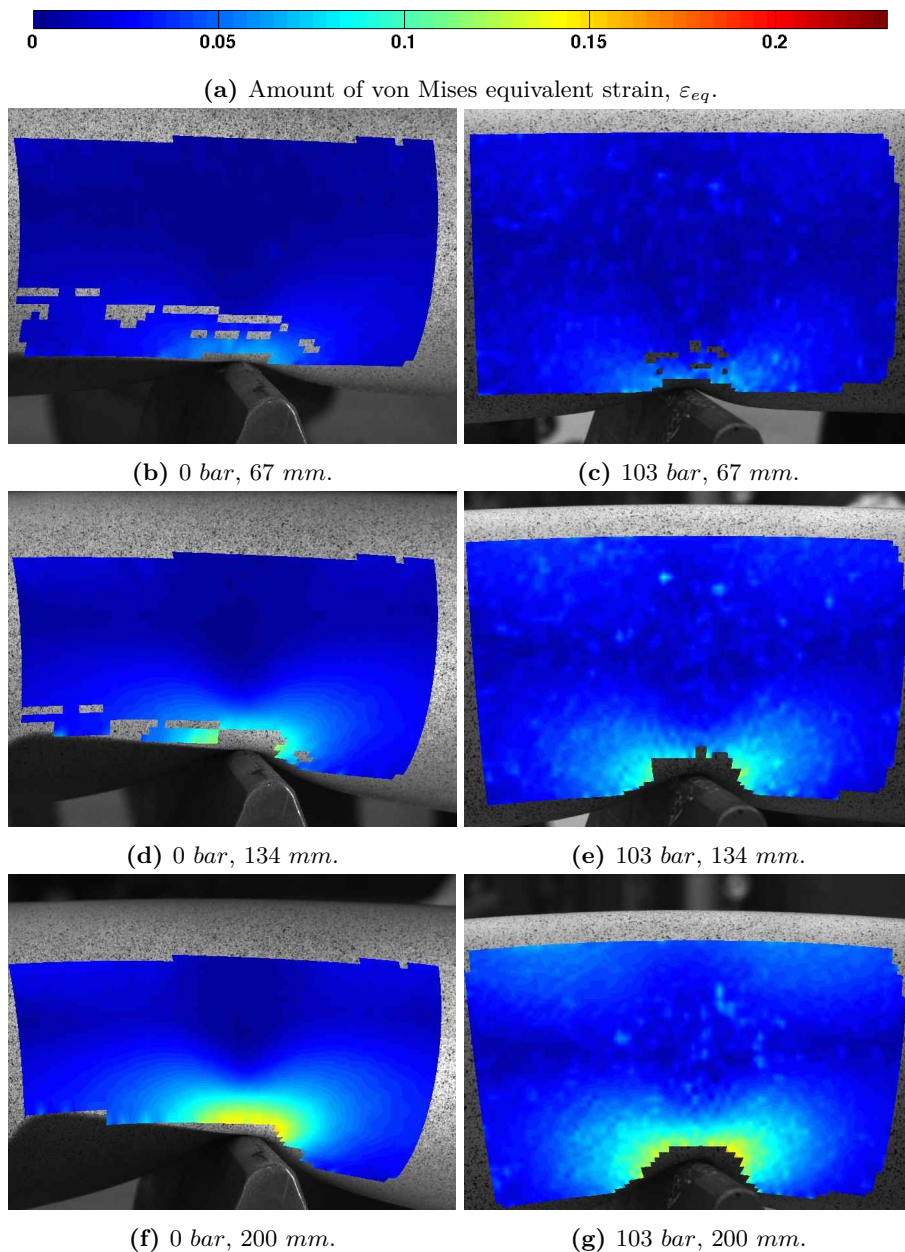


**Figure 4.24:** Comparison of the equivalent strain on the surface for different amounts of indenter displacement with a linearly increasing horizontal loading (0-53 kN). Pipe 6 and 10 on the left and right hand side, respectively. Note the different scale/zoom between the two series.

### Force-Displacement

**Dimensional.** A dimensional indenter force - indenter displacement plot is given in Figure 4.25. The corresponding curves from quasi-static impact without internal pressure is included for comparison. It is important to keep the variation in wall thickness in mind when comparing results (Table 4.5 and 4.6).

The same trend that was observed for the experiments without internal pressure is also seen for the experiments with internal pressure: horizontal loading increase the stiffness with regard to transverse loading. This effect is particularly seen in the last phase, characterized as pure bending (Section 4.1.4).

When comparing the average vertical force (Table 4.11), it can be seen that the difference between constant and linearly increasing loading is quite small. This suggest that horizontal loading is of minor importance in the initial denting phase.

When comparing results between the experiments with and without internal pressure (continuous vs. dashed lines, respectively) it can be seen that internal pressure increase the stiffness in all phases of deformation. The difference is increasing in size with displacement.

The fairly equal absolute and relative difference might indicate that the effect of pressure is independent of horizontal loading. However since the wall thickness variation (from 3.95 to 4.20 mm) not is accounted for, it is hard to make any conclusions.

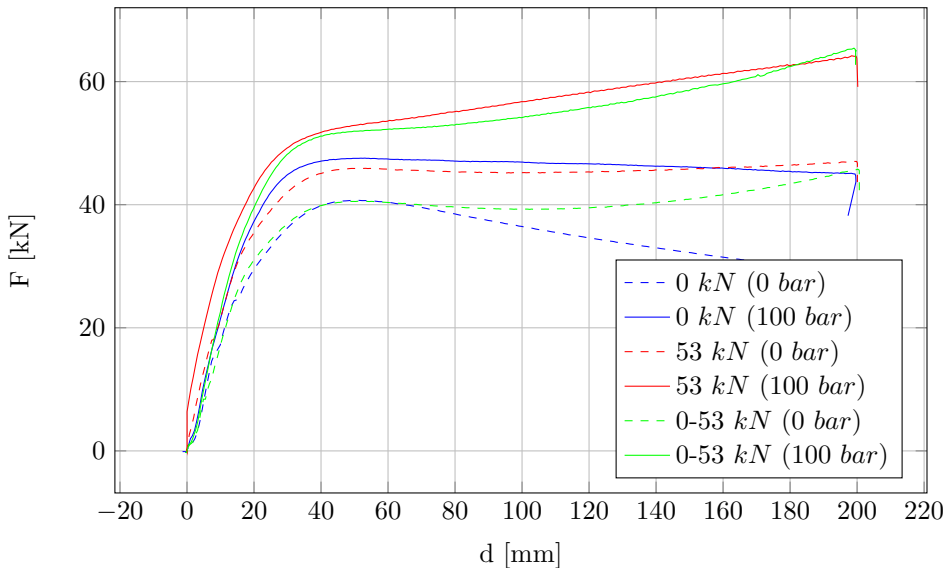


**Figure 4.25:** Dimensional force-displacement plot for quasi-static tests: pipe 4, 5, 6, 8, 9 and 10.

## 4. Experimental Work

---

**Table 4.11:** Comparison of average indenter force.

Case	Without Pressure AVG [ $kN$ ]	With Pressure AVG [ $kN$ ]	Abs.Diff. [ $kN$ ]	Rel.Diff. <sup>a</sup>
<b>0</b> $kN$	32.5	42.81	10.31	31.7%
<b>C 53</b> $kN$	38.11	52.13	14.02	36.8%
<b>L 0-53</b> $kN$	40.06	50.59	10.53	26.3%

<sup>a</sup>Difference relative to loading without pressure.

**Dimensionless Results.** A dimensionless plot is presented in Figure 4.26, where each pipe is scaled with the denting stiffness as proposed in Section 4.1.4, i.e. the variation in wall thickness is accounted for by calculating an average denting force needed to deform a dent with a specific geometry similar on all pipes. The same parameters were chosen as in Section 4.1.4.  $B$  was chosen as the indenter-width equal to  $20\text{ mm}$  and  $\Delta$  and  $L$  (Figure 4.9) were set equal to  $10\text{ mm}$  and  $100\text{ mm}$ , respectively. The displacement,  $d$ , is scaled with the average pipe diameter. The recorded indenter force,  $F$ , were then scaled with the average denting force,  $F_{avg}^{denting}$  (Equation 4.13).

The results seem fairly satisfactory, where the positioning of the curve for linearly increasing loading perhaps is the best measure. It is positioned between zero and constant loading in all phases of deformation, which is what one would expect, contrary to what can be observed in the dimensional plot (Figure 4.25).

The same comparison of average force as was presented in Table 4.11 is presented in Table 4.12, only now for the average dimensionless force. Given that the dimensionless plot is physically reasonable, it can be seen that the absolute and relative difference in average indenter force are approximately the same. This suggests that the additional stiffness due to internal pressure is independent of horizontal loading with respect to the cases of loading discussed in this section.

**Table 4.12:** Comparison of average dimensionless indenter force.

Case	Without Pressure AVG [-]	With Pressure AVG [-]	Abs.Diff. [-]	Rel. Diff. <sup>a</sup>
<b>0</b> $kN$	0.65	0.88	0.23	35.4%
<b>C 53</b> $kN$	0.81	1.08	0.27	33.3%
<b>L 0-53</b> $kN$	0.79	1.06	0.27	34.2%

<sup>a</sup>Difference relative to loading without pressure.



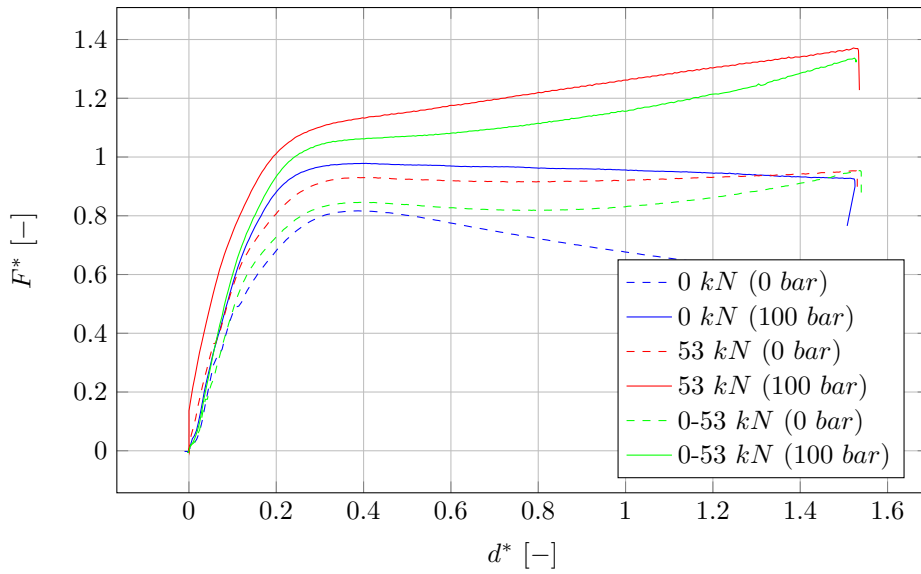


**Figure 4.26:** Dimensionless force-displacement plot for quasi-static tests: pipe 4, 5, 6, 8, 9 and 10.

### 4.3 Concluding Remarks

The quasi-static experiments discussed in Section 4.1 proved fracture to be dependent on dynamic loading. The internal and external cracks found after dynamic impact on pipe K and L, can not be recreated in a quasi-static experiment (Figure 4.27). The cause of this rather large difference between quasi-static and dynamic loading is not yet revealed.

To scale the indenter force with a theoretical average denting force seem to be a good procedure to account for wall thickness variations (Figure 4.10 and 4.26).

Application of internal pressure seems to reduce local denting, in addition to creating a more localized dent. The increased stiffness of the pipe with regard to transverse loading, when pressurized, seem to be independent of horizontal loading in the range of loading considered here. Dimensionless results indicate a 33-35% increase in average transverse loading, however this may change if the amount of indenter deformation is changed.

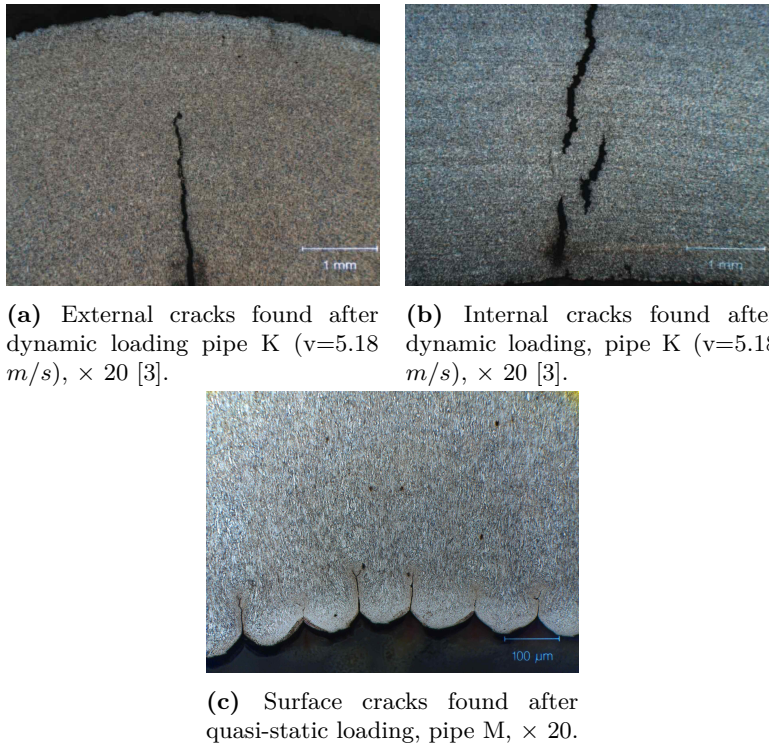


**Figure 4.27:** Comparison of crack formation after dynamic and quasi-static loading.

## Chapter 5

# Finite Element Analysis

Experimental work in the previous chapter concluded fracture to depend on dynamic loading and to be present before stretching. It is of interest to carry out Finite Element Analysis (FEA) to investigate if it is possible to predict fracture using the Cockcroft-Latham fracture criterion, introduced in Section 3.3. The analysis will concentrate around the pipe K experiment (dynamic impact at 5.18  $m/s$ ), because this was the most heavily deformed pipe. An essential part in doing this is to determine the number of elements needed in the impacted zone to get convergence on relevant measures of strain and stress.

The analyses will be conducted using the software Abaqus, explicit time integration and solid elements. Previous work has proved such analyses to be computationally expensive. It will be investigated if it is possible to utilize a modeling technique known as submodeling to carry out refined analysis of the impacted area such that computational costs can be saved.

Experiments on pipes with internal pressure showed that pressure reduced the magnitude of local denting and increased the stiffness. FEA will be carried out to determine if it is possible to recreate this behaviour and to get a deeper understanding of how internal pressure affects the local strains and stresses that develop in the impacted zone of the pipe.

## 5.1 Theory

### 5.1.1 Time Integration

A dynamic problem can in the most general case be written as

$$[M]\{\ddot{\mathbf{D}}(t)\} + [C]\{\dot{\mathbf{D}}(t)\} + [K]\{\mathbf{D}(t)\} = \{\mathbf{R}^{ext}(t)\}. \quad (5.1)$$

Here  $[M]$ ,  $[C]$  and  $[K]$  are the mass-, damping- and stiffness matrices, respectively.  $\{\mathbf{D}(t)\}$ ,  $\{\dot{\mathbf{D}}(t)\}$  and  $\{\ddot{\mathbf{D}}(t)\}$  are vectors containing the displacement, velocity and acceleration of every Degree Of Freedom (DOF) at every node in the system.  $\{\mathbf{R}^{ext}(t)\}$  is the external force vector, expressing the external loading. The matrices are of dimension  $N_{DOF} \times N_{DOF}$ , while the vectors are of dimension  $N_{DOF} \times 1$ .  $N_{DOF}$  are the total number of DOFs in the system.

This is a time dependent system which must be solved iteratively forward in time: from  $t_n$  to  $t_{n+1}$ . This can be done either by implicit or explicit time integration. Explicit time integration implies that the displacements at the following time increment,  $t^{n+1}$ , are calculated directly from one or more preceding time steps ( $t \leq t^n$ ), without solving any system of equations. Implicit time integration implies that the displacements at time  $t^{n+1}$  are calculated indirectly from the equilibrium conditions at time step  $t^{n+1}$ , meaning that solving a system of equations is needed [14].

While implicit integration always maintains equilibrium (unconditionally stable) explicit time integration just leaps forward in time without any guarantee of equilibrium (conditionally stable). However this is done at a much cheaper computational cost since equation solving is not needed. The advantage of doing implicit time integration is that larger time steps can be used. However since dynamic impact of pipes is a short duration event, small time steps will in any case be needed to ensure that all dynamic effects are captured. Explicit time integration will therefore be the integration method used throughout this work.

### 5.1.2 Stability

Stability in explicit time integration is first of all maintained by ensuring that the time step used,  $\Delta t$ , is less than the critical time step,  $\Delta t_{cr}$ . The critical time step is in the general case of an undamped system<sup>1</sup> given as

$$\Delta t_{cr} = \frac{L}{c_d}, \quad (5.2)$$

where  $L$  is the smallest element length and  $c_d$  is the speed of sound in the material.  $c_d$  can be found as

$$c_d = \sqrt{\frac{E}{\rho}} \quad (5.3)$$

---

<sup>1</sup>Damping reduce the stability limit even further [14].

where  $E$  is the Young's modulus and  $\rho$  the density of the element material. This condition is known as the CFL-condition (Courant, Friedrichs and Lewy), and it states that information shall not travel through any element during one time step to maintain stability [47]. This is a very important condition to keep in mind when carrying out numerical explicit analyses because it implies that mesh refinement not only increase  $N_{DOF}$ , but also the number of necessary time increments. I.e. mesh refinement will lead to a rapid increase in the computational effort needed.

### 5.1.3 Energy Balance

A sufficiently small time step does not necessarily guarantee that the solution is physically meaningful. In addition to comparing numerical results with physical results (if available), it is important to check the energy balance of the analysis. The total energy of the system should approximately be constant during the analysis, meaning that energy not disappear nor come into being by artificial numerical effects. The total energy,  $E_{tot}$ , in Abaqus is defined as<sup>2</sup>

$$E_{tot} = E_K + E_{SE} + E_{PD} + E_{AE} + E_{VD} + E_{FD} - E_{WK} - E_{PW} - E_{CW}. \quad (5.4)$$

The different quantities are explained in Table 5.1.

It is worth noting the two non-physical quantities,  $E_{AE}$  and  $E_{VD}$ , introduced to maintain numerical stability. Abaqus introduce an artificial stiffness to each element to prevent mesh instability when using reduced integration, commonly known as "hourglassing". The hourglass mode of deformation does not cause any strain in the respective element integration point. I.e. zero element stiffness is triggered and the element can thereby deform freely in so called hourglass modes. The total work done by this artificial stiffness is denoted as  $E_{AE}$ . According to Simulia Nordic (Nordic supplier of Abaqus), the artificial strain energy should be less than 1% relative to the internal energy ( $E_{PD}+E_{SE}+E_{AE}$ ) of the system. In addition, Abaqus introduces damping to control high-frequency oscillations, in the form of bulk viscosity, triggered by volumetric straining. The energy dissipated through this artificial viscosity is denoted as  $E_{VD}$ .

**Table 5.1:** Energy definitions [15].

$E_K$	Kinetic energy
$E_{SE}$	Elastic strain energy
$E_{PD}$	Energy dissipated through plastic work
$E_{AE}$	Artificial strain energy
$E_{VD}$	Energy dissipated through viscous damping
$E_{FD}$	Energy dissipated through friction
$E_{WK}$	Work done by external forces
$E_{PW}$	Work done by contact penalties
$E_{CW}$	Work done by constraint penalties

<sup>2</sup>Irrelevant energy quantities in this type of problem such as heat flux are omitted.

### 5.1.4 Locking

Finite elements based on a pure displacement formulation may behave to stiffly when exposed to certain modes of deformation, because the stresses not are approximated correctly. Two such effects associated with bending is so-called shear- and volumetric locking. It should also be noted that both effects reduce with mesh refinement.

#### Shear Locking

Shear locking is a phenomena which occurs when a fully integrated linear element is exposed to bending. In case of pure bending, the element takes on a trapezoidal shape, instead of the expected with curved inner and outer surfaces (Figure 5.1). This behaviour impose shear strains in the respective integration points that not really exist. Thus shear stiffness of the element is activated, making the element behave to stiffly [48]. The activated shear stiffness increases with decreasing aspect ratio (height to width) of the element and magnitude of bending. When using reduced integration, the integration point is positioned at the center of the element, in which shear strains do not occur. I.e. shear locking is avoided when using reduced integration.

#### Volumetric Locking

Volumetric locking is a phenomena which also is associated with bending of a fully integrated linear element. In case of pure bending a linear field in the thickness direction (y-direction) of normal "x-strains" will be present in the element. However the element is not able to create a linear field in the thickness direction of perpendicular "y-strains" that can compensate this field. I.e. the element is not able to bend without changing the volume at each integration point. This effect increase in size with Poisson's ratio  $\nu \rightarrow 0.5$  (incompressibility) [48] or incompressible plastic deformation [15]. This change of volume cause spurious normal "y-stresses" to develop in the integration points such that the element

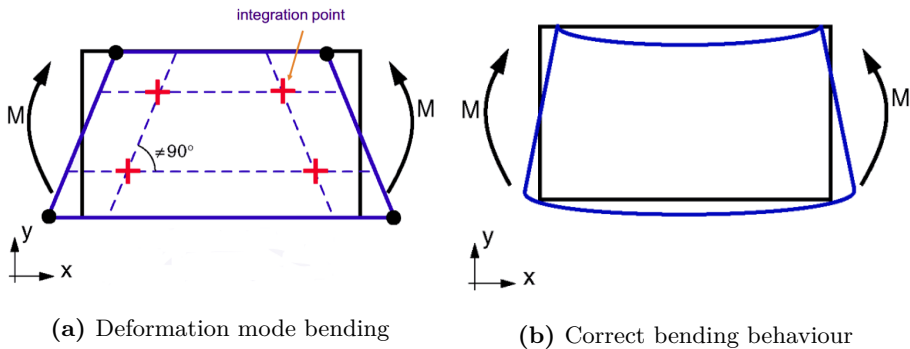


**Figure 5.1:** Bending of a fully integrated linear element compared to a realistic bending mode.

behave behave to stiff. With an integration point in the centre of the element (reduced integration) the normal strains associated with bending is zero, and thus volumetric locking is not triggered.

### 5.1.5 Submodeling

Submodeling is an analysis technique offered in Abaqus which enables the user to carry out refined analyses on specific regions of interest on a larger global model. The displacements or stresses from a global model is used to drive a smaller submodel with a refined mesh/geometry. The procedure can be summarized as follows:

**Step 1** Run a "coarse" global analysis of the problem.

**Step 2** Create a submodel of the global model.

**Step 3** Define boundaries on the submodel in which variables from the global model are to be transferred.

**Step 4** Run the submodel analysis using the transferred variables from the global model to drive deformation of the submodel.

It is important to note that the only link between the submodel and the global model is this transfer of variables. The most general procedure is to transfer the displacements, so called node-based modeling. This is recommended for analyses where the deformation of the submodel and the global model is expected to be approximately the same, and analyses involving large rigid body motions [15]. Node-based modeling will thus be attempted in this thesis.

### 5.2 Material Model

Slåttedalen and Ørmen [1] calibrated a Johnson-Cook material model (isotropic hardening) including strain rate dependency. The calibration was based on uniaxial tension tests on axisymmetric smooth specimens (Figure 3.19), tested both quasi-statically and at elevated strain rates. The specimens were cut from a X65 steel pipe at different locations, and their tests proved the material to be isotropic with homogeneous properties through the cross section. Based on the average values from 12 tests, the material was found to yield at  $478 \pm 15$  MPa, have nominal peak stress of  $572 \pm 14$  MPa and strain hardened to a true peak stress of  $1314 \pm 12$  MPa. A strain rate dependency with regard to the flow stress was detected and included in a Johnson-Cook material model. When adopted on the pipe impact problem and compared with experimental results, the model provided good results on the force response during impact, however a much too stiff behaviour was found during subsequent stretching.

Fornes and Gabrielsen [2] investigated the kinematic properties of the X65 steel. Compression-tension and tension-compression tests were conducted on uniaxial specimens at relatively low values of pre-compressive/tension strain (0-10%). A combined hardening model was developed which included isotropic hardening expressed by the Voce equation (2.41) and kinematic hardening expressed by the Armstrong-Fredericks equation (2.43). The combined material model generally resulted in a softer behaviour. This implied better compliance in subsequent stretching however at the cost of underestimating the force response during impact.

Aune and Hovdelien [3] addressed the problem that the pipe in reality was exposed to larger compressive strains than the ones used in the tensile tests performed by Fornes and Gabrielsen [2]. They conducted new compression-tension tests on notched uniaxial specimens (Figure 3.15) exposed to up to 40% compressive strain. New parameters for the Voce equation and the Armstrong-Fredericks equation were calibrated from their experimental results by inverse modeling. Their material model, when applied on the pipe impact problem resulted in a slightly improved compliance in subsequent stretching. However an additional small decrease in the force response during impact was detected, when compared with the model calibrated by Fornes and Gabrielsen [2]. Especially the force in the intermediate phase during impact, termed denting and bending (Section 4.1), was found to be underestimated when using the combined hardening model.

Subsequent stretching of the pipes has not been carried out as part of this thesis, neither numerically nor experimentally. However, special attention has been made to the load reversal that occurs when the pipe spring back after impact/loading with regard to fracture. The combined hardening model developed by Aune and Hovdelien [3] has therefore been used throughout the numerical work, because it seems to provide better results in case of load reversal. The material parameters used are presented in Table 5.2.



### 5.2.1 SIMLab Metal Model

The SIMLab Metal Model (SMM), is a subroutine developed by SIMLab for material definition. The model allows for definition of material properties outside the complete Abaqus environment (Abaqus/CAE). The model is applicable when modeling metals and alloys, and for use with either solid elements or shell elements [49]. SMM includes several yield surfaces, hardening rules and fracture models. The material properties are defined by a material card (Appendix A.3) which specifies the material effects to be included and the respective parameters [50].

The SMM enables the Cockcroft-Latham fracture criterion directly. The criterion specifies the element to be eroded when the integral

$$\int_0^{\varepsilon_f} \max(\sigma_1, 0) d\varepsilon_{eq}^p, \quad (5.5)$$

is equal to the material parameter  $W_{cr}$  in one of potentially multiple integration points of the respective element. The material parameter  $W_{cr}$  is based on the uniaxial tensile tests on smooth axisymmetric specimens, discussed in Section 3.3.2. The value used is given in Table 5.2.

A slightly narrowed yield surface has been adopted when using the SMM: Hershey surface (Section 2.3.1) with  $m=6$  is chosen since it is preferable for metals having a BCC structure (Section 3.2.1) [17].

The use of SMM does however add significant computational cost. SMM has therefore not been used when fracture was judged unlikely to occur (based on observations in the lab). In these cases the material was defined through Abaqus/CAE. I.e. no fracture criterion was included and a von Mises yield surface was used.

**Table 5.2:** The material constants.

<b>Elasticity</b>			E	$\nu$
			208000MPa	0.3
<b>Isotropic</b>				
<b>Hardening</b>	Voce-hardening law			
	$\sigma_0$	$Q_{R1}$	$\theta_{R1}$	$Q_{R2}$
	299MPa	160MPa	4000MPa	400MPa
				$\theta_{R1}$
				100MPa
<b>Kinematic</b>				
<b>Hardening</b>	Armstrong-Fredericks law			
		$Q_{\chi1}$	$\theta_{\chi1}$	$Q_{\chi2}$
		129MPa	50401MPa	100MPa
				$\theta_{\chi1}$
				1279MPa
<b>Visco-</b>				
<b>plasticity</b>			$\dot{\epsilon}_{eq}^{p,0}$	$C_\sigma$
			0.000806	0.0105
<b>Yield</b>				
<b>Criterion</b>	Hershey criterion			
				m
				6
<b>Fracture</b>	Cockcroft-Latham criterion			
				$W_{cr}$
				1595MPa
<b>Other</b>				
				$\rho$
				7850 kg/m <sup>3</sup>

## 5.3 Quasi-Static Bending of Pressurized Pipes With Horizontal Axial Loading

### 5.3.1 Numerical Model

The two planes of symmetry present were exploited such that only one quarter of the pipe was modeled. The model consisted of three parts: the pipe itself, a rigid indenter and a rigid link tied to the cross sectional end of the pipe (Figure 5.2). The rigid link rotated and translated about an external reference point, defined with a horizontal offset equal to  $423\text{ mm}$ , to comply with the experimental setup (Section 4.2.1). Pressure was applied on the whole inner surface (both the pipe and the rigid link). Horizontal loading was applied through the reference point tied to the rigid link.

The analyses were carried out through four steps of loading, analogous to the lab experiments. Internal pressure and initial horizontal axial loading were applied gradually in the first step to avoid causing unwanted stress waves that could possibly affect the response of the pipe. The magnitude of pressure and horizontal axial loading was according to the measured values from the experiment in the lab (Table 4.8). The indenter moved vertically  $200\text{ mm}$  at a constant velocity equal to  $25\text{ mm}/\text{min}$  in the second step. However, the indenter was initially smoothly accelerated over a time period of  $100\text{ s}$ . This rather low acceleration was needed to minimize inertial effects due to mass scaling. Unloading was carried out through two steps: Unloading 1 and 2. During Unloading 1, the indenter reversed and moved vertically away from the pipe, while the rigid links were constrained with regard to horizontal movement. During Unloading 2, the constrained rigid links were released such that the pipe could spring back completely.

All pipes were meshed relatively coarse. Three elements over the thickness with a bias on element size along the longitudinal axis of the pipe.  $1.4 \times 3.0 \times 1.2\text{ mm}^3$

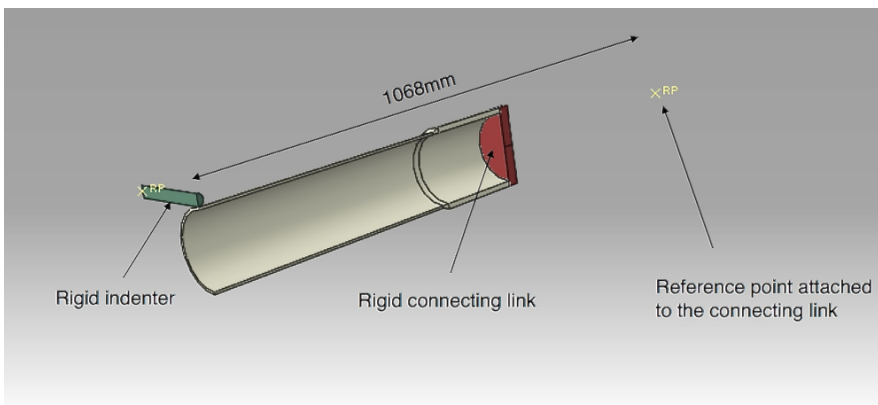


**Figure 5.2:** Numerical model of pipe experiments 8, 9 and 10.

## 5. Finite Element Analysis

---

**Table 5.3:** Load steps in analysis

Step	Duration	Description
Pressurization	30 s	Smooth application of internal pressure and initial horizontal loading.
Deformation	532 s	200 mm indenter movement. Smoothly accelerated up to constant velocity.
Unloading 1	25 s	Indenter removal with fixed rigid links.
Unloading 2	40 s	Complete spring back. Deactivated interaction between pipe and indenter.

at midspan, versus  $1.4 \times 3.0 \times 10 \text{ mm}^3$  at the end of the lathed area (Figure 5.3), giving in total approximately 26 000 elements. Linear eight noded, solid elements with reduced integration (C3D8R) were used to save computational costs and avoid locking (Section 5.1.4).

Fracture was not expected to occur and the material was defined through Abaqus/CAE. Isotropic hardening were tabulated according to the Voce-hardening law for different strain rates (Abaqus does not support parametric definition when using the Voce-hardening law). Kinematic hardening was included through the Armstrong-Frederick equation. For more details on how to define a combined (isotropic and kinematic) viscoplastic material model in Abaqus it is referred to [3] and [15]. The von Mises yield criterion was used and a surface-to-surface penalty interaction was defined between the indenter and the pipe. The analyses were run in double precision.

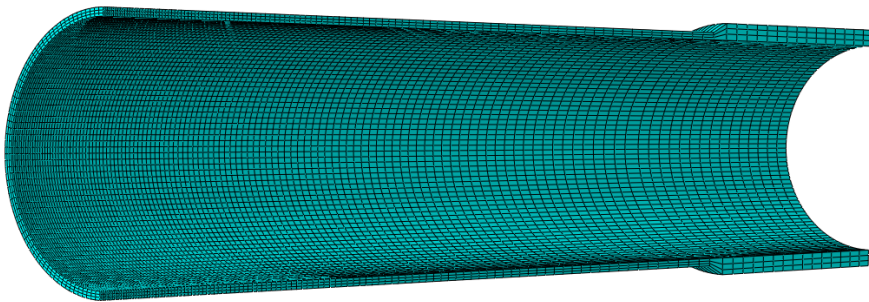


**Figure 5.3:** Mesh used in the numerical pipe 8, 9 and 10 experiment.

### 5.3.2 Results

#### Mass Scaling

To reduce the CPU-time needed, scaling was applied to the model. This can usually be done either by scaling the rate of deformation (time scaling) or by increasing the density of the material such that the critical time step (Equation (5.2)) is increased (mass scaling). The appropriate magnitude of scaling is however case dependent and must be found by trial and error.

Due to the strain rate sensitivity of the material, mass scaling was applied. The same magnitude of scaling was applied to the whole pipe for simplicity, contrary to variable mass scaling where only the mass of the smallest elements are scaled. Analyses of the pipe with internal pressure and zero horizontal loading (pipe 8) with densities scaled by  $10^8$ ,  $10^7$ ,  $10^6$  and  $10^5$  were carried out to map the effect and to determine the proper magnitude of scaling to be adopted in the subsequent analyses.

The force-displacement plot for different magnitudes of scaling is given in Figure 5.4. It can be seen that mass scaling introduces oscillations in the force response. These oscillations were found to reduce when the acceleration of the indenter was decreased (increased length of the defined smooth amplification). This is why a rather slow acceleration is chosen in all the analyses. The indenter is accelerated up to a constant velocity of  $25 \text{ mm/min}$  over a time period of  $100 \text{ s}$ . The cost of doing this is that the total time of the analysis is correspondingly increased.

The last step of unloading (Unloading 2) complicates the analysis because the experiment is changed from being quasi-static to being dynamic, because the

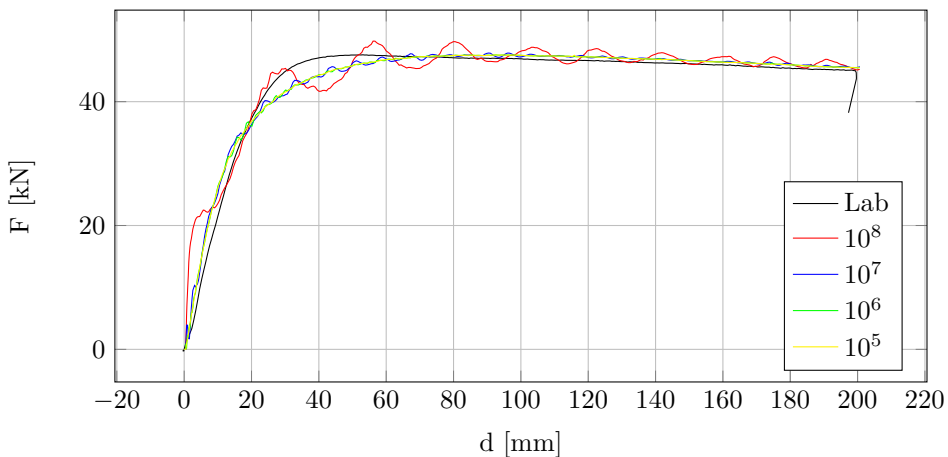


**Figure 5.4:** Force-displacement plot for different magnitudes of mass scaling on the model with zero horizontal loading (pipe 8).

## 5. Finite Element Analysis

---

**Table 5.4:** Comparison between different magnitudes of mass scaling on the pipe with zero horizontal loading (pipe 8).

Scaling	CPU-time <sup>a</sup>	% $E_K$ <sup>b</sup>	% $F_{\text{avg}}$ <sup>c</sup>	$\varepsilon_{\text{eq}}^{\text{p.def}}$ <sup>d</sup> [-]	$\varepsilon_{\text{eq}}^{\text{p.unl}}$ <sup>e</sup> [-]
$10^8$	1:00	0.9%	-4.97%	0.501	0.726
$10^7$	3:10	0.09%	-6.48%	0.474	0.709
$10^6$	9:09	0.009%	-6.64%	0.461	0.740
$10^5$	30:06	0.0009%	-6.66%	0.459	0.795

<sup>a</sup>Total wall-clock time when 8 CPUs are used.

<sup>b</sup>Magnitude of kinetic energy after indenter deformation (before unloading), relative to the internal energy,  $E_I$ .

<sup>c</sup>The average transverse indenter force, relative to the average indenter force measured in the lab (Table 4.11).

<sup>d</sup>Maximum equivalent plastic strain, after indenter deformation.

<sup>e</sup>Maximum equivalent plastic strain, after complete unloading.

horizontal restriction is instantly removed. When the horizontal actuators are released, the stored elastic energy in the pipe is released and the pipe springs back to its equilibrium state without any external resistance. The same procedure was followed in the lab, however in that case the horizontal actuators most likely contributed with significant resistance. Zero external damping was brought into the numerical model, and this caused the pipe to oscillate around a state of equilibrium to a small degree at the end of Unloading 2.

The spring-back phase was seen to contribute to a large increase in plastic deformation. The magnitude of equivalent plastic strain,  $\varepsilon_{\text{eq}}^{\text{p}}$ , increased approximately from 0.46-0.50 to 0.71-0.80 in the critical element, depending on the magnitude of mass scaling (Table 5.4). I.e. the dynamics, affected by mass scaling, influenced the value of final plastic deformation. The magnitude of final equivalent plastic strain in the critical element is not seen to converge with respect to mass scaling.

To carry out a detailed analysis of this phase, one option could be to stop the quasi-static analysis after the first unloading step and then perform a restart operation with zero mass scaling to capture the dynamics of the experiment in a realistic way. And additionally, if possible, apply external damping analogous to what was done by Aune and Hovdelien [3], to find the final state of equilibrium. However, this is left for future work.

The average force (Table 5.4) is noted to converge with mass scaling up to  $10^7$ , such that if one is searching for the force response only, one might as well scale the density with  $10^7$ . This would result in a very effective analysis, only needing 3 hours to complete on eight CPUs. However it was decided to scale the mass

with  $10^6$  in the subsequent analyses to avoid the small oscillations in the force response and to presumably be able to make better indications of the trends with respect to straining after complete unloading.

### Force-Displacement

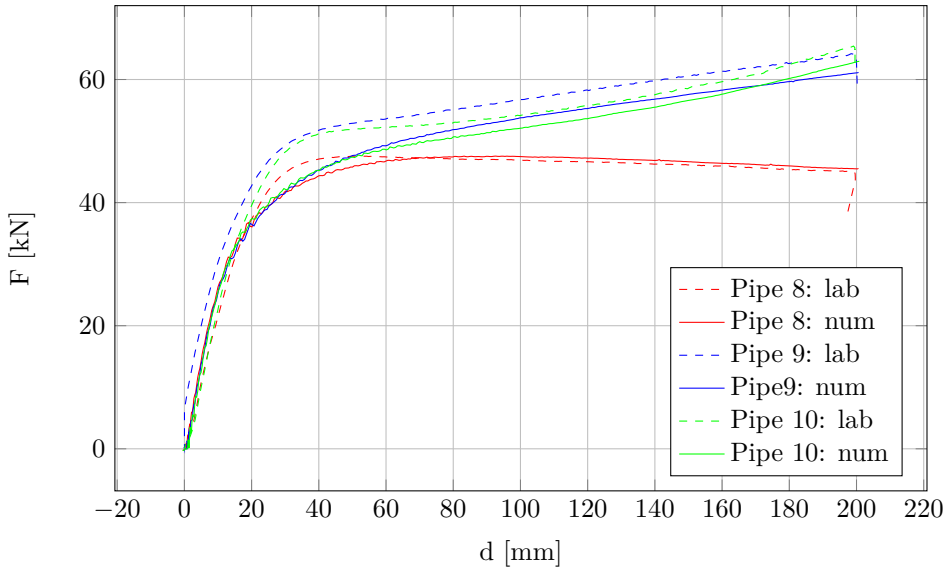


**Figure 5.5:** Pipe 8: "zero" horizontal loading ( $0.64 \text{ kN}$ ) and  $103.56 \text{ bar}$  internal pressure. Pipe 9: constant horizontal loading ( $53.24 \text{ kN}$ ) and  $102.99 \text{ bar}$  internal pressure. Pipe 10: linearly increasing horizontal loading ( $-1.85$ - $52.94 \text{ kN}$ ) and  $102.86 \text{ bar}$  internal pressure.

A comparison of the reaction force of the indenter versus the reaction force of the support indicate global equilibrium<sup>3</sup>. Some energy is seen to be absorbed by the artificial stiffness introduced to prevent hourglass modes, however this contribution is less than 1% relative to the internal energy. The maximum deviation in  $E_{tot}$  was noted to be approximately 0.3% relative to the internal energy. The simulations are thus deemed valid from a numerical perspective.

The force-displacement plot is given in Figure 5.5. All numerical models seem to underestimate the reaction force. Simulations of Pipe 8, 9 and 10 underestimate the average force by 6.63%, 9.40% and 11.61%, respectively. This is especially seen during the intermediate phase, characterized as the "denting and bending" phase (described in Section 4.1.4). A better compliance in this phase was reported by Asheim and Mogstad [4] when using only isotropic hardening. Some of the force underestimation may also be caused by inaccurate wall thickness

<sup>3</sup>This was not the case in the numerical work done by [4] on pressurized pipes with an imported mesh.

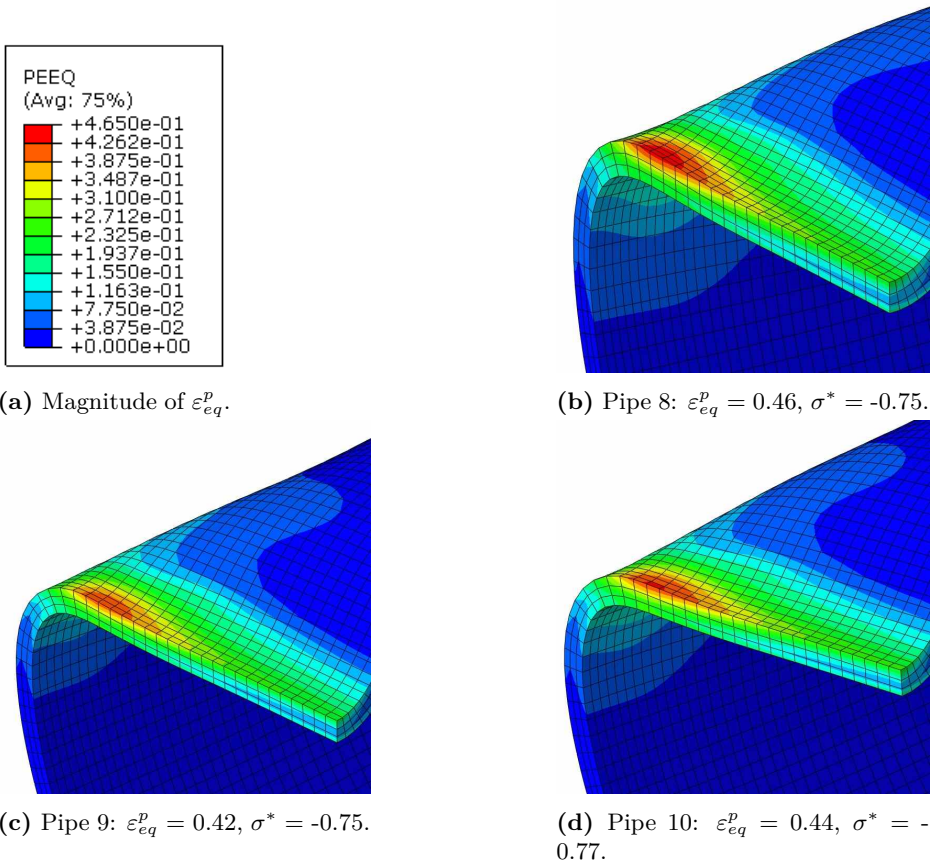


**Figure 5.6:** Comparison of equivalent plastic strain in the dented zone between different cases of horizontal loading after 200 mm indenter deformation, before unloading.  $\sigma^*$ , and  $\varepsilon_{eq}^p$  are given for the critical element with the highest value of  $\varepsilon_{eq}^p$  after unloading.

measurements or variations in the span length between the supports. That said, the main trend of increasing transverse force with horizontal loading, especially in the last phase, is well captured by these numerical models.

### Deformation

Comparison of the N-S diameter at midspan and inner deformation (Figure 4.6) between the experimental- and numerical results indicate that the value of denting, characterized by the N-S diameter is well captured. The numerical model of pipe 8 and 10 overestimated the N-S diameter with +6% (5.9 mm) and +4% (4.3 mm), respectively<sup>4</sup>. The value of inner deformation was underestimated with

<sup>4</sup>Pipe 9 was not available for comparison due to a error in the horizontal loading in the experimental tests (Section 4.2.4)



-16% (-19 mm) and -12% (-14 mm) for pipe 8 and 10, respectively. This might indicate that the rotation point was modeled to far from the rigid link<sup>5</sup>.

Figure 5.6 illustrates the differences in equivalent plastic strain and stress triaxiality in the dented zone after 200 mm indenter deformation (before unloading). No significant differences is noted on both parameters when horizontal loading is applied.

A large portion of the equivalent plastic strain develops when the pipe is unloaded, illustrated by a contour plot of equivalent plastic strain during unloading in Figure 5.7. Investigation of the pipe 8 model reveals that the magnitude of equivalent plastic strain increases from 0.46 to 0.74 when the pipe is unloaded<sup>6</sup> and spring back. The stress triaxiality changes from -0.74 to +0.58. This observation is of importance with regard to fracture. A negative stress triaxiality of -0.74 will most likely not allow voids to grow (illustrated as void locking in Figure 3.2). When the pipe is unloaded, the loading in the critical element is reversed from a compressive to a tensile state and the stress triaxiality is correspondingly changed to +0.58. Indicating that it is possible for ductile voids to grow and potentially coalesce and cause fracture.

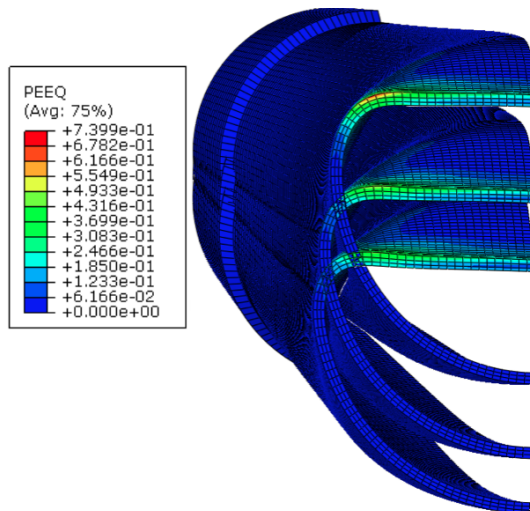


**Figure 5.7:** Overlay plot of different stages of unloading of the pipe 8 experiment, displaying the magnitude of equivalent plastic strain (PEEQ).

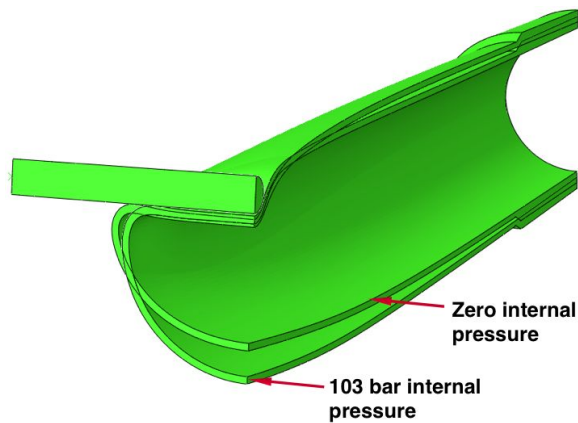
<sup>5</sup>The support width was not explicitly measured in the lab, and the used value is based on experimental setup described by [4, 5].

<sup>6</sup>Except internal pressure, however the application of internal pressure was seen to cause zero plastic straining when applied in the first step.

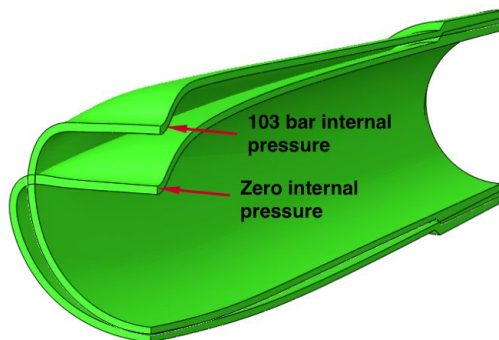
### 5.3.3 The Effect of Internal Pressure

To investigate the effect of pressure alone with regard to plastic deformation, the pipe 8 simulation was repeated without application of internal pressure. The difference in global deformation when the pipe is deformed with and without internal pressure is illustrated in Figure 5.8. It can be seen that internal pressure reduces the magnitude of denting such that more of the indenter deformation must be accounted for by bending. This influences how the pipe deforms when it is unloaded. The pressurized pipe is observed to spring back to a larger extent than the unpressurized, illustrated in Figure 5.8.

How this change in global deformation influences plastic deformation locally in the dent is illustrated in Figure 5.9. Here the magnitude of plastic deformation in the critical element (the element with the largest magnitude of equivalent plastic strain after unloading) is plotted against indenter deformation along with the



(a) After 200 mm indenter deformation.



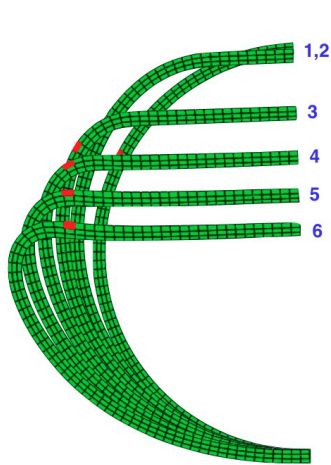
(b) After complete unloading.

**Figure 5.8:** Comparison of deformation between loading with and without internal pressure.

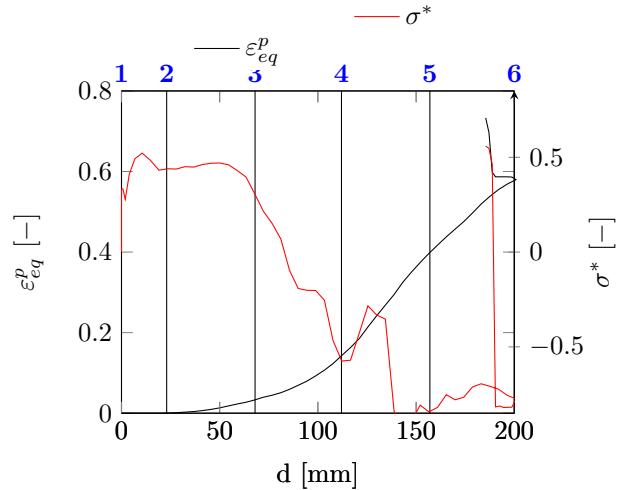
stress triaxiality.

The left figures illustrates how a plastic hinge moves in the circumferential direction as the cross section is dented. At first (stage 1-3) the critical element is plastically deformed in a state of high triaxiality (tension). I.e. the conditions for ductile void growth are very good (Section 3.1). Then, as the plastic hinge travels through the critical element (stage 3-6), a large increase in plastic deformation occurs. The stress triaxiality is shifted to a low, negative value (compression), meaning that it is much harder for voids to grow. The largest change of plastic deformation occur during this phase.

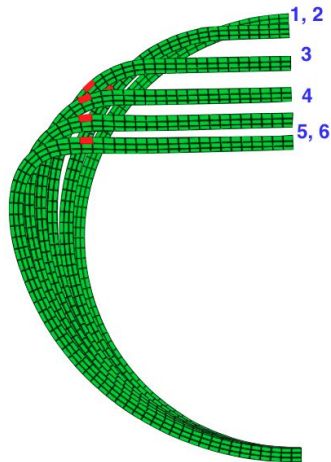
It can be seen that the critical element in the pipe without internal pressure is exposed to a larger magnitude of plastic deformation after 200 *mm* of indenter deformation (before unloading). When the indenter is removed (stage 6-), the critical element in the pressurized pipe is exposed to more plastic deformation than the element in the unpressurized pipe. This occurs simultaneously as the stress triaxiality is shifted to a positive value. Both pipes ends up with approximately the same magnitude of equivalent plastic strain in their respective critical elements after unloading. It is noted that a larger portion of plastic deformation occurs with a positive stress triaxiality in the pressurized pipe, indicating that the overall conditions for void growth presumably are better when the pipe is pressurized.



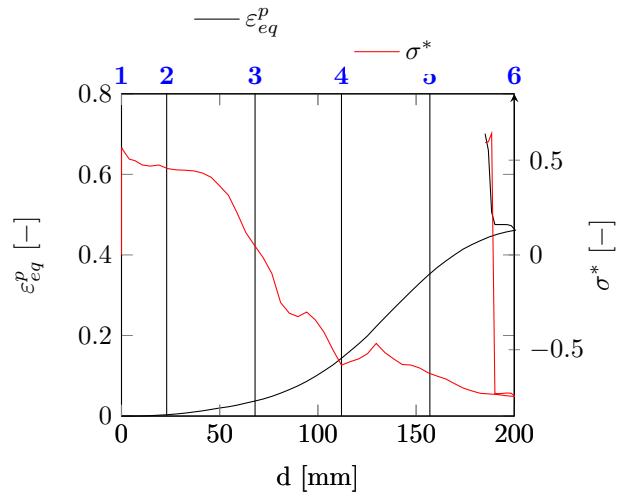
(a) Stages of deformation, 0 bar.



(b) 0 bar internal pressure.



(c) Stages of deformation, 103 bar.



(d) 103 bar internal pressure.

**Figure 5.9:** equivalent plastic strain,  $\varepsilon_{eq}^p$ , plotted against indenter deformation,  $d$ , along with the stress triaxiality,  $\sigma^*$ . Data are extracted from the element with the highest magnitude of equivalent plastic strain after loading and unloading (element marked in red).

#### Concluding Remarks

The force response of the pipe, in particular during the intermediate phase, characterized as denting and bending, is underestimated when using kinematic hardening and three elements through the wall thickness. However the general trend of increasing force response with application of horizontal axial loading is well captured.

Horizontal loading up to 53 *kN* on pipes with 103 *bar* internal pressure does not seem to influence the magnitude of equivalent plastic strain in the dented zone significantly.

A large increase in equivalent plastic strain is observed to occur in the dented zone when the pipe is unloaded, while at the same time the stress triaxiality is changed from approximately -0.7 to +0.6.

Comparison between FEA of pipes bended with and without internal pressure indicate that the pressurized pipe possibly is more prone to failure by ductile fracture. Because more plastic deformation seems to occur in tensile state (positive stress triaxiality) compared to the unpressurized when exposed to the same magnitude of indenter deformation. This is however only a numerical observation, not supported by experimental findings.

### 5.4 Quasi-Static Bending of Simply Supported Empty Pipes

The quasi-static experiments named pipe M and N, discussed in Section 4.1, were conducted to investigate if fracture also occurred in case of quasi-static deformation compared to dynamic deformation. Two numerical models of the quasi-static experiments were created to see if it was possible to recreate the behaviour seen in the lab and to gain further insight in the stress-strain history of the critical regions.

#### 5.4.1 Numerical Model

Both models were modeled according to the dimensions given in Table 4.2. The two planes of symmetry were utilized, meaning that only one quarter of each pipe was modeled to save computational time. Apart from the pipe, the assembly consisted of a support and an indenter (Figure 5.10). The support was modeled as an elastic cylinder, restrained against movement in all DOFs. The indenter was modeled as a rigid half cylinder, restrained against movement in all DOFs, except along the axis of deformation.

The pipes were meshed with 3 elements through the wall thickness and 68 in the circumferential direction. A bias in the longitudinal direction was used, such that the element size was increased from  $1.3 \times 2.9 \times 1.2 \text{ mm}^3$  at midspan to  $1.3 \times 2.9 \times 10 \text{ mm}^3$  at the end of the lathed region. Giving a total number of 27132 C3D8R-elements (Figure 5.11). The indenter and the support were meshed with an element size of  $3.5 \text{ mm}$  and  $7.1 \text{ mm}$ , respectively.

The numerical models were exposed to the same magnitude of indenter deformation as in the lab:  $350.07 \text{ mm}$  (pipe M) and  $139.90 \text{ mm}$  (pipe N). The indenter was smoothly accelerated, using a smooth step definition, up to a constant velocity of  $10 \text{ mm/min}$  equal to the rate used in the experiments. This smooth acceleration was implemented in order to prevent oscillations in the force re-

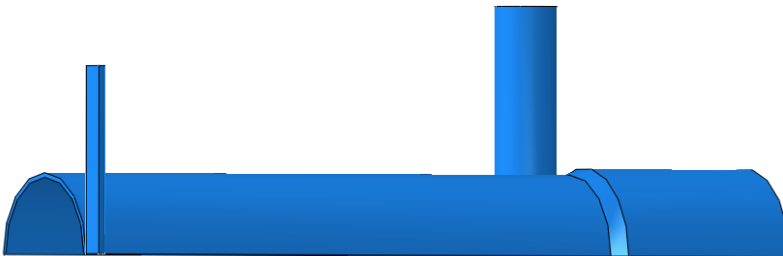


**Figure 5.10:** The set-up for pipe M and N.

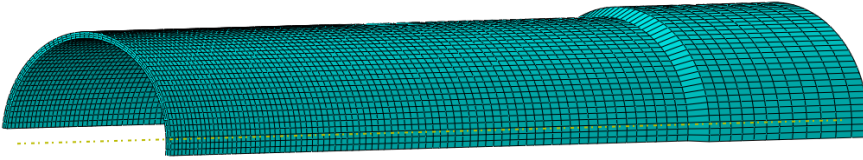


**Figure 5.11:** The mesh for pipe M and N.

sponse. The duration was set to 100 s and 80 s for pipe M and N, respectively. The duration of the experiments in the lab was 2100.2 s and 839.4 s for pipe M and N, respectively. Due to the acceleration of the indenter in the numerical models, the step time in the simulation was set to 2150.2 s and 879.4 s in order to get the right magnitude of deformation.

Running the analyses with this duration and with the correct material properties, the analysis would take extremely long time. Therefore mass scaling was applied in order to increase the critical time step,  $\Delta t_{cr}$  (Section 5.1.2), analogous to what was used on the pipe 8, 9 and 10 models (Section 5.3). A factor of  $10^6$  was used, according to the study in Section 5.3.2, such that the critical time was increased with a factor of approximately  $10^3$ .

Fracture was not expected to occur and the material was defined directly in Abaqus/CAE to save computational time. The same combined hardening model that was used on pipe 8, 9 and 10 (Section 5.3), was adopted on these models.

Interaction was defined using the general contact formulation offered in Abaqus/Explicit. This means that contact can be defined between several regions by only one definition of interaction [15]. Tangential and normal behaviour was included in the definition. The normal behaviour was defined as "hard" contact. Tangential behaviour was defined with a friction coefficient of 0.4 in order to capture the behaviour between the pipe and the support when the pipe slide on the support. A penalty formulation was chosen for both properties. The analyses were run with double precision.

## 5.4.2 Results

### Force-Displacement

The energies need to be checked for an explicit analysis, in order to determine numerical stability. Table 5.5 shows that the deviation in total energy is low relative to the internal energy. Another energy check is to look at the magnitude of artificial strain energy relative to the magnitude of internal energy (Table 5.5). For pipe M and N the magnitude of artificial strain energy is a bit high, indicating that some elements are vulnerable to hourglass modes, however the global behaviour seems reasonable. Pipe M and N are deformed quasi-statically,

## 5. Finite Element Analysis

---

**Table 5.5:** Energies for pipe M and N simulation after complete deformation.

Models	$\% \Delta E_{tot}^a$	$\% E_{AE}^b$	$\% E_K^c$
Pipe M FEA	0.5	4.8	0.0012
Pipe N FEA	0.6	3.8	0.0012

<sup>a</sup>Change in total energy relative to the magnitude of internal energy.

<sup>b</sup>Magnitude of artificial energy relative to the magnitude of internal energy.

<sup>c</sup>Magnitude of kinetic energy relative to the magnitude of internal energy.

meaning that the magnitude of kinetic energy should be at a minimum. This is fulfilled, and it is reasonable to assume that inertial forces acting on the system are negligible.

By comparison of data between the experiments and the numerical simulations, it can be seen from Figure 5.12 that there is fairly good agreement between the analyses and the experiments with regard to the force-displacement curve. The curves from the analyses lie a bit lower than the curves from the experiment. This is probably due to the fact that a material model with combined hardening has been used. In previous theses it has been concluded that using isotropic hardening gives a better representation of the force-displacement curve in the bending phase.

When pipe M and N are compared it can be seen from the curve that pipe N has a higher maximum force and generally lies higher with regard to the force response than pipe M. This is probably due to the fact that pipe N is thicker than pipe M, 3.90mm and 3.74mm respectively. The effect of the thickness on the force-displacement curve was studied in detail by Slåttedalen and Ørmen [1]. They concluded the wall thickness has a huge effect on the force response.

### Deformation

Comparison with the experiments show that both the magnitude of permanent inner deformation and N-S diameter (Table 5.6) are overestimated by the FEA. I.e. the numerical models predict more denting for less inner deformation. This error might be accounted for by multiple factors. For example by the material model, a too coarse mesh or too simple elements. Some might also be caused by inaccurate measurements of both the wall thickness and the permanent deformation of the experimental pipe. The largest magnitude of equivalent plastic strain for the most heavily deformed pipe M was seen to be higher compared to pipe N.



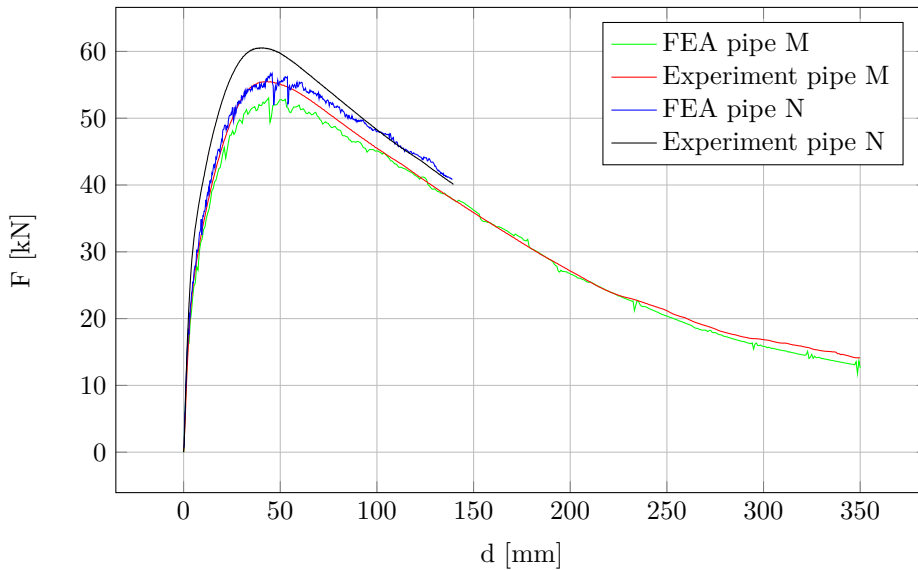


**Figure 5.12:** Force-displacement plot for quasi-static tests (M and N) compared to the numerical simulations.

**Table 5.6:** Comparison of permanent deformation and equivalent plastic strain between the experiments and FEA.

	<b>Inn. Def.<sup>a</sup></b>	<b>6 (N-S)<sup>b</sup></b>	$\varepsilon_{eq}^{p,max}$
	[mm]	[mm]	[–]
<b>Pipe M FEA</b>	373	24.15	0.7919
<b>Pipe M Experiment</b>	380	26.05	
<b>Pipe N FEA</b>	157	64.02	0.6353
<b>Pipe N Experiment</b>	161	63.91	

<sup>a</sup>Inner deformation (Figure 4.6).

<sup>b</sup>Diameter at in the North-South direction at midspan (Figure 4.6).

### Concluding Remarks

The same trend that was observed on analysis of pressurized pipe is observed in this case. The force response is underestimated, especially during the intermediate denting and bending phase. With regard to deformation the permanent inner deformation is overestimated along with a underestimation of the N-S diameter at midspan.

### 5.5 Dynamic Impact on Simply Supported Empty Pipes (Pipe K)

Slåttedalen and Ørmen [1] calibrated a Johnson-Cook fracture criterion (Equation (3.3)) and tested it on pipes dynamically impacted and subsequently stretched. When using solid, reduced integration C3D8R-elements, and a mesh consisting of four elements through the thickness, fracture was captured too late during subsequent stretching. Fracture was not found in any of their numerical models after impact only.

Aune and Hovdelien [3] tested the Cockcroft-Latham fracture criterion on a model of the pipe A experiment. The pipe was meshed with three elements through the thickness, in total 31440 fully integrated eight-noded elements using the numerical software LS-DYNA. Fracture was not found. The pipe K experiment was repeated numerically using shell elements and a modified Cockcroft-Latham criterion, but the model was not able to capture fracture after impact.

A mesh sensitivity study conducted by Slåttedalen and Ørmen showed that the global response of the pipe with regard to force-displacement was captured when using two or more C3D8R-elements through the thickness. However a high mesh sensitivity was noted locally in the impacted area of the pipe. A model with a highly refined mesh in the impacted area (36 elements through the thickness) was developed, where local mass scaling was applied in the refined area. However the numerical result was not deemed valid.

The objective of the following work is to carry out analysis of the pipe K experiment on a refined mesh and to investigate if it is possible to do this by submodeling. The study will be presented as follows: at first a presentation of the global model of the pipe K experiment, followed by results from models meshed with 3, 6 and 9 elements through the wall thickness in the impacted area. These results will be used to verify submodels meshed equivalently with 3, 6 and 9 elements through the wall thickness, driven by the global model with 3 elements through the thickness. Additionally it has been experimented if it is possible to carry out analyses on submodels with more than 9 elements through the wall thickness, based on a global model with 6 elements through the wall thickness.

At the end of this thesis it was recommended to experiment with the fully integrated, incompatible mode C3D8I-element offered in Abaqus. Results using this element will be presented after the part related to submodeling.

In light of the interesting effect of internal pressure, discussed in Section 5.3.3, the pipe K experiment was numerically repeated with 103 *bar* internal pressure to investigate the effect in case of dynamic impact. Results are presented at the end of this section.

### 5.5.1 1/4 Global Model Vs. 1/2 Global Model in Coherence with Submodelling

The displacements are transferred directly from the elements of the global model to the elements on the specified boundary of the submodel. This means that the same displacement field that was found on the global model also will be found on the respective boundaries of the submodel where displacements are being transferred. Thus the same "element-pattern" will be found on the boundaries of the submodel as on the boundaries of the global model. Figure 5.13 illustrates this. A very coarse global model (only one element through the thickness) has been used to drive a finer submodel. It can be seen that the submodel does not provide any better resolution with respect to displacements on the boundaries than what was found in the global model.

The pipe-impact problem involves two planes of symmetry which can be exploited when carrying out numerical analysis. When simulating 1/4 of the model, one plane of symmetry will be at midspan. This plane (or cross section) is in the most heavily deformed area of the pipe, and thus the area where it is of special interest to obtain better resolution with respect to displacements. For this reason, it was needed to carry out global analysis on half the pipe, to avoid transferring variables in the critical region at midspan.

Closer investigation of Figure 5.13 also reveals a linear pattern from the respective elements of the global model at both the inner- and outer surface of the submodel. This is because displacements have been specified to be transferred from the global model also to these surfaces to include the effect of the indenter. However, the outer surface is also the region of special interest when it comes to

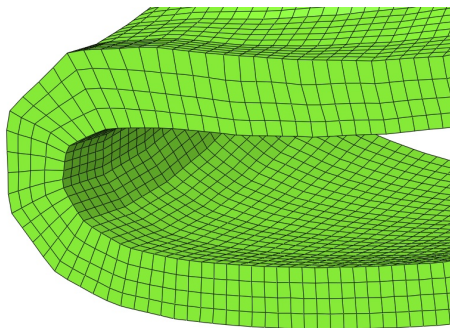


**Figure 5.13:** Example of how to not transfer variables in this particular problem, where displacements have been transferred on all surfaces from a 1/4-global model. Note the coarse linear pattern from the global model on both the outer/inner surface and the cross section.

## 5. Finite Element Analysis

---

fracture.

To avoid this problem it was decided to only transfer displacements at the "cutted" wall cross sections of the submodel. This means that the "pushing"-effect from the indenter is neglected. Equivalent to a simply supported beam where rotations are applied at both ends, the deformation at midspan depend on the length of the beam. Thus to ensure that the displacements of the submodel at midspan were equal to the displacement of the global model at midspan, the submodel was required to be very small, only 4-20 *mm* wide.

### 5.5.2 Global Model

In light of the previous discussion it was needed to develop a global model where only one plane of symmetry was exploited. A half model meshed with three elements through the thickness will from now be termed "Half 3". The global models with a refined mesh of six and nine elements through the thickness, both planes of symmetry were exploited such that only one quarter of the whole pipe were simulated. These models will from now be termed "Quarter 6" and "Quarter 9". Additionally a quarter model with 3 elements through the thickness were simulated, to verify the use of the symmetry plane at midspan, from now termed "Quarter 3". Dimensions of the pipe were set according to Pipe K (Table 4.2).

All the analyses were run with double precision, and with full precision on the nodal outputs.

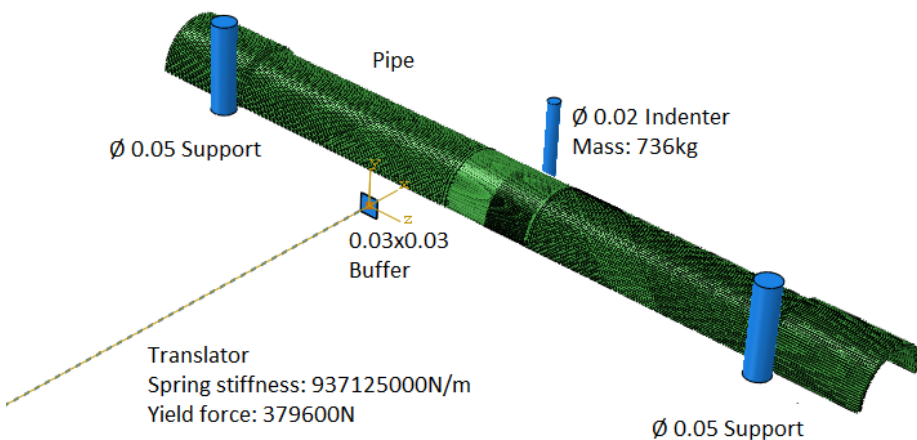


**Figure 5.14:** Half Model of pipe K. Measurements without units are given in meters.

### Numerical Model

Figure 5.14 displays the setup of the global half model. The pipe is simply supported using two supports modeled as cylinders with diameter equal to 0.05  $m$  and length of 0.15  $m$ . The trolley, which hits the pipe, is made as a rigid cylinder with radius equal to 0.1  $m$  equal to the nose tip radius of the indenter used in the experiments. The initial velocity is set to 5.18  $m/s$  according to the Pipe K experiment.

**Modeling of the Buffer.** The kicking machine, in which the experiment was conducted, is equipped with buffers made of eight square aluminum columns (80x80  $mm^2$ , 3.5  $mm$  thick, 320  $mm$  long) to stop the trolley in case not all the kinetic energy is absorbed by the pipe during impact. With regard to the Pipe K experiment the trolley impacted the buffers with a velocity of 2.55  $m/s$  and caused the buffers to compress 6-8  $mm$ . When the trolley finally was stopped, elastic energy stored in both the pipe and the buffer cause the trolley to bounce back in the opposite direction.

It is believed that fracture occurs during this face of spring back, thus it was assumed important to also include the effect of the buffer in the numerical model. It was for example observed that permanent inner deformation of the pipe increased with approximately 10  $mm$  (toward what was measured in the lab) when the buffer was changed from being rigidly constrained in all directions.

The aluminum columns were observed to deform both elastically and plastically when impacted by the trolley. The indenter was decelerated from approximately 2.55  $m/s$  to 0  $m/s$ , and then sent back again due to elastic forces stored in the buffer and the pipe. To model this behaviour the buffer is assumed to behave linear elastic and perfectly plastic (Figure 5.15). The spring stiffness,  $k$ , was calculated to be  $1.874 \cdot 10^9 N/m$  for the whole model, based on the cross sectional area of the eight rectangles and the Youngs modulus of aluminum (70 000  $MPa$ )<sup>7</sup>.  $k$  is set equal to  $0.937 \cdot 10^9 N/m$  and  $0.469 \cdot 10^9 N/m$  for the half and the quarter pipe, respectively.

The yield force,  $F_{avg}^{buffer}$ , was taken as the average buckling stiffness. The average buckling stiffness of one rectangular column can be calculated as

$$F_{avg}^{buffer} = \kappa \sigma_0 t^2 (b/t)^{1/3}. \quad (5.6)$$

Here  $\kappa$  is a dimensionless constant with value 13.06,  $\sigma_0$  is the yield stress (209  $MPa$ ), and  $t$  and  $b$  is the thickness and the width of the crash-box, respectively. The calculated average buckling stiffness of one column was found to be 94.9  $kN$ . The yield force used for the half and quarter model was thus set to  $94.9 * 4 = 379.6 kN$  and  $94.9 * 2 = 189.8 kN$ , respectively.

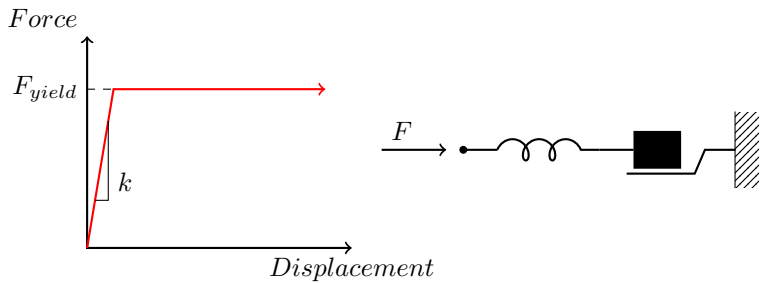
The buffer was modeled as a rigid square with each side equal to 0.03 meter. In

---

<sup>7</sup> $k_{tot} = 8k = 8 \frac{EA}{L} = 8 \frac{70000 * (80^2 - (80 - 2 * 3.5)^2)}{320} = 1.874 \cdot 10^6 N/mm = 1.874 \cdot 10^9 N/m.$

## 5. Finite Element Analysis

---



(a) Linear elastic - perfect plastic behavior.

(b) Rheological model.

**Figure 5.15:** Buffer model.

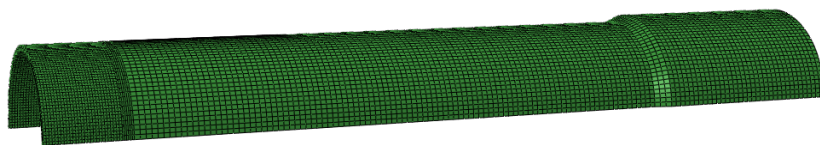
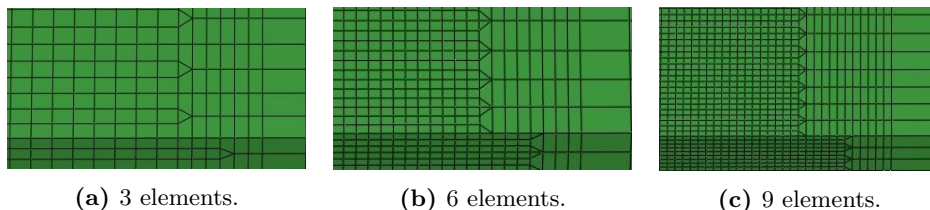
order to satisfy the deformation, a translator was attached to the rigid square, and given the stiffness and the yield force just calculated.

**Material.** The material was defined using SMM with the properties given in Table 5.2. The indenter was given mass equal to 736 *kg* and 368 *kg* for the half and the quarter models, respectively, corresponding to the mass of the impact trolley used in the experiment (1472 *kg*). The rigid buffer was given a small mass of 2 *kg* to avoid instabilities.

**Time.** The duration of the simulation was set to 0.23 *s* although the indenter hit the buffer after 0.11 *s*. The additional time of 0.12 *s* is included to capture the full spring back of the pipe. I.e the additional time is not necessary if one only is searching for the force-response of the pipe.

**Interaction.** A general contact interaction is defined between relevant surfaces (pipe-indenter, indenter-buffer and pipe-support), with both tangential and normal behaviour. The tangential friction coefficient is set equal to 0.4, with a penalty friction formulation. "Hard" contact is chosen for the normal behaviour.

**Mesh.** It was found difficult to obtain proper mesh transitions when using Abaqus/CAE. The pipes were instead meshed using the open software SALOME. A mesh transition was placed approximately 55 *mm* from midspan on all models, with a transition width of approximately 9 *mm* (Figure 5.16). Two elements through the thickness were used on the coarse part on Half 3, Quarter 3 and Quarter 6, while three were used on Quarter 9. The applied element transitions are illustrated in Figure 5.17. Half 3/Quarter 3, Quarter 6 and Quarter 9 were defined with 90, 180 and 270 elements in the circumferential direction, giving a total 49800/24900, 77760 and 242730 elements, respectively. Linear eight noded, solid elements with reduced integration (C3D8R) were used on all models to save computational costs.

**Figure 5.16:** Quarter 3.**Figure 5.17:** Different mesh transitions applied on models with three, six and nine elements through the thickness at midspan.

## Results

Table 5.7 shows how the total energy was observed to deviate from equilibrium. A deviation below 1%, relative to the internal energy, were observed on the quasi-static analyses on empty and pressurized pipes. A deviation between 2 and 22 % is observed in this case of dynamic impact with the material defined using SMM. Such a large deviation indicate numerical instability. However, when comparing force-displacement and permanent deformation with the experimental values, it is observed that the numerical results coincide quite well. Even though Half 3 and Quarter 3 yielded a total energy deviation of 2% and 22.4%, respectively, the force-displacement, magnitude of deformation and plastic deformation coincide between the two analyses. Based on this, it was decided to ignore the just

**Table 5.7:** Energy check of different global models.

Models	$\% \Delta E_{tot}^a$	$\% E_{AE}^b$
Half 3	2.0	2.0
Quarter 3	22.4	1.6
Quarter 6	11.8	0.9
Quarter 9	6.8	0.6

<sup>a</sup>Magnitude of change in Total energy relative to the magnitude of internal energy.

<sup>b</sup>Magnitude of artificial energy relative to the magnitude of internal energy.

## 5. Finite Element Analysis

---

mentioned energy unbalance. The unbalance is probably caused by some error related to the implementation of SMM.

The magnitude of artificial strain energy, relative to the magnitude of energy dissipated through plasticity, is seen to vary between 2.8 and 0.8 %, decreasing with mesh refinement. This indicates that hourglass control is being triggered to prevent hourglass modes. Close investigation of the analyses revealed hourglass modes that occurred in the impacted zone of the pipe. These modes did not disappear with mesh refinement, illustrated in Figure 5.18.

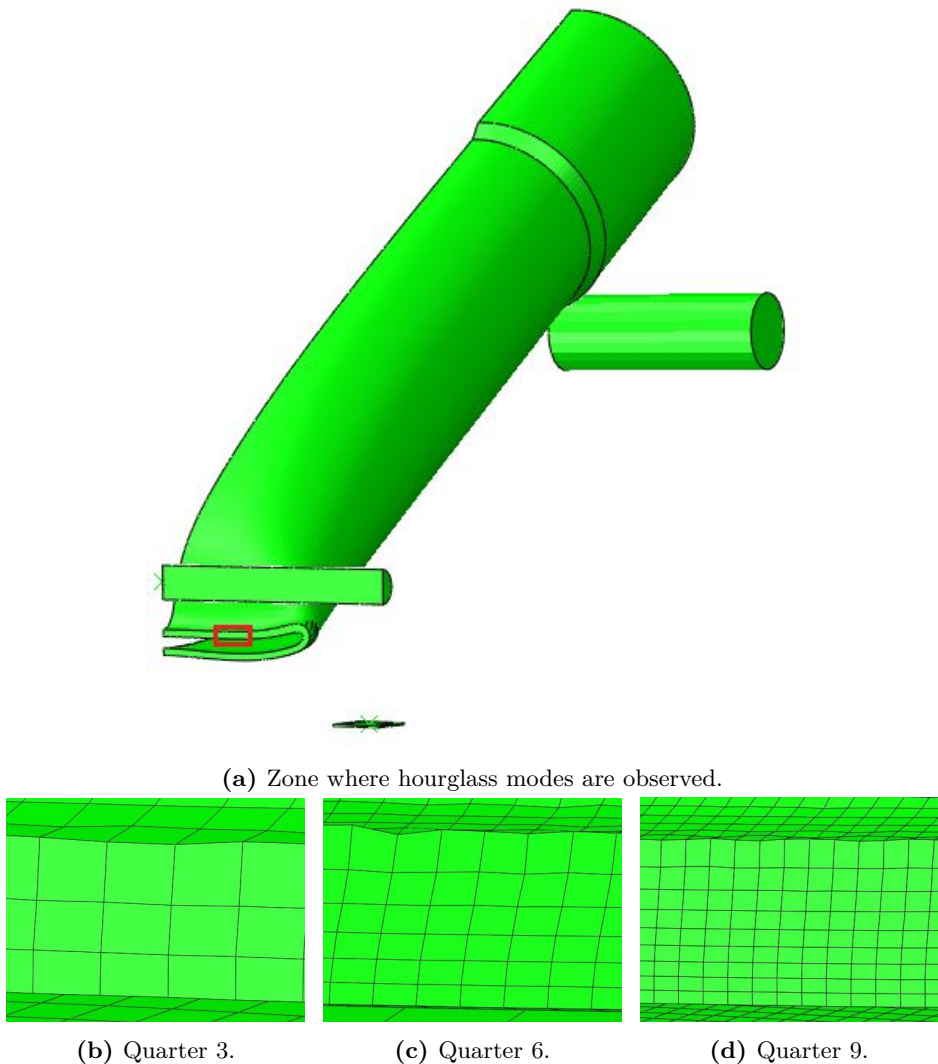


**Figure 5.18:** Hourglass modes observed in the impacted zone for different element sizes.



### Force-Displacement

The obtained force-displacement curves are shown in Figure 5.19. The same general trends that were observed in the quasi-static experiments are observed in these simulations. The force-response in the intermediate phase is a bit underestimated compared to experimental results. This is probably due to the combined hardening definition, better results have been reported using isotropic hardening only [1]. Additionally, inaccuracy in the wall thickness measurement of the experimental pipe should be taken into account.

**Half 3 vs. Quarter 3.** No significant differences are noted on the force-response when comparing Half 3 and Quarter 3. The average force response is calculated to 35.65 and 35.61  $kN$  for Half 3 and Quarter 3, respectively.

**Mesh Refinement.** No significant differences are observed with a mesh refinement higher than 3 elements through the thickness. The average force<sup>8</sup> response is calculated to 39.28, 40.10 and 41.18  $kN$  for Quarter 3, Quarter 6 and Quarter 9, respectively. The average force of the experiment is calculated to 40.34  $kN$ . I.e. the force response is well captured using 3 elements through the thickness and C3D8R-elements.

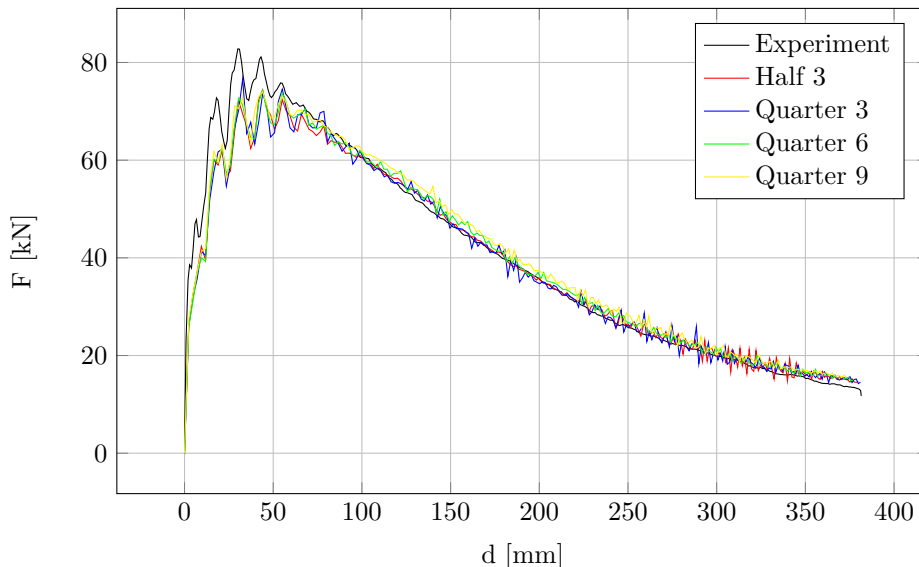


**Figure 5.19:** Comparison of force-displacement for increasing number of elements through the thickness.

<sup>8</sup>The average force is calculated as the force-displacement integral divided on the indenter position when impacting the buffer.

**Deformation**

A comparison of the permanent deformation after complete loading is given in Table 5.8. Here the magnitude of inner deformation and diameter in N-S direction at midspan, according to Figure 4.6, is compared between the different models and the experiment. It should be kept in mind that the experimental measured values are a bit inaccurate. The numerical models are generally seen to have a too small magnitude of permanent inner deformation, and too much reduction in N-S diameter at midspan. The magnitude of inner deformation was observed to be sensitive to the last phase of deformation when the indenter hit the buffer, and the modeling of this phase is no more than an approximation.

**Table 5.8:** Comparison of permanent inner deformation and N-S diameter at midspan (point 6, Figure 4.6).

	Inn. Def. <sup>a</sup>	6 (N-S) <sup>b</sup>	$\varepsilon_{eq}^{p,max}$
	[mm]	[mm]	[–]
<b>Experiment</b>	403	27.02	
<b>Half 3</b>	387	22.23	0.806
<b>Quarter 3</b>	387	22.24	0.804
<b>Quarter 6</b>	390	22.53	1.070
<b>Quarter 9</b>	392	22.54	1.108

<sup>a</sup>Inner deformation (Figure 4.6).

<sup>b</sup>Diameter at in the North-South direction at midspan (Figure 4.6).

**Half 3 vs. Quarter 3.** No significant differences are noted on neither inner deformation nor N-S diameter at midspan. A comparison of the magnitude of equivalent plastic strain on the surface of Half 3 and Quarter 3 in the most deformed area (Figure 5.20) is given in Figure 5.21. A 0.2% deviation on the maximum magnitude of equivalent plastic strain is noted between the two models.

**Mesh Refinement.** The magnitude of permanent inner deformation is observed to approach the experimental measured value when increasing the number of elements. However, a deviation of 2.8% (11 mm) is still noted on the model with nine elements through the wall thickness. The N-S diameter at midspan is seen to converge at approximately 22 mm, 18% less than the experimental measured diameter.

In Figure 5.22 the magnitude of equivalent plastic strain is plotted against deformation of the respective critical element of Quarter 3, Quarter 6 and Quarter

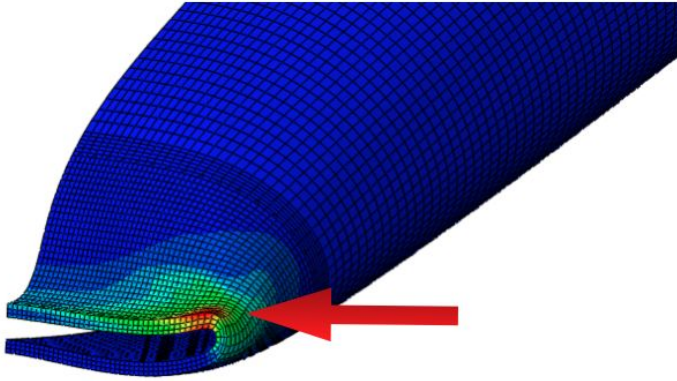


Figure 5.20: The most plastically deformed zone.

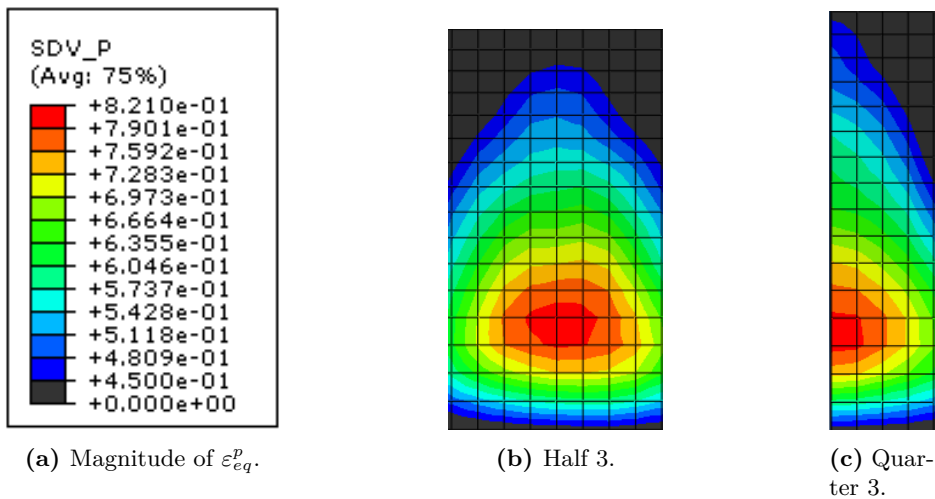
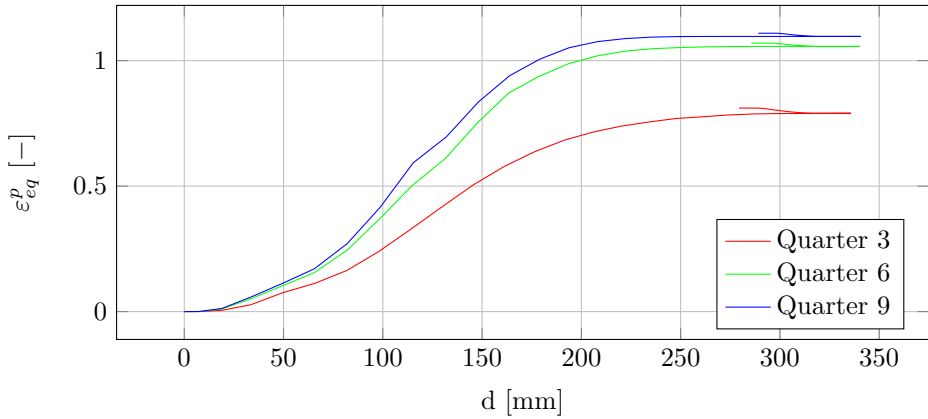


Figure 5.21: Comparison of the magnitude of equivalent plastic strain on the surface of Half 3 and Quarter 3, in the most plastically deformed zone (Figure 5.20).

9 in indenter direction. A rather large increase in maximum equivalent plastic strain is observed when the mesh is refined: from 0.81 to 1.11 when the number of elements through the thickness is increased from three to nine. It is not possible to determine if the magnitude of equivalent plastic strain has converged or not, however it is noted that the difference between six and nine elements through the thickness is rather small: 0.27 difference between three and six, 0.04 difference

## 5. Finite Element Analysis



**Figure 5.22:** Comparison of  $\varepsilon_{eq}^p$  - displacement for the element with the highest magnitude of final equivalent plastic strain.

between six and nine.

Based on metallurgical investigations (Section 3.2), it is seen that the area with the highest magnitude of plastic deformation coincides well with where fracture occurs. Figure 5.23 compares the evolution of the damage parameter,  $D$ ,

$$D = \frac{\int \max(\sigma_1, 0) d\varepsilon_{eq}^p}{W_{cr}}, \quad (5.7)$$

in the element with the highest magnitude of equivalent plastic strain between the different meshes. The damage parameter is plotted against displacement in the indenter direction of the respective element. It is seen that the criterion is far from predicting fracture ( $D=1$ ), even with nine elements through the thickness. It is not possible to determine if this parameter has converged. It is also noted that according to this criterion, the most damaged zone is on the inside of the pipe wall, where  $D$  is equal to 0.32 at the highest (Figure 5.24).

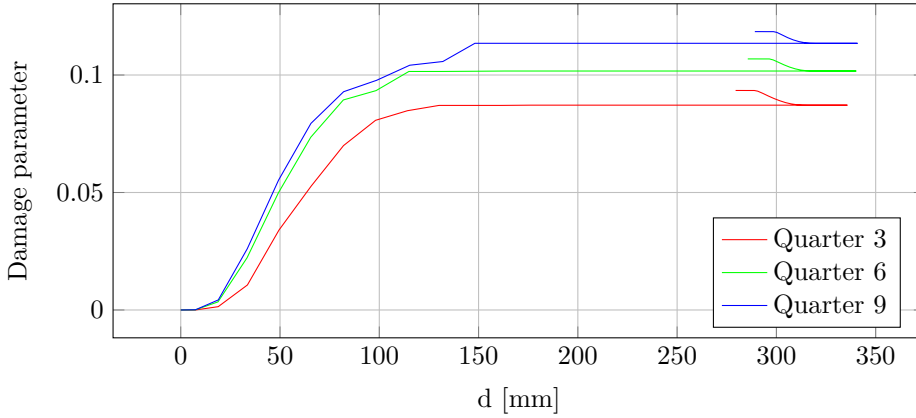


**Figure 5.23:** Comparison of damage - displacement curves for the element with the highest magnitude of equivalent plastic strain after complete loading.

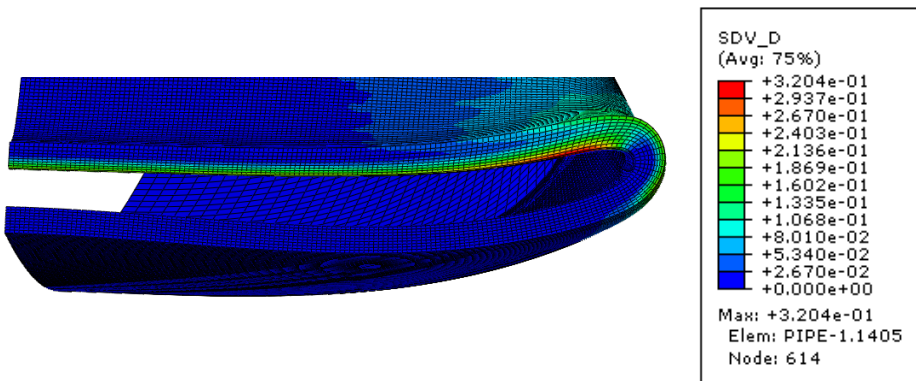


**Figure 5.24:** Contour plot of the damage parameter on the model with nine elements through the thickness.

### Computational Costs

Table 5.9 shows that the CPU-time increase rapidly when decreasing the element size. The CPU-time for the quarter model with 6 elements through the wall thickness is over 7 times larger than the quarter model with 3 elements. This rapid increase is due to a combination of a decreased critical time step and an increased number of elements. The quarter model with 9 elements over the thickness used 50 hours and 7 minutes on NTNU's super computer, "Vilje", with use of 32 CPUs. The analysis was first started on the cluster "Snurre" with use of 8 CPUs in order to estimate the time needed for comparison.

**Table 5.9:** Comparison of the computational cost of carrying out the different analyses.

	Number of Elements	CPU-time <sup>a</sup> [h : min]
<b>Half 3</b>	49800	09 : 35
<b>Quarter 3</b>	24900	04 : 46
<b>Quarter 6</b>	77760	35 : 35
<b>Quarter 9</b>	242730	190 : 00 <sup>b</sup>

<sup>a</sup>Total CPU usage of the simulation, given in hours:minutes with 8 CPUs. Run on the cluster "Snurre".

<sup>b</sup>Estimated time when started on 8 CPUs. 32 CPUs were in fact used on this analysis.

### Concluding Remarks

Comparison between exploiting one plane of symmetry and two, does not show any significant differences with regard to either force response or magnitude of plastic deformation locally in the dent. To exploit both planes of symmetry and only model one quarter of the pipe is, based on these results, concluded to be a valid simplification.

Comparison of the force response on models with refined meshes, with 3, 6 and 9 elements through the thickness, reveals that the force response of the pipe is well captured when using 3 elements through the thickness and C3D8R-elements.

It is not possible to determine if the magnitude of equivalent plastic strain locally in the dent has converged when using 9 elements through the wall thickness. The same applies for the measure "permanent inner deformation", convergence is not

seen when increasing from 3 to 9 elements through the thickness.

The damage parameter according to the Cockcroft-Latham criterion is far from predicting fracture and the most damaged area is according to this criterion on the inside of pipe.

### 5.5.3 Submodeling

In this section it will be investigated if it is possible to utilize submodel analysis in the most plastically deformed area of the pipe. Displacements will be transferred from the "Half 3" model, to submodels with the same element type and size as Half 3/Quarter 3, Quarter 6 and Quarter 9 to compare if the same results are obtained. At first a verification of the submodel width is made, to verify the simplification made when neglecting the indenter and only transferring variables at the cross sectional sides of the submodel. All submodel analyses are carried out using Abaqus/Explicit without mass- or time scaling.

#### Submodel

Only elastic strains are observed to occur on the underside of the pipe (Figure 5.20), therefore only  $105^\circ$  (from the top where the indenter hit) of the cross section is modeled (Figure 5.25). The translational DOFs: 1, 2 and 3 (rotational DOFs not active when using C3D8R-elements), according to a general 3D cartesian coordinate system is transferred on all sides except at the top and underside.

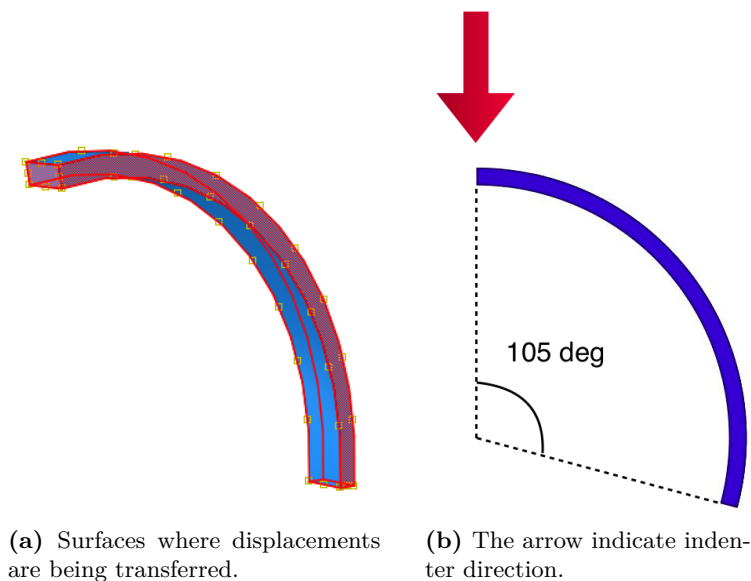


**Figure 5.25:** Submodel configuration.

### Results

**Width Verification.** The width verification is conducted on submodels with 2, 4 and 8 elements across the width. These models will from now be termed Sub 2, Sub 4 and Sub 8. All three models were meshed with the same element size as used in the dented zone of Half 3, in total 312, 624 and 1248 elements, respectively. The width of each submodel is correspondingly  $4.1mm$ ,  $8.2mm$  and  $16.3mm$ .

The analyses Sub 2, Sub 4 and Sub 8 were run with double precision on eight CPUs and needed in total 0:07, 0:10 and 0:18 to complete (hour:min). A check of the energy balance of the respective analyses proved small values for both  $\% \Delta E_{tot}$ <sup>9</sup> and  $\% E_{AE}$ <sup>10</sup>, 0.2-0.6 and 1.3-1.9, respectively.

A comparison of deformation between the global model and the submodel should always be made when carrying out submodel analysis by making an overlay plot [15]. As can be seen in Figure 5.26, displacement of Sub 2, Sub 4 and Sub 8 seem to coincide with the global model, Half 3.

A comparison of how the equivalent plastic strain is "distributed" on the outer surface in the most plastically deformed zone (Figure 5.20) is presented in Figure 5.27. It is seen that maximum value of equivalent plastic strain is found on Sub 8 and that Sub 2 is in best agreement with the global model, however the differences are generally small and it seems that the assumption to not transfer displacements at the top- and underside is valid.

Based on these results the best choice would be to use the width of Sub 2 as basis for the following analyses with refined meshes. However as shown in Figure 5.18, what seem to be hourglass modes is present in the global model. It was observed that these modes were transferred to the critical region at midspan of the submodel when using the smallest width. Thus to avoid this transfer of non-realistic deformation, it was decided to use the width of Sub 4,  $8.148mm$ , as basis for the refined analyses.

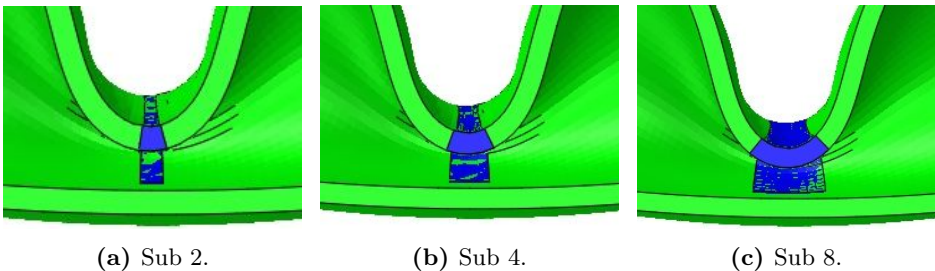


**Figure 5.26:** Overlay plot with the global modal Half 3.

---

<sup>9</sup>magnitude of change in Total energy relative to the magnitude of internal energy.

<sup>10</sup>magnitude of artificial energy relative to the magnitude of internal energy.



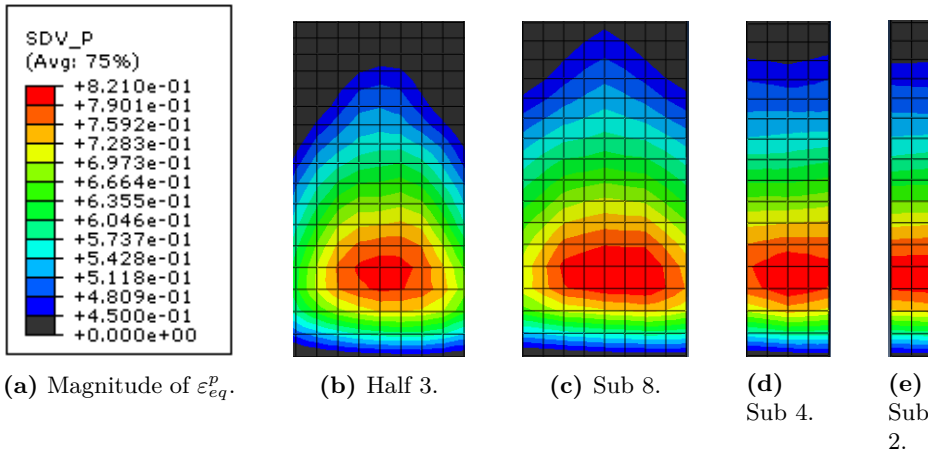


**Figure 5.27:** Comparison of equivalent plastic strain on the surface in the most plastically deformed zone. The width of a single element is  $2.037\text{mm}$ . Maximum equivalent plastic strain was 0.806, 0.821, 0.818 and 0.807 in Half 3, Sub 8, Sub 4 and Sub 2, respectively.

**Mesh Refinement.** Based on the width of Sub 4 new submodels meshed with the same element size as Quarter 6 and Quarter 9 were developed, from now termed Sub t6 and Sub t9. These submodels consisted of 4992 and 16848 elements, respectively. Both submodels were driven by the Half 3 global model, and results were compared with the global models Quarter 6 and Quarter 9. The energies,  $\% \Delta E_{tot}$  and  $\% E_{AE}$ , was found to be in the same range, but a small reduction on both parameter was noted compared to Sub 4.

It has already been shown how the magnitude of equivalent plastic strain in the submodel with three elements through the thickness is in good agreement with the global model with the same element size. Figure 5.28 and Figure 5.29 show the differences in equivalent plastic strain between submodels and corresponding global models.

A deviation is observed between the submodels and the corresponding global models on the magnitude of equivalent plastic strain. The deviation at maximum between Sub t6 - Quarter 6 and Sub t9 - Quarter 9 is 0.13 and 0.11, respectively. Even though the refined submodels do not provide the same results as their corresponding global models the general distribution of equivalent plastic strain is the same. It is also seen that the magnitude of equivalent plastic strain increases with mesh refinement of the submodels.

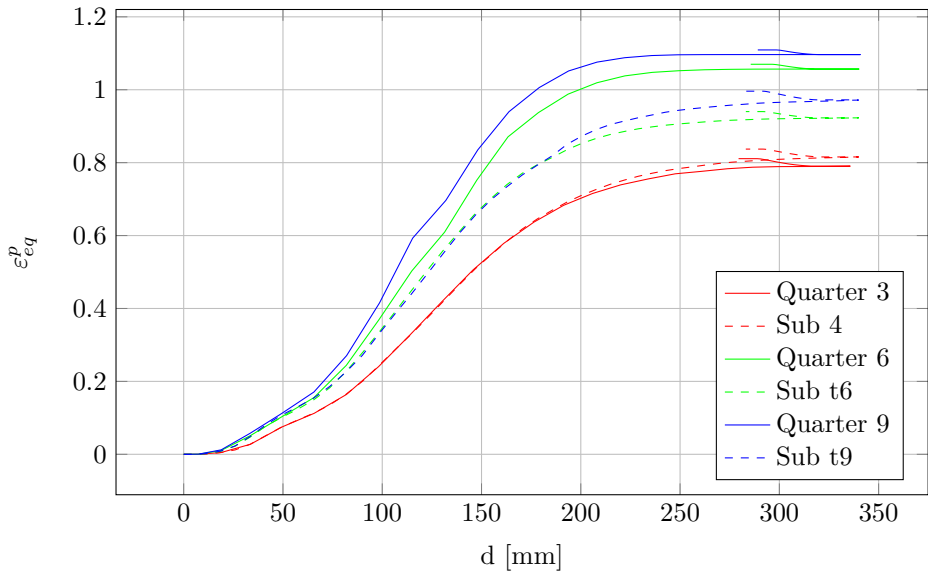


**Figure 5.28:** Equivalent plastic strain-displacement plot for the critical element from the different quarter models and corresponding submodels.

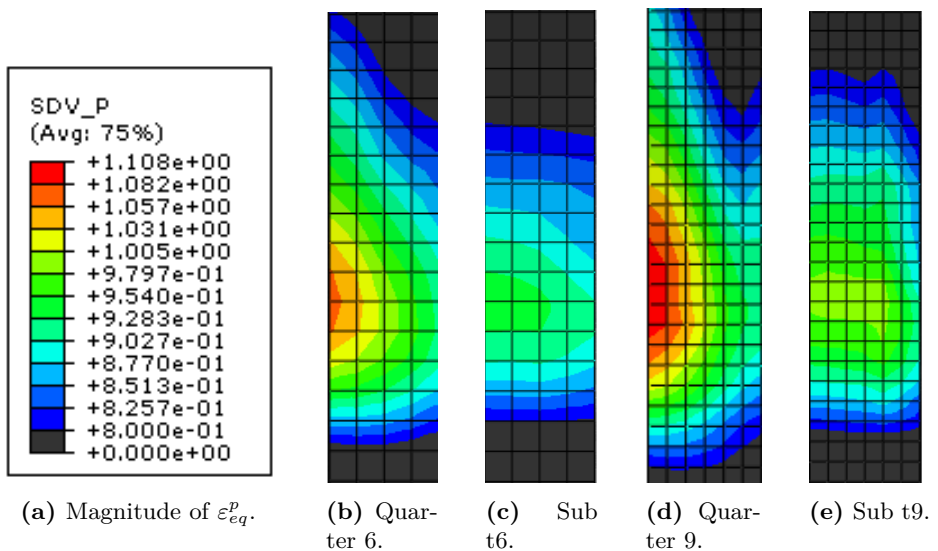


**Figure 5.29:** Contour plot of the equivalent plastic strain in most deformed zone. Maximum equivalent plastic strain was 1.07, 0.94, 1.11 and 1.00 in Quarter 6, Sub t6, Quarter 9 and Sub t9, respectively.

The reason why the submodels deviate from the corresponding global models is probably explained by the fact that the global model Half 3 not has converged on the magnitude of deformation locally in the dent. I.e. a non-converged displacement field is transferred to the submodels. Figure 5.30 illustrates how the deformation of Sub t9 is bounded by the deformation of Half 3, when compared with the deformation of Quarter 9.

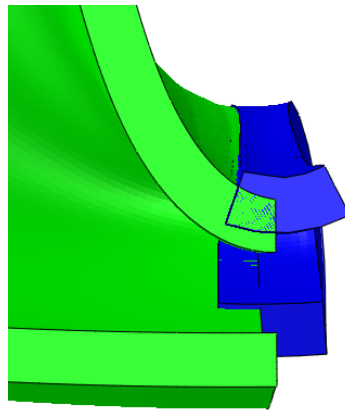


**Figure 5.30:** Overlay plot of Sub t9 (blue) and Quarter 9 (green) after complete deformation. Keep in mind that Sub t9 is driven by Half 3.

### Computational Costs

Table 5.10 tabulates the CPU usage when carrying out submodel analysis on 8 CPUs. Since analyses are carried out using explicit time integration, the same trend that was observed regarding the global analyses is observed in this case as well: an exponential increase in CPU time with element refinement. Even though the submodel is quite small in size, the analysis become rather expensive when the elements are refined. However carrying out submodel analysis is a lot more effective compared to global analysis.

## 5. Finite Element Analysis

---

**Table 5.10:** Comparison of the CPU-usage between submodels and global models with the same element size.

	Submodel <sup>a</sup>	Total <sup>b</sup>	Global Model <sup>c</sup>
	[ <i>h</i> : <i>min</i> ]	[ <i>h</i> : <i>min</i> ]	[ <i>h</i> : <i>min</i> ]
<b>Sub t6</b>	02 : 49	12 : 24	35 : 35
<b>Sub t9</b>	12 : 29	22 : 04	190 : 00 <sup>d</sup>

<sup>a</sup>Total CPU-time of the simulation, given in hours:minutes when carried out on 8 CPUs.

<sup>b</sup>Total time of both the submodel and the global model used to drive the submodel (Half 3).

<sup>c</sup>Time of the corresponding global model with the same element size at midspan.

<sup>d</sup>Estimated time when started on 8 CPUs. 32 CPUs were in fact used on this analysis.

### Concluding Remarks

It is observed that submodeling can be a lot more computationally effective compared to global analysis and the transfer of displacements from the global model to the submodel seem to valid. The submodel deforms as it should. However refined submodels will be bounded by the deformations obtained from the global model. Thus a refined submodel, driven by a non-converged global model, will not provide the same solution as global model with the same refined element size.

It is shown that a submodel approximately provides the same strain field as the global model when both models have the same element size.

### 5.5.4 Refined Submodel Analysis

The global analysis with nine elements through the thickness did not give convergence on maximum equivalent plastic strain when using C3D8R-elements. To carry out global analyses with more than nine elements through the thickness was regarded as too extensive. So a study was conducted to investigate if it was possible to carry out submodel analysis with more than nine elements through the thickness. A global half model analysis with 6 elements through the thickness at midspan was carried out (from now termed Half 6), which solution was used to drive the following refined submodels.

#### Submodel

To save computational costs, it was attempted to use a smaller submodel than the ones previously discussed in Section 5.5.3. The submodel included 55° of the pipe wall in the most plastically deformed zone, illustrated in Figure 5.31.

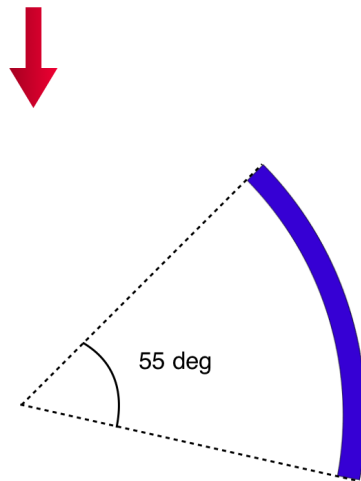


**Figure 5.31:** Submodel size. Arrow indicate indenter direction.

**Verification of the Submodel.** Two submodel analyses on submodels with width equal to 2 and 5 *mm* and meshed with the same element size as the global model were carried out to verify that displacements are transferred correctly. The two models will from now be termed rSub 2 and rSub 5. Figure 5.32 illustrates the final deformed configuration of the respective submodels and comparison with the global model showed good agreement.

The distribution of equivalent plastic strain in the most deformed zone is illustrated in Figure 5.33. Both submodels are in good agreement with the global model, but a small underestimation of the maximum magnitude is noted.

Both submodels seem to provide the same strain field as the global model and are thus deemed valid. To save computational costs, it was decided to use the smallest submodel, rSub 2, as basis for mesh refinement.

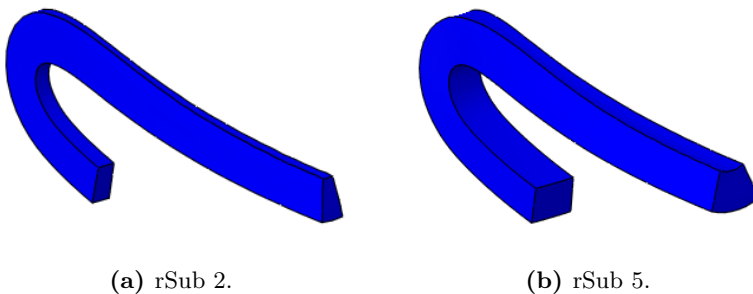


**Figure 5.32:** Final deformed configuration.

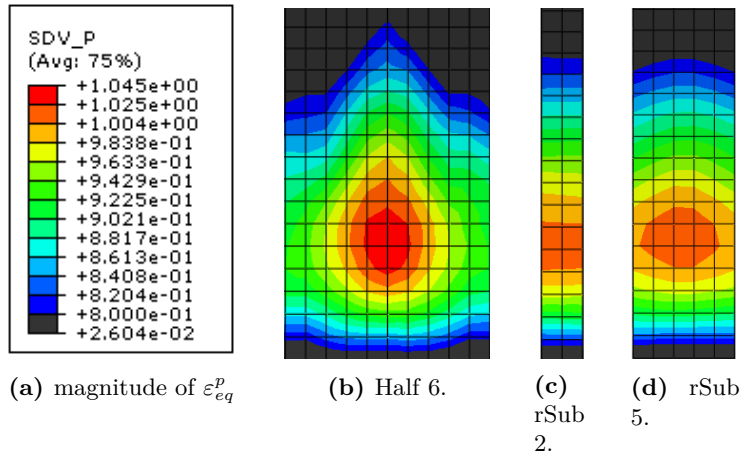


**Figure 5.33:** Comparison of equivalent plastic strain on the surface in the most plastically deformed zone between global model and submodels. Maximum equivalent plastic strain was 1.045, 1.015 and 1.016 on Half 6, rSub2 and rSub5, respectively.

### Mesh Refinement

**rSub 2.** Strange things started to occur when the mesh was refined. When increasing from 6 to 7 elements through the thickness, the submodel still deformed as it should, however artificial stresses appeared in the submodel. The effect of these artificial stresses is best illustrated by comparing the difference in accumulated damage according to the Cockcroft-Latham criterion between two submodels with 6 and 7 elements through the thickness (Figure 5.35). This effect was even more evident when refining the mesh even further. Figure 5.34 illustrates the final deformed configuration of a submodel meshed with 21 elements through the thickness. 10% of the elements in the submodel have been eroded at what seem to be random places. In light of the seemingly good results on refined submodels presented in Section 5.5.3, this was a bit surprising.

A lot of what seem to be hourglass modes were observed in the impacted zone of the global model (Figure 5.36), it is believed that the artificial stresses observed in the submodel are linked to these modes and that the effect become more evident when the mesh refined. When the submodel only is 2 mm wide it is assumed that the transferred hourglass modes will dominate the entire submodel solution and based on this assumption it was investigated if it was possible to carry out mesh refinement on the 5 mm wide submodel instead (rSub 5).

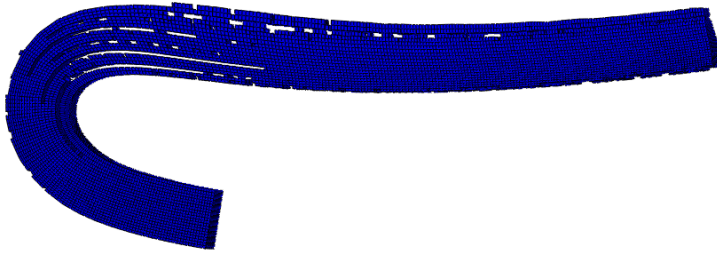


**Figure 5.34:** The deformed submodel with 21 elements over the thickness

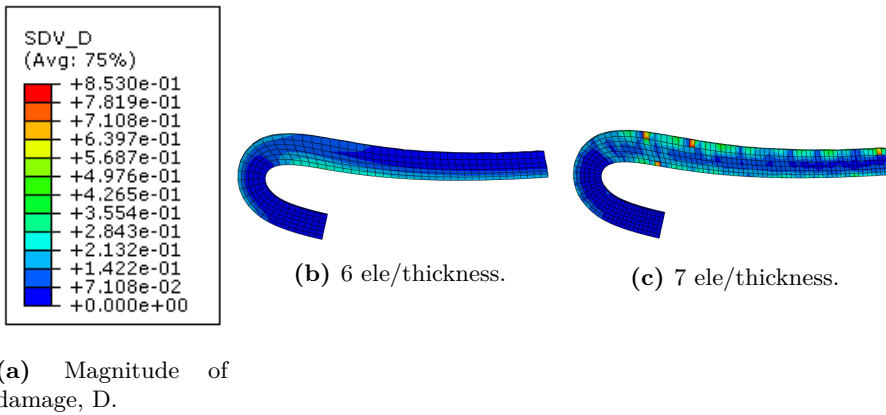


**Figure 5.35:** Comparison of the distribution of damage between submodels based on rSub 2 with 6 and 7 elements through the thickness.

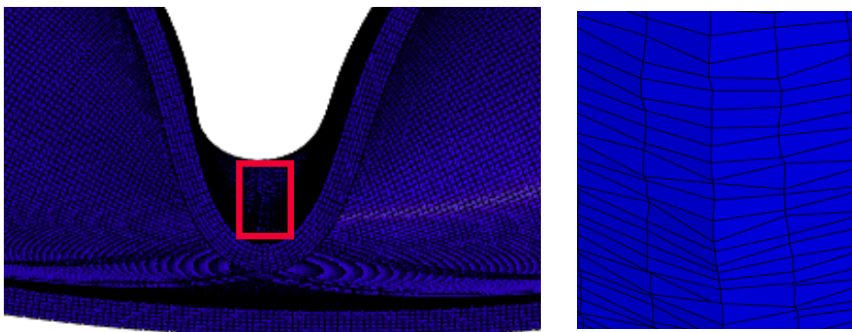


**Figure 5.36:** What seem to be hourglass modes observed in the global model.

## 5. Finite Element Analysis

---

**rSub 5.** Contrary to rSub 2, no artificial stresses were observed on rSub 5 when meshed with 7 and 10 elements through the thickness, a small increase in the maximum equivalent plastic strain was detected, but no convergence. Thus it was decided to carry out a submodel analysis with 21 elements through the wall thickness. The model consisted of approximately 300 000 elements, and due to the reduction of the critical time step, the total time for completing the analysis was estimated to be over a month with use of 8 CPUs. Due to this the time period of the submodel analysis was scaled by four (time scaling and mass scaling will be discussed later). This reduced the estimated time to complete the analysis to approximately 13 days. The analysis was started, but after 10 days the analysis was aborted due to storage capacity problems on the cluster. Sadly the .odb-file was corrupted and no results were therefore available for analysis.

**35 ° Submodel** It is clear that due to the critical time step of explicit analysis, also submodeling become computationally expensive when the mesh is refined. To save computational costs a smaller submodel was developed, only consisting of 35° of the most deformed area (Figure 5.37), however the width of 5 mm was maintained.

The model was meshed with 12 elements through the thickness, in total 18 000 elements and it needed 30 hours to complete on 8 CPUs without any scaling. Some artificial stresses were observed, and some strange modes of deformation were observed in some areas on the surfaces where displacements were transferred. Figure 5.38 illustrates how a row of elements in the transfer zone was observed to be twisted (this was not observed on the other side of the submodel). The analysis was thus not deemed valid.

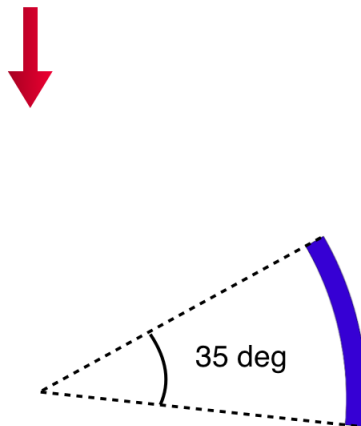


**Figure 5.37:** 35° submodel. The arrow indicates indenter direction.



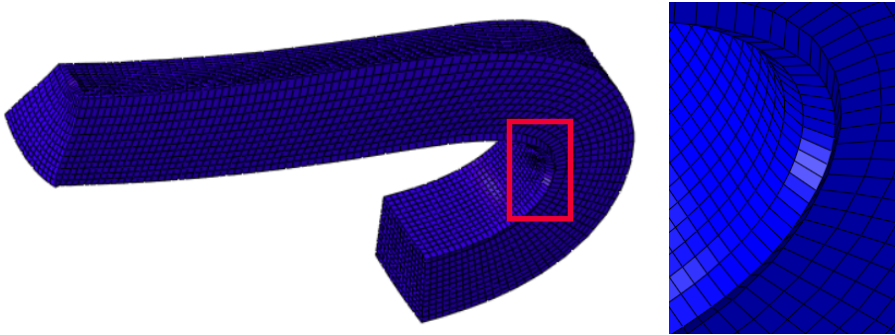


**Figure 5.38:** Twisted elements observed on the 35°-submodel.

### Scaling

It was assumed that when the global deformation of the pipe was captured by the global model it would be appropriate to apply scaling to the submodel to save computational costs. It was therefore of interest to attempt either mass- or time scaling of the submodel.

**Mass Scaling** Since strain rate sensitivity is included in the material model, the most obvious choice is to apply mass scaling on the submodel. A scaling of  $10^6$  and  $10^3$  were applied on rSub 5, meshed with 21 elements through the thickness. The scaling did indeed decrease the computational time, but post-processing of the results revealed that the model scaled with  $10^6$  did not deform at all. The model was observed to vibrate in its "undeformed" configuration. When the density was scaled with  $10^3$ , the submodel deformed, but a lot of artificial stresses were observed during the analysis. These stresses caused a lot of elements to be eroded in what seem to be random places, illustrated in Figure 5.39. It was also attempted to use  $10^2$  and 10, but tendencies of artificial stresses were observed in these cases as well.

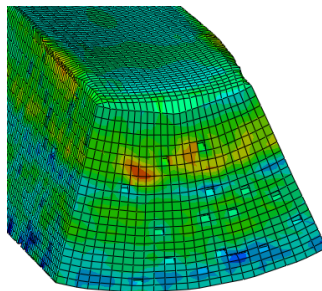


**Figure 5.39:** Eroded elements observed when the density is scaled by  $10^3$ . The contours illustrate the magnitude of  $\sigma_{eq}$ .

**Time Scaling** It was also investigated if time scaling would provide better results than mass scaling. Time scaling by 400 gave the same result as mass scaling by  $10^6$ : the submodel was only observed to vibrate in its "undeformed" configuration. The model did deform when time scaling by 40 was applied, but artificial stresses were observed, causing elements to be eroded (Figure 5.40). Scaling by 4 does however seem to provide decent results, but the required computational time is still rather large for refined submodels.

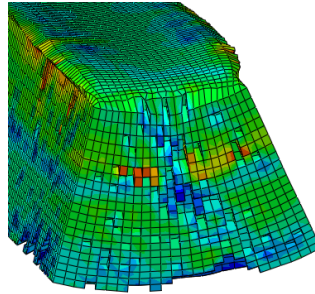


**Figure 5.40:** Eroded elements observed with time scaled by 40. The contours illustrate the magnitude of  $\sigma_{eq}$ .

### Concluding Remarks

Artificial stresses and twisted elements were observed to occur in the submodel when it was made to small. These effects are believed to be linked with the hourglass modes observed in the global model. I.e. these effects might disappear if a submodel is driven by a global model without hourglass modes.

Due to the critical time step, the submodel analyses require a huge number of time increments to complete. I.e. the required computational effort becomes extremely high even if the total number of elements in the submodel is low. Since neither mass scaling nor time scaling of the submodel seem to work, this way of analysis is judged as a dead end when applied on such a problem. Especially when taking into account that strains obtained in the submodel, in either case will be bounded by the displacements obtained from the global model (Figure 5.30).

### 5.5.5 Change of Yield Surface

As mentioned in Section 5.2.1, a slightly narrowed yield surface has been adopted when using SMM: Hershey surface with  $m=6$  (Section 2.3.1). It was therefore of interest to compare results between the Hershey surface and the von Mises surface used in the previous theses. Two analyses were carried out on a relatively coarse model of the Pipe K experiment consisting of three elements across the thickness. However a rigid buffer was used in these two experiments, i.e. results

should not be compared with the other Pipe K results presented where an elastic-plastic buffer was used.

Contour plots of the equivalent plastic strain in the most deformed zone (Figure 5.20) is presented in Figure 5.41. As can be seen no significant differences are observed between the two models with respect to equivalent plastic strain. This suggests that changing the yielding surface has little effect in this case.

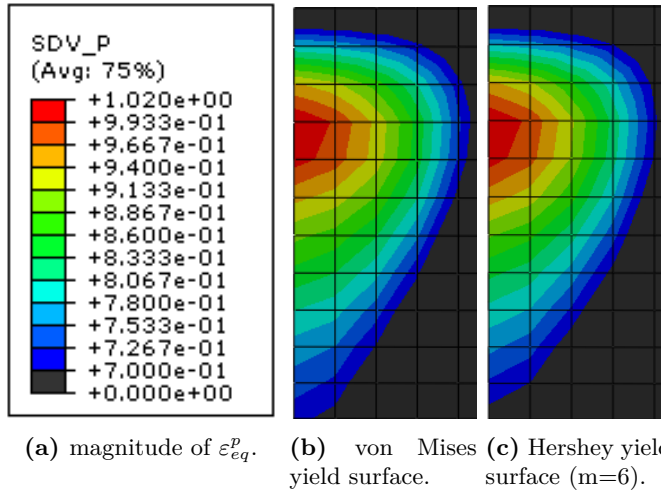


**Figure 5.41:** Contour plot of the equivalent plastic strain for different yield criteria. Plots are taken from the most deformed zone (Figure 5.20).

### 5.5.6 Global Analysis Using Fully Integrated Elements

At the end of this work it was suggested after dialog with Simulia Nordic (Nordic supplier of Abaqus) to test the C3D8I-element on this particular problem. This is a linear eight noded fully integrated element similar to the standard C3D8-element, where "I" denotes "incompatible mode". Contrary to the C3D8-element, which is a eight noded linear fully integrated displacement based element, it models shear behaviour correctly when exposed to pure bending. I.e. it is not susceptible to shear locking (Section 5.1.4). Additionally it does not lock for approximately incompressible material behaviour, volumetric locking (Section 5.1.4), according to Simulia Nordic. To obtain this, the element is supplied with additional shape functions, called "bubble functions", associated with 13 additional DOFs compared to the C3D8-element [15]. The displacement modes associated with these DOFs are usually called "incompatible" or "nonconforming" because, at locations other than at the nodes, they allow overlaps or gaps between adjacent elements [51].

To compare the difference between using reduced integration (C3D8R), standard fully integrated elements (C3D8) and fully integrated elements with incompatible

## 5. Finite Element Analysis

---

modes (C3D8I), analyses were carried on a relatively coarse global model. The model was meshed with 3 elements through the wall thickness and with a bias in the longitudinal direction:  $2.1 \times 1.4 \times 2 \text{ mm}^3$  at midspan, gradually increased to  $2.1 \times 1.4 \times 10.2 \text{ mm}^3$  at the end of the lathed area, giving in total 28500 elements. It was assumed that the difference when changing element formulation was the largest in the dented zone, because this was the zone where most bending was observed to occur. Thus, to save computational costs, only elements 50 mm from the left cross sectional end were changed (Figure 5.42). The rest of the pipe was modeled with C3D8R-elements.

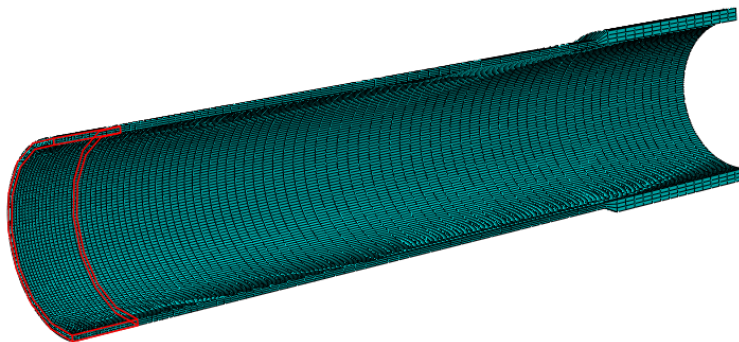


**Figure 5.42:** Elements defined to be fully integrated.

**Table 5.11:** Comparison of permanent deformation.

	Inn. Def. <sup>a</sup>	6 (N-S) <sup>b</sup>	F <sub>avg</sub>	CPU-time <sup>c</sup>
	[mm]	[mm]	[kN]	[h : min]
<b>Experiment</b>	403	27.02	40.34	
<b>C3D8R</b>	381	23.2	39.75	10:00
<b>C3D8</b>	386	23.1	41.22	19:51
<b>C3D8I</b>	385	23.3	40.41	20:27

<sup>a</sup>Inner deformation (Figure 4.6).

<sup>b</sup>Diameter at in the North-South direction at midspan (Figure 4.6).

<sup>c</sup>Total CPU usage, given in hours:minutes when carried out on 4 CPUs.

## Results

In Table 5.11 it can be seen that the global force response of the pipe, given as the average force<sup>11</sup>,  $F_{avg}$ , is well captured by all element formulations. However, the computational effort needed is greatly increased when using fully integrated elements.

A comparison of the magnitude of equivalent plastic strain in the dented zone is presented in Figure 5.43. It is observed that fully integrated elements estimate a larger magnitude compared to reduced integration. This is probably related to the fact that the models with fully integrated elements in total have six integration points across the thickness, whereas the model with reduced integration only has three (one in each element). As a comparison it was shown in Section 5.5.2 that when using six C3D8R-elements across the thickness, the maximum equivalent plastic strain was estimated to 1.070 (Quarter 6).

It was especially interesting to observe that one element was eroded (seen in Figure 5.43), exactly where and when it was expected, when using C3D8I-elements. The element was eroded in the most plastically deformed zone (beside the element with the largest magnitude of  $\varepsilon_{eq}^p$ ) during the spring back phase. To get a better look at the differences between the elements, a comparison of different relevant measures of stress and strain is presented in Figure 5.44. The integration point with the largest magnitude of equivalent plastic strain after complete loading was chosen as the reference point with regard to data extraction. It can be seen in Figure 5.43 that this is the same element. However it can be noted that it was not the same integration point.

It can be seen that the predicted magnitude of damage,  $D$  (Equation (5.7)), according to the Cockcroft-Latham criterion is a lot higher when using C3D8I. This is caused by a major difference in the major principal stress history,  $\sigma_1$ . The difference is also evident when comparing the hydrostatic stress,  $\sigma_H$ : there is no compressive phase (negative  $\sigma_H$ ) in the respective C3D8I-integration point, contrary to C3D8 and C3D8R. It is interesting to observe that in spite this, the magnitude of equivalent plastic strain is approximately the same. This is probably because the equivalent plastic strain is driven by the equivalent stress which do not take the hydrostatic stress into account, but instead is based on the deviatoric stress (Section 2.1). It is also interesting to observe that no significant differences are observed when comparing C3D8 and C3D8R. The plots illustrate the fact that in spite a similar global response and similarity in some parameters, other parameters relevant to fracture might be significantly different when changing the element formulation.

---

<sup>11</sup>The average force is calculated as the force-displacement integral divided by the indenter position when impacting the buffer.

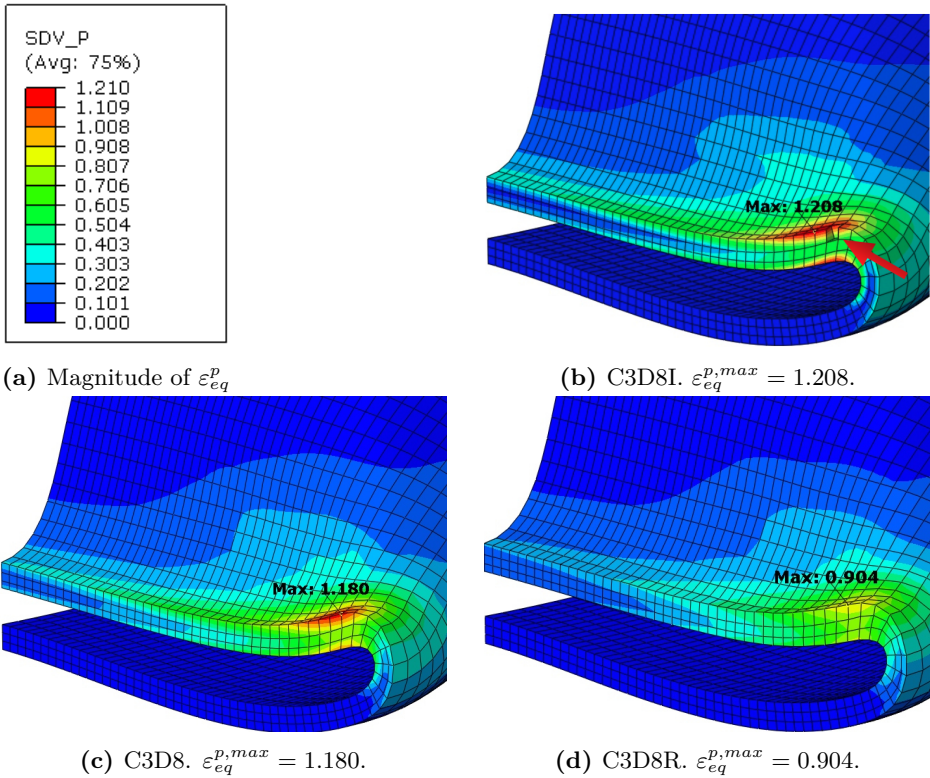


**Figure 5.43:** Distribution of equivalent plastic strain after deformation for different element formulations. The arrow indicate the eroded element. Note that the indicated Max-values at the respective nodes are extrapolated based on element integration points.

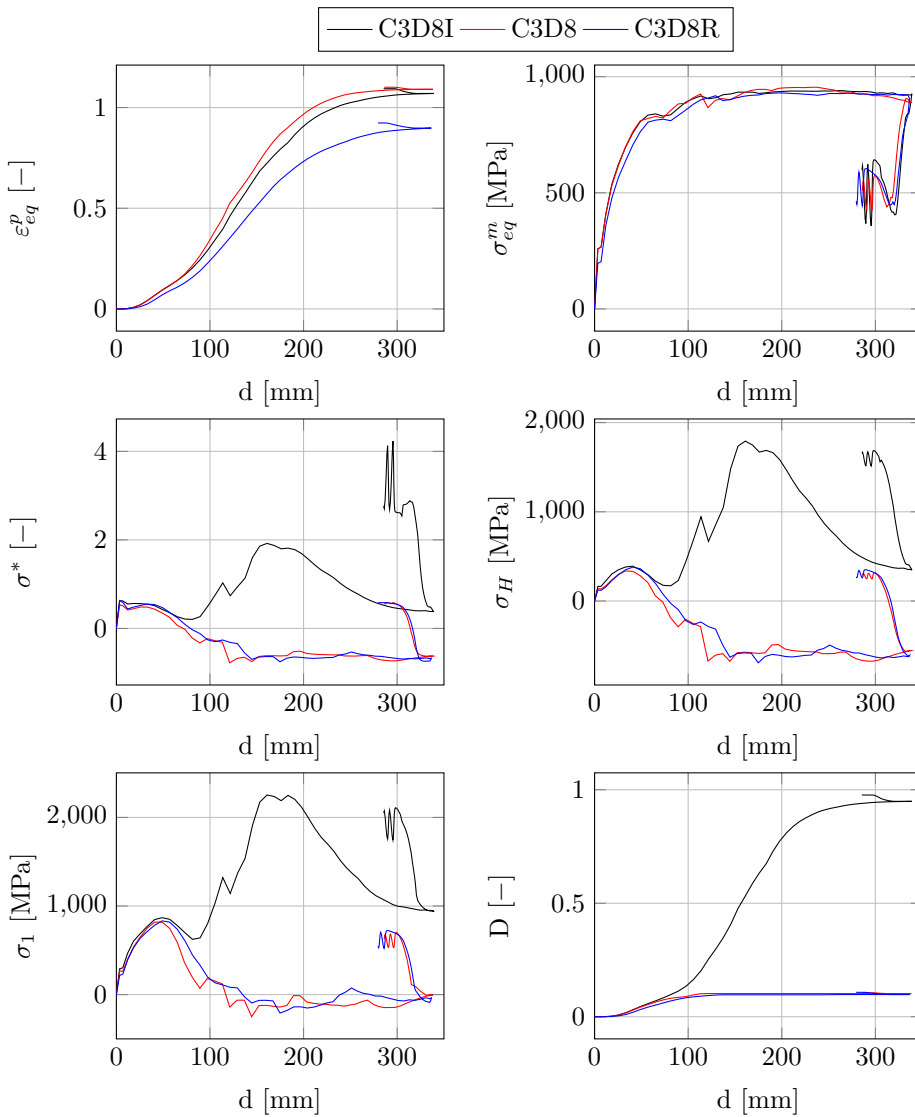


**Figure 5.44:** Comparison between different element formulations. Data are extracted from the element integration point with the highest magnitude of equivalent plastic strain after complete deformation and plotted against displacement in indenter direction of the respective element.

### Refined Analysis

In light of the eroded element observed when using C3D8I elements it was of great interest to carry out analysis on refined models. Thus two additional analyses were carried out on global models with 6 and 9 elements through the thickness. The model with 6 elements through the wall thickness was meshed with elements of size  $0.6 \times 1.4 \times 1.5 \text{ mm}^3$  at midspan, gradually increased to  $0.6 \times 1.4 \times 10 \text{ mm}^3$  at the end of the lathed area, in total 78960 elements. To save computational costs, only elements 50 mm from the symmetry plane at midspan were defined as C3D8I-elements. C3D8R-elements were used elsewhere.

As a "final" model it was decided to carry out analysis on a global model with 9 elements through the thickness, where the entire pipe was defined with C3D8I-elements. The elements of the "Quarter 9"-model (Section 5.5.2) were simply changed from C3D8R to C3D8I and the analysis was submitted on 64 CPUs, using the super computer situated at NTNU named "Vilje". The time estimated if the simulation was to be carried out on 8 CPUs was approximately 1000 hours.

### Results

Unfortunately the model with 9 elements through the thickness went wrong. For unknown reasons some elements in the transition zone (Figure 5.17) were eroded in the beginning of the simulation. However this did not influence the global response of the pipe significantly during subsequent deformation. But the buffer did not deform as it should have done (deformed a lot more) when impacted by the indenter and for some reason this aborted the whole analysis. However the global force response of the simulation looked reasonable and when comparing the average force, calculated to 41.4 kN, it is seen that it is approximately the same as the previous simulations (Table 5.11). The simulation was thus deemed trustworthy until buffer impact, at least in the sense of making comparison of trends with regard to mesh refinement. The model with 6 elements through the thickness executed correctly.

Comparison of relevant measures of stress and strain in the integration point with the highest magnitude of equivalent plastic strain after loading is presented in Figure 5.45 for 3, 6 and 9 C3D8I-elements through the thickness. Additionally, data from the global model with 9 C3D8R-elements through the thickness ("Quarter 9") is included for comparison. First of all it should be noted that based on these results it is not possible to determine convergence on any of the presented measures.

It was previously noted that using C3D8I-elements predicted a lot more accumulated damage than C3D8- and C3D8R-elements. This effect is observed to decrease when the number of elements through the wall thickness is increased from 3 to 9. From a value of almost 1.0, the damage parameter,  $D$ , is decreased to approximately 0.3. I.e. far from predicting fracture. In fact it is seen that the model with 9 C3D8I-elements through the thickness is very similar to the



one with 9 C3D8R-elements. Based on these results it seem reasonable to conclude that the high magnitude of predicted damage when using 3 C3D8I-elements through the wall thickness only was a feature of the coarse mesh used. This point illustrate the very high mesh (and element) sensitivity of local stresses and strains that develop in the pipe when impacted.

## 5. Finite Element Analysis

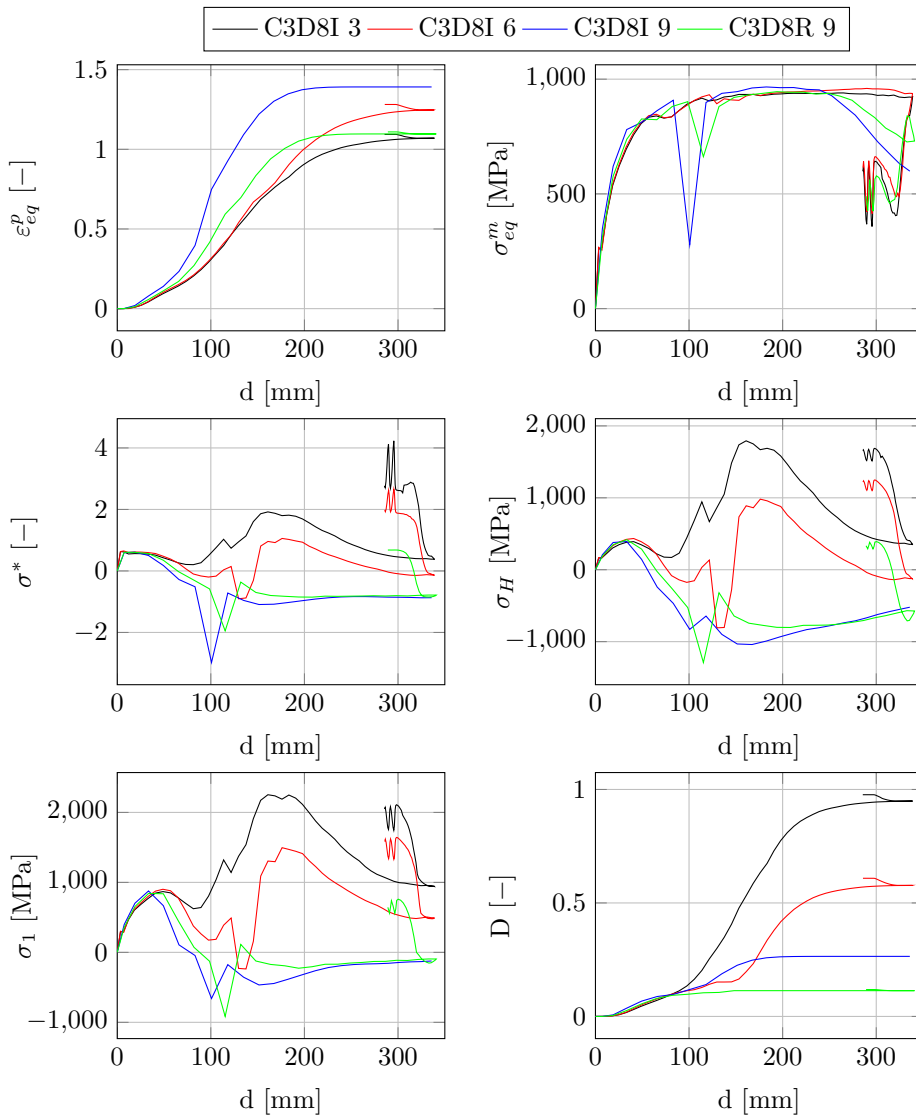


**Figure 5.45:** Comparison of mesh refinement when using C3D8I/R-elements: 3, 6 and 9 elements through the wall thickness. Data are extracted from the element integration point with the highest magnitude of equivalent plastic strain after complete deformation and plotted against displacement in indenter direction of the respective element.

### Concluding Remarks

The high magnitude of predicted accumulated damage when using C3D8I-elements on a coarse mesh is only a feature of the mesh and is not found when the mesh is refined.

Simulation of models with 6 and 9 C3D8I-elements through the thickness is not able to determine convergence on any relevant measures of stress or strain locally in the impacted zone.

#### 5.5.7 The Effect of Pressure

It was of interest to carry out a numerical experiment to investigate the effect of internal pressure when a pipe is dynamically impacted. The pipe K experiment was repeated numerically with application of 103 *bar* constant internal pressure.

The pipe was meshed in Abaqus using C3D8R-elements. 3 elements through the wall thickness with a bias in the longitudinal direction.  $2.1 \times 1.4 \times 2 \text{ mm}^3$  at midspan, gradually increased to  $2.1 \times 1.4 \times 10.2 \text{ mm}^3$  at the end of the lathed area, giving in total 28930 elements. Two simulations, with and without internal pressure, were carried out on the same mesh due to the previously noted high mesh sensitivity. It is important to note that this is only a numerical experiment, and that lab results not exists for dynamic impact with constant internal pressure. Additionally, the local strains have not converged on such a coarse mesh using C3D8R-elements (Section 5.5.2).

The internal pressure was applied in an initial smooth step of 0.002 *s*, and then maintained constant at 103 *bar*. The material was defined using SMM, with combined hardening, similar to the previously discussed pipe K models.

The analysis was run with double precision on 4 CPUs, and took approximately 8 hours to finish. A 1-2 % deviation was noted on the energy balance relative to the magnitude of internal energy at the end. The artificial strain energy was 1.7-2% relative to the internal energy and some hourglass modes were observed in the impacted zone of the pipe.

### Results

The force-displacement plot when impacted with and without internal pressure is given in Figure 5.46. It is noted that internal pressure significantly increased the stiffness of the pipe. The average force response of the pipe was noted to increase from 36.4 *kN* to 87.9 *kN*. Meaning that the kinetic energy of the indenter (5.18 *m/s*, 1472 *kg*), was absorbed after less indenter displacement: reduced from 393

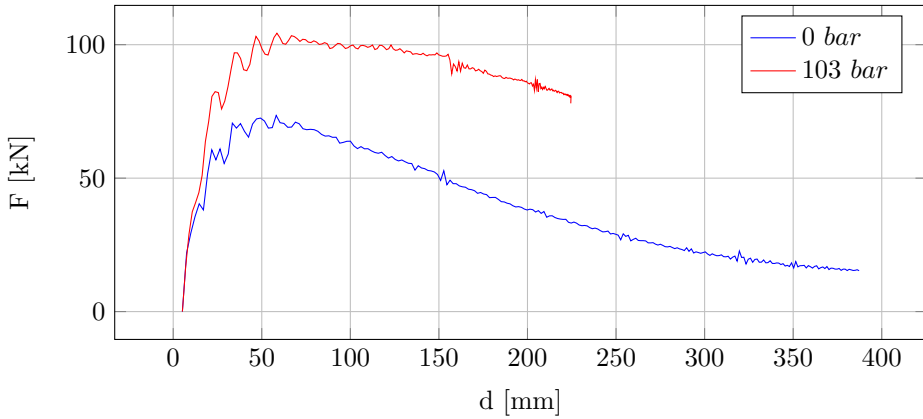


**Figure 5.46:** Pipe K experiment, with and without internal pressure.

*mm* to 224 *mm*. The increased stiffness of the pipe resulted in a less deformed final configuration (Figure 5.47). These findings coincide with what Jones and Birch [46] discovered when doing experimental dynamically testing on pressurized pipes and compared it with unpressurized.

### Deformation

It is interesting to compare the magnitude of equivalent plastic strain, in the respective critical element (the element with the highest magnitude of  $\varepsilon_{eq}^p$  after deformation). Figure 5.48 illustrates how the equivalent plastic strain increases with indenter deformation, along with the instantaneous stress triaxiality. The same trend that was discussed in Section 5.3.3 is seen in this case: the critical element undergoes a larger magnitude of plastic deformation during spring back when the pipe is pressurized compared to when it is not. The equivalent plastic strain increase from 0.58 to 0.80 during spring back when the pipe is pressurized,

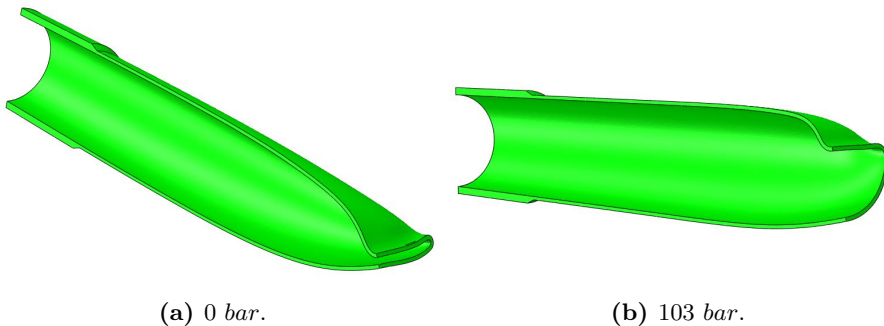


**Figure 5.47:** Deformation when impacted at 5.18 *m/s* (pipe K), without and with 103 *bar* internal pressure.

whereas it increases from 0.81 to 0.83 when the pipe is not. I.e. a similar magnitude of final plastic deformation in the critical element is observed in the two cases. However more plastic deformation occurs in the pressurized pipe with a positive stress triaxiality, indicating that the conditions for void growth and ductile failure is better. This point is highlighted when comparing the damage parameter in the respective critical elements: 0.19 in the pressurized pipe versus 0.11 in the unpressurized. Indicating that the critical element in the pressurized pipe is closer to fracture according to the Cockcroft-Latham criterion.

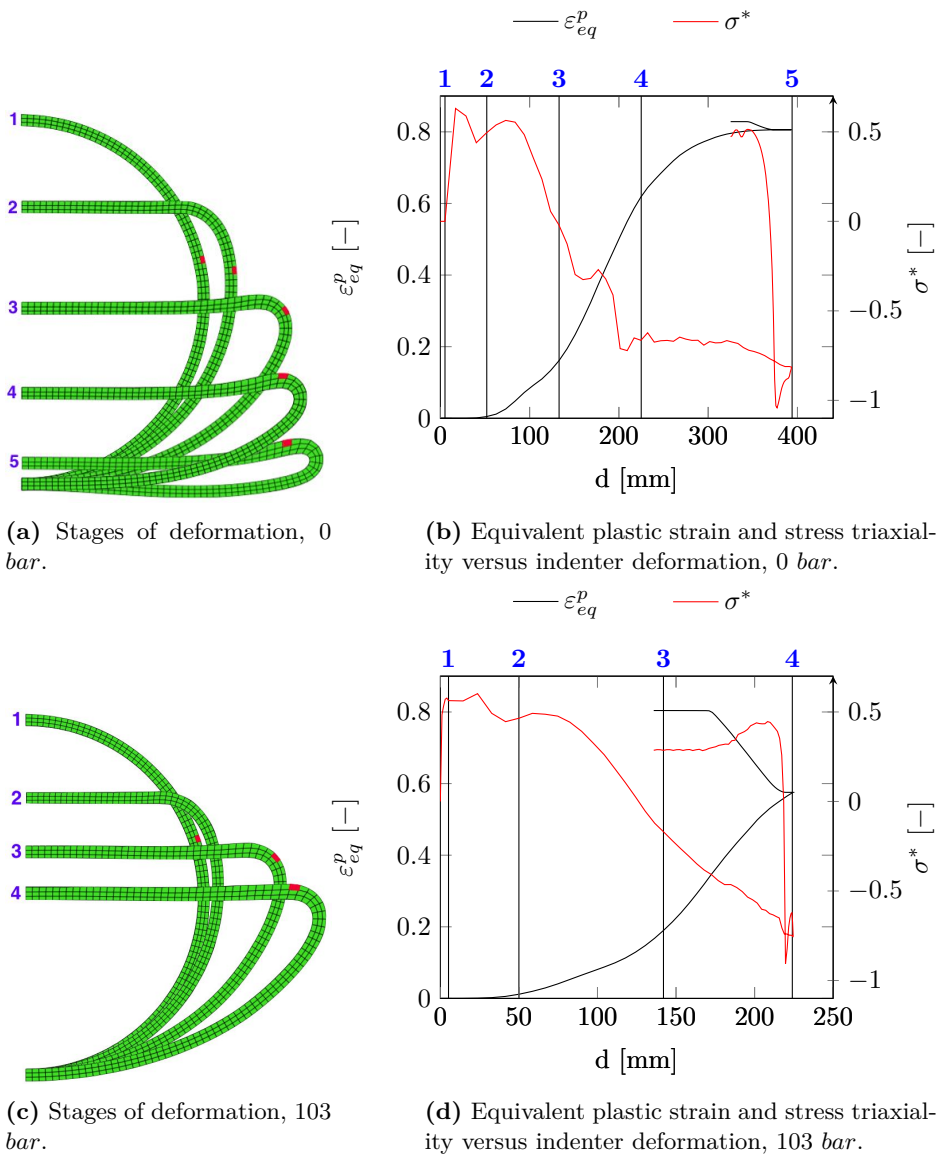


**Figure 5.48:** equivalent plastic strain,  $\varepsilon_{eq}^p$ , plotted against indenter deformation,  $d$ , along with the stress triaxiality,  $\sigma^*$ . Data are extracted from the element with the highest magnitude of equivalent plastic strain after complete deformation (element marked in red).

### 5.5.8 Summery and Discussion

Analyses of global models meshed with 3, 6 and 9 elements through the wall thickness in the dented zone was not able to determine convergence on relevant measures, such as equivalent plastic strain, locally in the most impacted zone. Simulations with both reduced integration and fully integrated incompatible mode elements were attempted without being able to do so. To carry out analysis on models consisting of more than 9 elements through the wall thickness will be very time consuming due to the rapid increase in computational cost when refining the mesh in an explicit analysis. The global force response of the pipe is observed to converge when using 3 elements through the thickness and reduced integration, but it is clear that this not should be taken as a sign that the entire solution has so.

It was attempted to use submodeling of the impacted zone. I.e. make a small model of the impacted zone and transfer displacements from a deformed global model. However due to the critical time step when using explicit time integration, the computational cost of carrying out the submodel analysis soon become large when the mesh was refined. Despite that the total number of elements in the submodel is low. It was attempted to apply both mass and time scaling successively to reduce the computational cost, but unfortunately without success.

The submodel solution was found to be bounded by the solution of the global model. I.e. the solution of a submodel will not continuously improve with mesh refinement when driven by a non-converged global model. Based on these observations, submodeling was deemed to be a dead end when applied on this particular problem.

Based on this it still remains as a question to the writers how one could carry out analysis and accurately describe the stress-strain history in the most impacted zone of the pipe. One possibility could be to carry out analysis using higher order elements (this is not yet available in Abaqus/Explicit), but this is left for further work.

One of the objectives was to investigate if it was possible to predict fracture when using the Cockcroft-Latham fracture criterion. Depending on the type of element used the predicted magnitude of damage was 0.15-0.3 (element is deleted at 1.0). I.e. the criterion is quite far from predicting fracture despite that the magnitude of equivalent plastic strain is above 1.0 (Figure 3.16 and 3.17). The reason for this is perhaps best illustrated when evaluating Figure 5.49. It is seen that a lot of plastic deformation take place with a negative major principal stress. I.e. no damage is accumulated according to the Cockcroft-Latham criterion, which probably is not a very likely assumption. The compression-tension tests discussed in Section 3.2.3 displayed a significant drop in the fracture strain in tension after pre-compression. I.e. the material does in fact take damage when plastically deformed with a negative major principal stress. In light of these considerations it would have been interesting to carry out analysis on refined models using a

## 5. Finite Element Analysis

---

fracture criterion able to predict accumulation of damage in a compressive state. However it must also be mentioned that these considerations are based on a non-converged global solution.

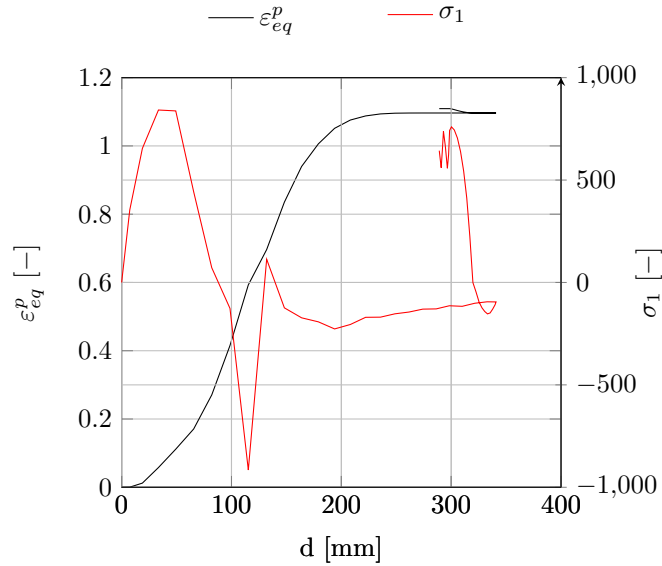


**Figure 5.49:** Equivalent plastic strain,  $\varepsilon_{eq}^p$ , plotted against element displacement in indenter direction,  $d$ , along with the major principal stress  $\sigma_1$ . Data are extracted from the element with the highest magnitude of equivalent plastic strain after complete deformation in the "Quarter 9" global model.



## Chapter 6

# Summary and Conclusions

Deformation of a pipe impacted in the transverse direction can be characterized by three phases of deformation [41]: local denting, denting and global bending and finally bending only (Figure 6.1). When considering the cross section where the pipe was impacted, local denting may also be visualized as a plastic hinge moving in the circumferential direction. Figure 6.2 illustrate how the equivalent plastic strain increase in selected elements when the pipe is deformed. A step increase is observed to occur in each element, followed by a relatively constant magnitude of equivalent plastic strain during subsequent deformation. The step increase is caused by the plastic hinge and it is seen that the magnitude of the increase also is getting larger as the hinge is moving in the circumferential direction.

As the pipe is deformed, elastic energy builds up. This energy is released when the striking object is removed, causing the pipe to spring back. As can be seen in Figure 6.2, this causes only a small increase in plastic deformation. The state of stress is also reversed during this process. Such that in the most plastically deformed element, element 1431 in Figure 6.2, the state of stress is reversed from a state of compression to a state of tension. This change of state is illustrated

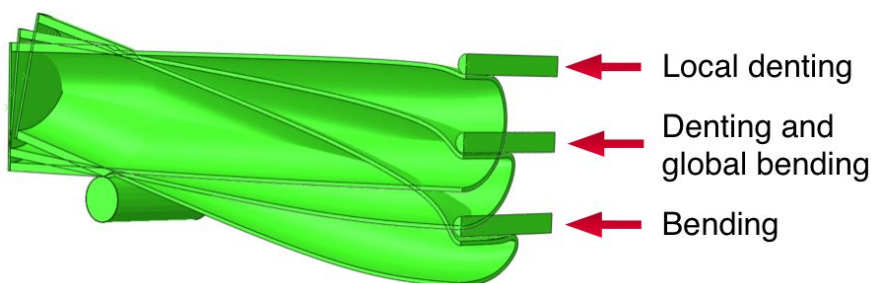


**Figure 6.1:** Phases of deformation.

## 6. Summary and Conclusions

in Figure 5.49 where the major principal stress is plotted with equivalent plastic strain against element displacement for the same element (element 1431), it is seen that the major principal stress jump from a negative to a positive value.

An anchor or trawl gear impacting a pipeline on the seabed can potentially be hooked in the pipeline and pull it out of position. Such interference will build up large amounts of elastic energy. When the anchor/trawl gear is released, the elastic energy will cause the pipeline to move back towards its initial position. I.e. the bended part during impact will be stretched back. This situation of loading has previously been experimentally recreated by first dynamically impacting a simply supported pipe in a kicking machine, and subsequently stretch the pipe straight in a quasi-static tension rig [1]. A clearly visual fracture was found on the surface of all pipes during the stretching phase and the degree of fracture depended on the magnitude of deformation after impact (depending on impact trolley velocity).

It was of interest to investigate when fracture initiates. Metallurgical investigation of impacted pipes (not stretched) revealed internal and external cracks in the pipe wall, potentially not visible on the surface of the pipe [3]. These cracks reduce the integrity of the pipe and may be very hard to detect by non-destructive inspection. As part of this thesis equivalent quasi-static experiments have been conducted to determine if these cracks are dynamically dependent or not. Neither

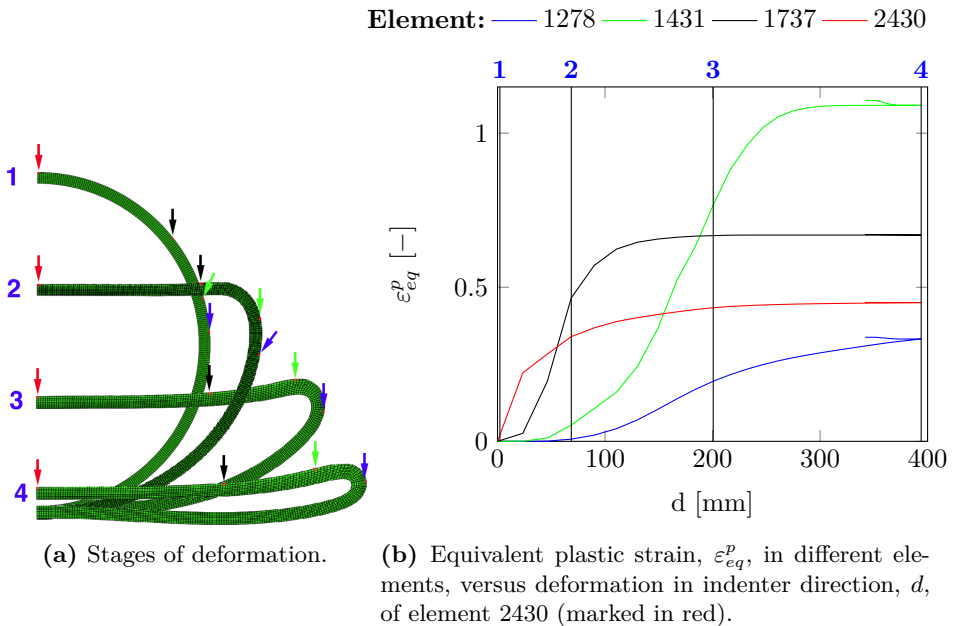


**Figure 6.2:** Plastic equivalent strain at different locations compared to different stages of deformation.

internal nor external cracks were found in the pipe wall by metallurgical investigation of pipes exposed to approximately the same amount of deformation as the dynamically impacted pipes. Based on this it is concluded that the formation of such cracks indeed are dependent on dynamic loading.

The location of these cracks seems to coincide with where the largest magnitudes of equivalent plastic strain is observed in FEA models. It was therefore of interest to investigate if it was possible to predict such fracture using the Cockcroft-Latham fracture criterion. The combination of denting, bending and spring back cause a complex stress-strain history locally in the impacted area of the pipe and it was found very difficult to describe this situation of loading accurately using a coarse mesh of linear eight noded solid elements. It was not possible to determine convergence on the magnitude of equivalent plastic strain in the impacted area when carrying out analyses on pipe models meshed with 3, 6 and 9 elements through the wall thickness in the impacted zone. Both reduced integrated elements (C3D8R) and fully integrated, incompatible mode elements (C3D8I) were attempted without being able to do so. However, it should be noted that the global force response of the pipe is well captured using only 3 elements through the wall thickness. Especially this point illustrates a very important aspect of this problem: convergence on the global force response does not imply convergence on relevant measures locally in the impacted zone.

In an attempt of obtaining convergence on equivalent plastic strain in the impacted zone it was investigated if it was possible to utilize an analysis technique known as submodeling in Abaqus. Displacements from a global analysis were transferred to specific boundaries on a small submodel in a stepwise manner, such that the submodel deformed in the same way as the respective impacted area of the global model. This way of modeling is concluded to be a dead end when applied to this particular problem for two reasons. Due to the critical time step of explicit analyses, the submodel requires a huge number of time increments to complete. Hence, the computational effort needed to complete the analysis becomes extremely high although the total number of elements in the submodel is low. If one actually was able to carry out such an analysis, the deformation of the submodel will be bounded by the displacements obtained from the most likely non-converged global model.

The predicted amount of damage according to the Cockcroft-Latham fracture criterion in the integration point with the largest magnitude of equivalent plastic strain varied between 0.15-0.3 (element erosion at 1.0) depending on the type of element used. I.e. the criterion is far from predicting fracture despite that the magnitude of equivalent plastic strain is above 1.0 and close the fracture strain observed when carrying out axisymmetric uniaxial material tests on the X65 pipe steel.

A pipeline may in reality be under the influence of internal pressure and axial forces which build up when it is dragged out of position. To investigate this

## 6. Summary and Conclusions

---

effect pipes were pressurized with approximately 100 *bar* internal pressure and bended quasi-statically in a three point stretch-bending rig, while zero, constant and linearly increasing horizontal loading (in the axial direction) were applied.

Internal pressure was seen to increase the stiffness of the pipe approximately by 30% during all phases of deformation, with respect to the average indenter force and the cases of loading discussed throughout this thesis. It was also observed that internal pressure reduces the magnitude of local denting relative the magnitude of global bending, in accordance with the findings of [46]. No significant differences with respect to local denting were found when comparing zero, constant and linearly increasing horizontal loading.

Previous equivalent experiments without internal pressure (only transverse bending and horizontal loading) concluded that horizontal loading increases the force response of the pipe, especially during the last phase characterized as bending [5]. No significant differences were seen on local denting either by comparing permanent deformation or strains obtained by DIC between bending with and without horizontal loading.

FEA were carried out to investigate if it was possible to recreate the experiments numerically. The force response was a bit underestimated ( $\approx -6.5\%$ ), but the main trend was well captured. The underestimated force response is probably related to the combined isotropic/kinematic hardening material model used. It has previously been noted [2, 3, 4, 5] that an isotropic hardening model increases the force response during bending compared to a combined hardening model. Comparison of the equivalent plastic strain and the state of stress between models with zero, constant and linearly increasing horizontal loading revealed no significant differences.

FEA of pipes loaded with and without internal pressure indicate that the maximum equivalent plastic strain after deformation and before spring back is higher in pipes loaded without internal pressure. However, more plastic straining occur during the spring back phase in the pressurized pipe and the final magnitude after complete unloading is approximately the same. Since a larger portion of plastic deformation occurs during the spring back (with a positive stress triaxiality) it is assumed that the pressurized pipe is more prone to ductile failure than the unpressurized. Numerical experiments on pipes with constant internal pressure exposed to dynamic impact indicate the same trend. I.e. testing without internal pressure might be less conservative with respect to ductile failure than testing with internal pressure. However, it must be pointed out that this indication is not supported by experimental work.

The wall thickness of the pipes used in the experiments is not constant and this has affected the force-displacement curves obtained quite a lot. In this thesis it has been experimented to make the force-displacement plot dimensionless in such a way that the wall thickness variation was accounted for. Scaling the indenter

force with a theoretical average denting force, based on the formula proposed by [45], seem to provide good results.

The research presented in this thesis has showed that fracture in X65 steel pipes is dynamically dependent and hard to predict using FEA and the Cockcroft-Latham fracture criterion. It still remain unknown exactly what magnitudes of deformation that is required to initiate fracture in the pipe wall. Since fracture is dynamically dependent it is clear that quasi static testing not is sufficient with regard to failure and that the dynamical differences between a pipe impact in the lab and at the seabed needs to be investigated. Quasi static testing with constant internal pressure showed that internal pressure changed the mode of deformation and FEA of the respective experiments indicate that internal pressure should be included in case of future experimental work.



# Further Work

Based on the results from this research the following topics is suggested for future work:

**Dynamical differences.** Quasi-static experimental testing determined fracture to be dynamically dependent. The dynamic behavior of a pipe impacted at seabed will probably be different from the behavior of a pipe impacted in the lab. How does the surrounding water, span length between the supports, contact with the seabed, pipe coating etc. influence the dynamics?

**Pressurized Pipes.** In light of the numerical work predicting internal pressure to increase the probability for fracture, it would be very interesting to carry out dynamic impact tests on pipes with constant internal pressure. This would be a rather complicated experiment, but one possibility could be to pressurize a pipe with water and connect it with a large reservoir filled with a compressible medium to account for volume changes during deformation.

**Particle Crushing.** Metallurgical investigation of the fracture that occurred after dynamic impact revealed crushed particles in the bottom of the dimples found on the fracture surface (Section 3.2). It would be interesting to carry out more detailed investigation of the material after quasi-static bending. Do the crushed particles also exist after quasi-static deformation? What amount of deformation is required to crush these particles?

**Cell Modeling.** It is assumed that the calcium aluminate particles trapped within the matrix (Section 3.2) cause stress concentrations and void nucleation. It would be interesting to carry out cell model analysis to investigate how different states of stress/strain influence void growth/locking. However the major challenge would be to relate such results to the global loading of the pipe.

**Fracture Criterion.** It seems like the Cockcroft-Latham fracture criterion is not able to predict the accumulated damage during compression in a correct manner because the major principal stress is negative when a lot of plastic deformation occurs in the critical zone. It would be interesting to investigate the behavior of other criterions which perhaps are better at doing this.





# References

- [1] Slåttedalen K, Ørmen A. Impact Against Offshore Pipelines [Master thesis]. Trondheim: Norwegian University of Science and Technology; 2010.
- [2] Fornes J, Gabrielsen S. Impact Against Offshore Pipelines [Master thesis]. Trondheim: Norwegian University of Science and Technology; 2011.
- [3] Aune V, Hovdelien M. Impact Against Offshore Pipelines [Master thesis]. Trondheim: Norwegian University of Science and Technology; 2012.
- [4] Asheim T, Mogstad I. Impact Against Offshore Pipelines [Master thesis]. Trondheim: Norwegian University of Science and Technology; 2013.
- [5] Jakobsen E. Deformation of Pressurized Pipelines [Master thesis]. Trondheim: Norwegian University of Science and Technology; 2014.
- [6] DNV. Offshore standard DNV-RP-F111: Interference between trawl gear and pipelines. Det Norske Veritas, 2010.
- [7] Kristoffersen M, Børvik T, Langseth M, Hopperstad OS, Ilstad H, Levold E, editors. Damage and failure in an X65 steel pipeline caused by trawl gear impact. Proceedings of the International Conference on Offshore Mechanics and Arctic Engineering - OMAE; 2013.
- [8] Hanssen A, Auestad T, Tryland T, and Langseth M. The kicking machine: A device for impact testing of structural components. International Journal of Crashworthiness; 2003.
- [9] Clausen AH. Stretch Bending of Aluminium Extrusions [Dr.ing thesis]. Trondheim: Norwegian University of Science and Technology; 1999.
- [10] Wikipedia. Cauchy stress tensor [Internet], Updated: 31.01.2014; Cited: 05.02.2014. [http://www.en.wikipedia.org/wiki/Cauchy\\_stress\\_tensor](http://www.en.wikipedia.org/wiki/Cauchy_stress_tensor)
- [11] Irgens F, Continuum mechanics. Berlin : Springer; (c2008).
- [12] Wikipedia. Deformation (mechanics) [Internet], Updated: 05.02.2014; Cited: 06.02.2014. [http://en.wikipedia.org/wiki/Deformation\\_\(mechanics\)](http://en.wikipedia.org/wiki/Deformation_(mechanics))
- [13] Bob McGinty. Continuum Mechanics [Internet], Cited; 12.01.2014. <http://www.continuummechanics.org>

## REFERENCES

---

- [14] Mathisen KM. Lecture Notes in TKT4197 Nonlinear Finite Element Analysis. Trondheim: Norwegian University of Science and Technology; 2013.
- [15] SIMULIA. *Abaqus Analysis User Manual*, 6.12 edition.
- [16] SIMULIA. *Abaqus Theory Manual*, 6.12 edition.
- [17] Hopperstad O. S., Børvik T. Compendium in TKT4135 Mechanics of Materials Part I and II. Trondheim: Norwegian University of Science and Technology; 2012.
- [18] Lubliner J. Plasticity theory [Compendium]. University of Berkeley; 2005.
- [19] Wikipedia. von Mises yield criterion [Internet], Updated: 13.01.2014; Cited: 06.02.2014. [http://en.wikipedia.org/wiki/Von\\_Mises\\_yield\\_criterion](http://en.wikipedia.org/wiki/Von_Mises_yield_criterion)
- [20] Wikipedia. Infinitesimal Strain Theory [Internet], Updated: 03.02.2014; Cited: 14.02.2014. [http://en.wikipedia.org/wiki/Infinitesimal\\_strain\\_theory](http://en.wikipedia.org/wiki/Infinitesimal_strain_theory)
- [21] Barsoum I, Faleskog J, Pingle S. The Influence of the Lode Parameter on Ductile Failure Strain in Steel. *Procedia Engineering*. 2011;10(0):69-75.
- [22] François D, Pineau A, Zaoui A. *Mechanical Behaviour of Materials: Volume II: Fracture Mechanics and Damage*. Dordrecht: Springer Netherlands; 2013.
- [23] Callister W. D., Rethwisch D. G., *Materials Science and Engineering*. 8. edition. Wiley and Sons; 2011.
- [24] Sedláček R, *Finite Elemente in der Werkstoffmechanik*. 1. edition. Munich: Verlag Dr. Hut; 2009.
- [25] Wikipedia. Viscoplasticity [Internet], Updated: 25.10.2013; Cited: 02.04.2014. <http://www.en.wikipedia.org/wiki/Viscoplasticity>
- [26] Anderson T L, *Fracture Mechanics Fundamentals and Applications*. 3. edition. Boca Raton: Taylor & Francis Group; 2005.
- [27] Sabih A, Nemes JA. Internal ductile failure mechanisms in steel cold heading process. *Journal of Materials Processing Technology*. 2009;209(9):4292-311.
- [28] Bao Y, Wierzbicki T. On the cut-off value of negative triaxiality for fracture. *Engineering Fracture Mechanics*. 2005;72(7):1049-69.
- [29] Bai Y, Dodd B. *Adiabatic shear localization: occurrence, theories and applications*. Oxford: Pergamon Press; 1992.
- [30] Blazynski T.Z. *The Adiabatic Shear Phenomenon In Materials at High Strain Rates*. London: Elsevier; 1987.
- [31] Antoun T. *Spall fracture*. New York: Springer; 2003.

- 
- [32] Ren Y, Wang F, Tan C, Wang S, Yu X, Jiang J, et al. Shock-induced mechanical response and spall fracture behavior of an extra-low interstitial grade Ti-6Al-4V alloy. *Materials Science and Engineering: A*. 2013;578(0):247-55.
- [33] Inspection Certificate X65-Steel Pipe. Buenos Aires: Tenaris; 17.11.2004.
- [34] Mustapha. A. The effect of microstructure on the susceptibility of pipeline steels to environment-assisted cracking [Internet]. 2010; Cited 1.6.2014. <http://theses.ncl.ac.uk/dspace/bitstream/10443/1222/1/Mustapha11.pdf>
- [35] DNV. Offshore standard DNV-OS-F101: Submarine pipeline systems. Det Norske Veritas, 2008.
- [36] Westermann I., Kristoffersen M., Børvik T. Impact On Pipelines, Metallurgical Investigation [Presentation]. Trondheim: SINTEF, SIMLab, NTNU.
- [37] Kristoffersen M, Børvik T, Westermann I, Langseth M, Hopperstad OS. Impact against X65 steel pipes – An experimental investigation. *International Journal of Solids and Structures*. 2013;50(20–21):3430-45.
- [38] Kane A, Børvik T, Berstad T, Benallal A, Hopperstad OS. Failure criteria with unilateral conditions for simulation of plate perforation. *European Journal of Mechanics - A/Solids*. 2011;30(4):468-76.
- [39] Bao Y, Wierzbicki T. A Comparative Study on Various Ductile Crack Formation Criteria. *Journal of Engineering Materials and Technology*. 2004;126(3):314-24.
- [40] Hill R. *The Mathematical Theory of Plasticity*. Oxford Classic Texts, first edition, 1950.
- [41] Thomas SG, Reid SR, and Johnson W. Large Deformations of Thin-Walled Circular Tubes under Transverse Loading-I. *International Journal of Mechanical Science*; 1976.
- [42] Watson AT, Reid SR, Johnson W, and Thomas SG. Large Deformations of Thin-Walled Circular Tubes under Transverse Loading-II. *International Journal of Mechanical Science*; 1976.
- [43] Watson AR, Reid SR, and Johnson W. Large Deformations of Thin-Walled Circular Tubes under Transverse Loading-III. *International Journal of Mechanical Science*; 1976.
- [44] MathWorks Documentation. CSAPS [Internet], R2014a; Cited: 30.05.2014. <http://www.mathworks.se/help/curvefit/csaps.html?searchHighlight=csaps>
- [45] Søreide TH. *Ultimate load analysis of marine structures*. Trondheim: Tapir; 1981.

## REFERENCES

---

- [46] Jones N, Birch RS. Low-velocity impact of pressurized pipelines. *International Journal of Impact Engineering*. 2010;37(2):207-19.
- [47] Wikipedia. Courant, Friedrichs and Lewy condition [Internet], Updated: 06.06.2014; Cited: 07.06.2014. [http://en.wikipedia.org/wiki/Courant-Friedrichs-Lewy\\_condition](http://en.wikipedia.org/wiki/Courant-Friedrichs-Lewy_condition)
- [48] Wall WA, Biehler J. Vorlesungsmanuskript "Finite-Elemente". München: Technische Universität München; 2012.
- [49] SIMLab. Theory Manual SIMLab Metal Model: Models for Metals and Alloys. Structural Impact Laboratory, Department of Structural Engineering, Norwegian University of Science and Technology, 2012.
- [50] SIMLab. User Manual SIMLab Metal Model: Models for Metals and Alloys. Structural Impact Laboratory, Department of Structural Engineering, Norwegian University of Science and Technology, 2012.
- [51] Cook RD, Malkus DS, Plesha ME, and Witt RJ. *Concepts and Applications of Finite Element Analysis*. University of Wisconsin-Madison. Fourth Edition, 2002.

# Appendices

## A.1 Pipe Measurements

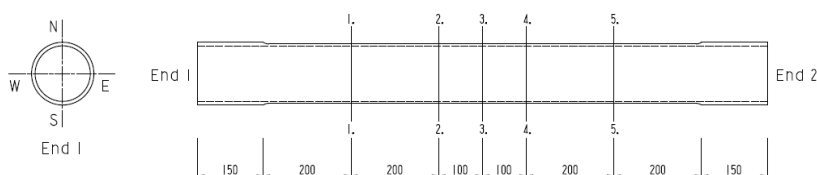


**Figure A.1:** Measurement scheme [1].

The wall thickness was measured with a PosiTector UTG (ultrasonic thickness gage). The variation of the thickness gage, mostly due to the curved surface of the pipe, was first controlled by performing 30 wall thickness measurements at the same point. However [4] compared results with measurements done with a micrometer (assumed more accurate) at the pipe ends, they found the UTG measurements to on average measure the wall 0.16 mm to thick.



**Figure A.2:** Wall thickness measurement with a ultrasonic thickness gage.

The wall thickness in the lathed area was then measured according to the scheme in figure A.1. The thickness was measured eight times at five different lengths according to the orientations; N, NE, E, SE, S, SW, W, NW.

The inner diameter of the pipes was measured at the two end sides in four directions.

**Table A.1:** Variation control of the thickness gage

Test number	Thickness [mm]
1	3.67
2	3.65
3	3.71
4	3.73
5	3.71
6	3.71
7	3.72
8	3.66
9	3.67
10	3.67
11	3.69
12	3.71
13	3.70
14	3.71
15	3.71
16	3.70
17	3.71
18	3.72
19	3.69
20	3.72
21	3.67
22	3.69
23	3.71
24	3.73
25	3.74
26	3.70
27	3.72
28	3.63
29	3.70
30	3.72
<b>AVG<sup>a</sup></b>	<b>3.70</b>
<b>SDEV<sup>b</sup></b>	<b>0.03</b>
<b>VAR<sup>c</sup></b>	<b>0.00</b>

<sup>a</sup>Average thickness<sup>b</sup>Standard deviation<sup>c</sup>Variation

**Table A.2:** Wall thickness, pipe M [*mm*].

	<b>1</b>	<b>2</b>	<b>3</b>	<b>4</b>	<b>5</b>	<b>AVG</b>	<b>SDEV</b>	<b>VAR</b>
N	3.55	3.47	3.57	3.56	3.72	3.57	0.09	0.01
NE	3.68	3.54	3.41	3.47	3.63	3.55	0.11	0.01
E	4.13	4.10	3.99	3.90	3.86	4.00	0.12	0.01
SE	4.12	3.90	3.89	3.81	3.75	3.89	0.14	0.02
S	4.31	4.30	4.20	4.07	3.82	4.14	0.20	0.04
SW	3.72	3.51	3.58	3.56	3.40	3.55	0.12	0.01
W	3.81	3.58	3.63	3.60	3.68	3.66	0.09	0.01
NW	3.64	3.43	3.55	3.45	3.62	3.54	0.10	0.01
<b>AVG</b>	3.87	3.73	3.73	3.68	3.69	<b>3.74</b>		
<b>SDEV</b>	0.28	0.33	0.27	0.22	0.14		<b>0.25</b>	
<b>VAR</b>	0.08	0.11	0.07	0.05	0.02			<b>0.06</b>

**Table A.3:** Inner diameter, pipe M [*mm*].

	<b>End 1</b>	<b>End 2</b>	<b>AVG</b>	<b>SDEV</b>	<b>VAR</b>
N-S	122.24	122.17	122.21	0.05	0.00
E-W	122.34	122.43	122.39	0.06	0.00
NE-SW	123.17	122.69	122.93	0.34	0.12
NW-SE	122.98	122.92	122.95	0.04	0.00
<b>AVG</b>	122.68	122.55	<b>122.62</b>		
<b>SDEV</b>	0.46	0.32		<b>0.38</b>	
<b>VAR</b>	0.21	0.11			<b>0.14</b>

**Table A.4:** Wall thickness, pipe N [*mm*].

	<b>1</b>	<b>2</b>	<b>3</b>	<b>4</b>	<b>5</b>	<b>AVG</b>	<b>SDEV</b>	<b>VAR</b>
N	4.13	4.10	4.26	4.54	4.54	4.31	0.21	0.05
NE	3.82	3.76	3.87	3.97	4.07	3.90	0.12	0.02
E	3.90	3.79	3.72	3.70	3.99	3.82	0.12	0.02
SE	3.54	3.54	3.45	3.48	3.58	3.52	0.05	0.00
S	3.89	3.68	3.54	3.67	3.65	3.69	0.13	0.02
SW	4.00	3.95	3.80	3.88	3.86	3.90	0.08	0.01
W	4.11	4.11	4.02	4.00	4.03	4.05	0.05	0.00
NW	3.85	3.96	4.30	3.99	4.10	4.04	0.17	0.03
<b>AVG</b>	3.91	3.86	3.87	3.90	3.98	<b>3.90</b>		
<b>SDEV</b>	0.19	0.20	0.31	0.32	0.30		<b>0.26</b>	
<b>VAR</b>	0.04	0.04	0.10	0.10	0.09			<b>0.07</b>

**Table A.5:** Inner diameter, pipe N [*mm*].

	<b>End 1</b>	<b>End 2</b>	<b>AVG</b>	<b>SDEV</b>	<b>VAR</b>
N-S	122.28	122.40	122.34	0.08	0.01
E-W	122.38	122.29	122.34	0.06	0.00
NE-SW	122.25	122.10	122.18	0.11	0.01
NW-SE	122.72	122.19	122.46	0.37	0.14
<b>AVG</b>	122.41	122.25	<b>122.33</b>		
<b>SDEV</b>	0.22	0.13		<b>0.19</b>	
<b>VAR</b>	0.05	0.02			<b>0.03</b>



**Table A.6:** Wall thickness, pipe 8 [*mm*].

	<b>1</b>	<b>2</b>	<b>3</b>	<b>4</b>	<b>5</b>	<b>AVG</b>	<b>SDEV</b>	<b>VAR</b>
N	3.87	4.06	4.10	4.02	4.00	4.01	0.09	0.01
NE	3.78	3.86	3.93	4.03	4.04	3.93	0.11	0.01
E	4.29	4.25	4.48	4.51	4.41	4.41	0.13	0.02
SE	4.31	4.17	4.22	4.31	4.35	4.27	0.07	0.01
S	4.54	4.31	4.18	4.24	4.37	4.33	0.14	0.02
SW	4.13	4.08	3.85	3.81	4.03	3.98	0.14	0.02
W	4.19	4.09	3.89	3.76	3.88	3.96	0.17	0.03
NW	3.68	3.85	3.81	3.70	3.72	3.75	0.07	0.01
<b>AVG</b>	4.10	4.08	4.06	4.05	4.11	<b>4.08</b>		
<b>SDEV</b>	0.30	0.17	0.23	0.29	0.27		<b>0.24</b>	
<b>VAR</b>	0.09	0.03	0.05	0.08	0.07			<b>0.06</b>

**Table A.7:** Inner diameter, pipe 8 [*mm*].

	<b>End 1</b>	<b>End 2</b>	<b>AVG</b>	<b>SDEV</b>	<b>VAR</b>
N-S	122.62	122.53	122.58	0.06	0.00
E-W	122.42	122.51	122.47	0.06	0.00
NE-SW	123.12	122.83	122.98	0.21	0.04
NW-SE	122.93	122.82	122.88	0.08	0.01
<b>AVG</b>	122.77	122.67	<b>122.72</b>		
<b>SDEV</b>	0.31	0.18		<b>0.24</b>	
<b>VAR</b>	0.10	0.03			<b>0.06</b>

## REFERENCES

---

**Table A.8:** Wall thickness, pipe 9 [*mm*].

	<b>1</b>	<b>2</b>	<b>3</b>	<b>4</b>	<b>5</b>	<b>AVG</b>	<b>SDEV</b>	<b>VAR</b>
N	3.81	3.83	3.96	4.02	3.99	3.92	0.10	0.01
NE	4.08	4.13	4.22	4.19	4.10	4.14	0.06	0.00
E	4.25	4.22	4.38	4.20	4.04	4.22	0.12	0.01
SE	4.05	3.94	3.93	3.93	4.01	3.97	0.05	0.00
S	4.03	3.73	3.80	3.71	3.90	3.83	0.13	0.02
SW	4.01	3.91	3.95	3.98	4.14	4.00	0.09	0.01
W	3.52	3.45	3.56	3.63	3.85	3.60	0.15	0.02
NW	3.75	3.77	3.87	4.00	4.02	3.88	0.13	0.02
<b>AVG</b>	3.94	3.87	3.96	3.96	4.01	<b>3.95</b>		
<b>SDEV</b>	0.23	0.24	0.25	0.20	0.10		<b>0.21</b>	
<b>VAR</b>	0.05	0.06	0.06	0.04	0.01			<b>0.04</b>

**Table A.9:** Inner diameter, pipe 9 [*mm*].

	<b>End 1</b>	<b>End 2</b>	<b>AVG</b>	<b>SDEV</b>	<b>VAR</b>
N-S	122.72	122.40	122.56	0.23	0.05
E-W	122.48	122.60	122.54	0.08	0.01
NE-SW	122.29	122.15	122.22	0.10	0.01
NW-SE	122.73	122.44	122.59	0.21	0.04
<b>AVG</b>	122.56	122.40	<b>122.48</b>		
<b>SDEV</b>	0.21	0.19		<b>0.20</b>	
<b>VAR</b>	0.04	0.03			<b>0.04</b>

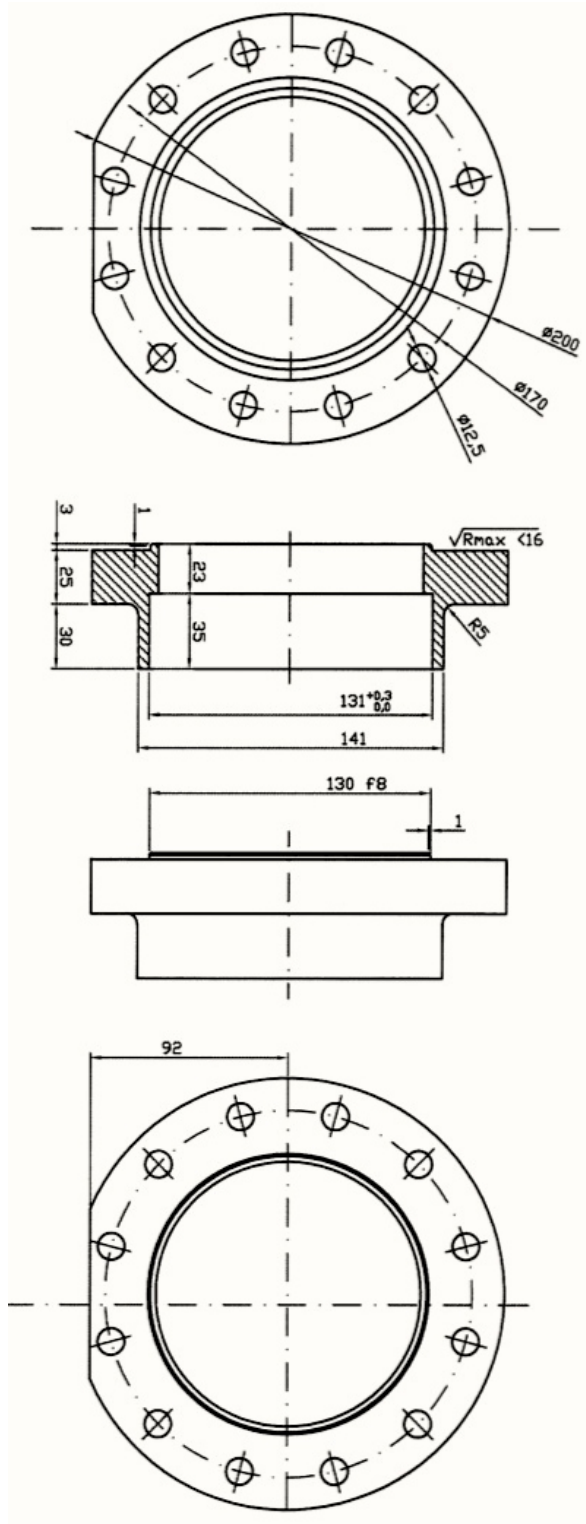
**Table A.10:** Wall thickness, pipe 10 [*mm*].

	<b>1</b>	<b>2</b>	<b>3</b>	<b>4</b>	<b>5</b>	<b>AVG</b>	<b>SDEV</b>	<b>VAR</b>
N	4.17	4.04	4.07	4.08	3.99	4.07	0.07	0.00
NE	4.43	4.49	4.50	4.53	4.41	4.47	0.05	0.00
E	4.14	4.12	4.11	4.15	4.18	4.14	0.03	0.00
SE	4.32	4.28	4.40	4.29	4.14	4.29	0.09	0.01
S	3.96	3.97	3.99	3.92	4.00	3.97	0.03	0.00
SW	3.87	3.93	3.98	4.03	4.21	4.00	0.13	0.02
W	3.92	4.00	4.10	4.08	4.28	4.08	0.13	0.02
NW	4.06	3.96	3.99	4.09	4.07	4.03	0.06	0.00
<b>AVG</b>	4.11	4.10	4.14	4.15	4.16	<b>4.13</b>		
<b>SDEV</b>	0.20	0.19	0.20	0.19	0.14		<b>0.18</b>	
<b>VAR</b>	0.04	0.04	0.04	0.03	0.02			<b>0.03</b>

**Table A.11:** Inner diameter, pipe 10 [*mm*].

	<b>End 1</b>	<b>End 2</b>	<b>AVG</b>	<b>SDEV</b>	<b>VAR</b>
N-S	122.29	122.41	122.35	0.08	0.01
E-W	122.91	122.54	122.73	0.26	0.07
NE-SW	122.03	122.07	122.05	0.03	0.00
NW-SE	122.38	122.34	122.32	0.04	0.00
<b>AVG</b>	122.38	122.34	<b>122.36</b>		
<b>SDEV</b>	0.37	0.20		<b>0.28</b>	
<b>VAR</b>	0.14	0.04			<b>0.08</b>

## A.2 Pipe Flange



### A.3 SMM Material card

Input parameters for the viscoplastic combined isotropic/kinematic hardening material model used in the numerical work when implemented using SMM.

```

** MATERIALS
**
**Material, name=SMM
**Density
7850.,
**INCLUDE,INPUT=../DEPVAR_SMM.inc
**USER MATERIAL,CONSTANTS=32
**      EFLAG,      YFLAG,      RMAPFLAG,      HFLAG
          1,          3,          2,          12
**      VFLAG,      TFLAG,      DFLAG,      SFLAG
          1,          0,          1,          0
**      STFLAG,      E,      PR,      SIGMA0
          0, 2.08000e+11, 3.00000e-01, 2.99000e+08
**      a,      THETAR1,      QR1,      THETAR2
          6, 4.00000e+09, 1.60000e+08, 1.00000e+08
**      QR2,      THETAR3,      QR3,      THETAX1
4.00000e+08, 0.00000e+00, 0.00000e+00, 5.04010e+10
**      QX1,      THETAX2,      QX2,      CSIGMA
1.29000e+08, 1.27900e+09, 1.00000e+08, 1.05e-02
**      PSIGMA,      DINIT,      DCRIT,      BETADAM
          8.06e-04,          1,          1,
          0
**      S0,      Phi,      so
1.59500e+09, 1.00000e+00, 1.00000e+00
**** Material parameters detail
** E      -> Young modulus
** PR     -> Poisson's ratio
** SIGMA0 -> Yield stress
** THETARi -> Voce's hardening modulus
** QRi    -> Voce's saturation stress
** THETAXi -> kinematic hardening modulus
** QXi    -> kinematic saturation stress
** Dinit  -> initial damage
** Dcrit  -> critical damage
** BETADAM -> damage coupling flag 0 no coupling
** S0     -> critical plastic work
** Phi    -> ECL parameter = 1 for Cockcroft-Latham
** so     -> ECL parameter = 1 for Cockcroft-Latham

```